Bifurcations, Multi-stability, and Localization in Thin Structures

Tian Yu

Dissertation submitted to the Faculty of the
Virginia Polytechnic Institute and State University
in partial fulfillment of the requirements for the degree of

Doctor of Philosophy
in
Engineering Mechanics

James Hanna, Chair
Mark A. Stremler, Co-chair
Raffaella De Vita
David A. Dillard
Chester J. Van Tyne

December 13, 2019
Blacksburg, Virginia

Keywords: thin structures, multi-stability, localization, pure bending, creases

Bifurcations, Multi-stability, and Localization in Thin Structures

Tian Yu

ABSTRACT

Thin structures exist as one dimensional slender objects (hairs, tendrils, telephone cords, etc.) and two dimensional thin sheets (tree leaves, Möbius bands, eggshells, etc.). Geometric and material nonlinearities can conspire together to create complex phenomena in thin structures. This dissertation studies snap-through, multi-stability, and localization in thin rods and sheets through a combination of experiments and numerics.

The first work experimentally explores the multi-stability and bifurcations of buckled elastic strips subject to clamping and lateral end translations, and compares these results with numerical continuation of a perfectly anisotropic Kirchhoff rod model. It is shown that this naive Kirchhoff rod model works surprisingly well as an organizing framework for thin bands with various widths.

Thin sheets prefer to bend rather than to stretch because of the high cost of stretching energy. Knowing the bending response of thin sheets can aid in simulating deformations such as creasing. The second work introduces an exact pure bending linkage mechanism for potential use in a bend tester that measures the moment-curvature relationship of soft sheets and filaments.

Mechanical rotary pleating is a bending-deformation-dominant process that deforms nonwoven materials into zigzag filter structures. The third work studies what combinations of processing and material parameters lead to successful rotary pleating. The rotary pleating process is formulated as a multi-point variable-arc-length boundary value problem for an inextensible rod, with a moment-curvature constitutive law, such as might be measured by a bend tester, as input. Through parametric studies, this work generates pleatability surfaces that may help avoid pleating failure in the real pleating process.

Creased thin sheets are generally bistable. The final work of this dissertation studies bistability of creased thin disks under the removal of singularities. A hole is cut in the disk and, through numerical continuation of an inextensible strip model, this work studies how the crease stiffness, crease angle, and hole geometry affect the bistability.

Bifurcations, Multi-stability, and Localization in Thin Structures

Tian Yu

GENERAL AUDIENCE ABSTRACT

Thin structures are those that have at least one dimension smaller than the other dimensions, such as hairs, telephone cords, and tree leaves, to name just a few. They can generate rich mechanical behaviors (e.g., snapping, crumpling) and complex shapes. A simple example is to rotate the two ends of a thin strip that has been deformed into an arch. Snapping will happen at a certain rotation angle. The first work studies snapping behaviors of thin bands subject to rotations and displacements at the two ends. This work employs a mechanical model based on force and moment balance on a spatial curve to solve the shapes of thin strips and capture the rich snapping behaviors.

It is much harder to stretch a thin sheet than to bend it, which can be easily seen by deforming a piece of paper. The physics behind this is that stretching requires more energy than bending in thin objects. Knowing the bending response of thin sheets can aid in simulating deformations of thin structures. The second work introduces a new pure bending mechanism that can subject a sheet to pure bending and measure its bending response through a moment-curvature relationship.

Thin sheets find broad applications in engineering. Mechanical pleating is a long-standing technique that deforms thin sheets into zigzag filter structures, but the mechanics behind it is unclear. The third work studies a rotary pleating process and aims to answer a basic question: What combinations of processing and material parameters lead to successful pleating? This work employs a one-dimensional model of an inextensible rod, with a moment-curvature constitutive law as input. The moment-curvature relationship of pleating materials can be measured by the pure bending mechanism developed in the second work.

Thin sheets with prescribed crease patterns can create complicated and targeted shapes, such as origami (paper folding) and kirigami (paper cutting). A simple creased thin sheet is bistable: A stable configuration can be obtained by inverting the crease, which leads to a conical vertex/singularity. The fourth work of this dissertation finds that the bistability of creased thin sheets will be destroyed if a large hole is made around the vertex. This work studies the loss of bistability of creases under removal of singularities by quantifying how the hole size, hole geometry, and other factors such as the crease angle and crease stiffness affect the bistability.

This work was supported by The NonWovens Institute (project 16-197) and the National Science Foundation under grant CMMI-1902444

Contents

List of Figures

Chapter 1

Introduction

Thin structures are those that have at least one dimension much smaller than the other dimensions, such as rods, strips, thin sheets and membranes. Because of many advantages like high flexibility, achieving large cyclic motions without failure, and low consumption of materials, thin structures find numerous applications within structural engineering. Examples include deployable space structures (e.g., solar sails, sun shields, parachutes), architectural structures (e.g., shell domes, cable-membrane structures), flexible electronics and medical devices. A telephone cord that has a helical shape is another elegant example.

Geometry, elasticity, and external loads can conspire together to generate complex behaviors in thin structures, such as snapping, crumpling, and wrinkling. Snap-through is an abrupt process triggered by the sudden release of elastic energy, such as the undesired inversion of an umbrella by a gust of wind or the flip of a clamped arch by poking its center. Snap-through is usually caused by certain bifurcations, such as fold and subcritical pitchfork bifurcations. Bifurcations in elastic structures can also be smooth, such as a supercritical pitchfork bifurcation. One of the earliest known examples is *Euler buckling*, when a thin beam is axially loaded until lateral deflection occurs.

Snap-through and buckling notoriously cause damage to engineering structures (e.g., local buckling in airplane wings and cylindrical shell tanks) and are traditionally undesirable. Recently, snapping and buckling has been revisited and utilized to design functional structures, such as robotic grippers [1], adaptive structures for flow regulation [2], and dielectric elastomeric plates for microfluidic pumps [3]. They are also embraced by mother nature to achieve functional movements, such as the rapid closure of the Venus flytrap's leaves [4] and the fast underwater suction of carnivorous *Utricularia* [5]. In this dissertation, I study various snap-through and buckling processes and obtain phase diagrams, which may help avoid jump phenomena of structures with similar geometries and guide new ideas in functional design.

Recent years have seen a surge in studying origami and kirigami structures. Origami has

been extended from laboratory paper folding to real structures with thickness [6, 7], and from rigid origami to curved folding [8, 9, 10, 11]. In curved folding, the mechanics of creases and flexibility of facets may compete to influence the mechanical responses of creased thin sheets [9, 12, 13]. This is different from traditional origami that mainly requires kinematic analyses. The mechanics of creases has been studied extensively [14, 15, 16, 17, 18], and accurately understanding the mechanics of folds is key to predict the shape and dynamics of creased structures. By introducing flexibility of the facets, recent works showed that new stable configurations can be achieved in traditional square twist [19] and simple Miura-ori patterns [20]. Lechenault and Adda-Bedia found that creased conical surfaces exhibit generic bistability, and a stable equilibrium can be achieved by inverting a creased thin disk, forming a conical vertex/elastic singularity [21]. Later, Walker and Seffen showed that once a small hole is made around the vertex of a bistable creased metal strip, the force needed to invert the strip is reduced compared to one without a hole [22]. Elastic singularities in thin sheets are generally caused by highly localized deformations, which can make isolated singular points and singular ridges [23, 24, 25]. By truncating the two ends of a stretching ridge that is formed by fastening a membrane to itself to make a bag shape, Witten found that the ridge transformed from a conical surface to a cylindrical surface [26]. Here I found that the generic bistability of creased thin sheets [21] will be lost if the hole around the vertex is large enough. I study this phenomenon in Chapter 5.

The mechanics of thin structures has been extensively studied [27], and various theories and models have been developed, such as the Kirchhoff rod theory [28], inextensible plate theory [29], and inextensible strip models [30, 31]. An effective tool to study mechanical behavior of a one dimensional slender structure is the Kirchhoff rod theory, which is based on the force and moment balance on a spatial curve. Kirchhoff rod theory adequately captures the large deformations, bifurcations and multi-stability of thin rods up to a certain anisotropy of the cross-section [32, 33, 34]. However, for a highly anisotropic rod (i.e., a strip), it fails to capture bending of the cross section, and we need a two dimensional thin plate model. Thin plates prefer to bend rather than stretch because of the high cost of stretching energy. Ideally, stretching of the middle surface of a thin plate can be set to zero, which leads to isometric deformations. Inextensible plate theory can be traced back to Mansfield and Ashwell. They developed and used it to study thin plates up to small deflections [35, 36]. Under isometric deformations, the deformed configuration of a thin plate can be parametrized by a family of straight generators. Wunderlich extended Sadowsky's work on an inextensible strip with an infinitesimal narrow width [37] to a finite-width strip and showed that the two dimensional energy functional of an inextensible strip can be explicitly integrated along generators, leading to a one dimensional variational problem [30]. Based on Wunderlich's functional, Starostin and van der Heijden derived the Euler-Lagrange equations and constructed realistic shapes of developable Möbius strips [31, 38]. They further used this framework to study multi-stability of helical ribbons [39] and triangular buckling patterns of twisted inextensible strips [40]. In this dissertation, I use a combination of various models of thin structures to study thin rods, strips and sheets.

In Chapter 2, I study bifurcations of buckled, clamped anisotropic rods and thin bands under lateral end translations. We use a perfectly anisotropic Kirchhoff rod model to capture the rich bifurcation behaviors. The naive Kirchhoff rod model captures all the bifurcation behaviors of a narrow strip and also works surprisingly well as an organizing framework for wide bands. We attempt to use the inextensible strip model to study wide bands. However, the strip model fails to capture the bifurcation behaviors of wide bands because of some singular issues.

In Chapter 3, I design an exact pure bending mechanism that is able to measure the moment-curvature relationship of soft sheets. Bending deformation is usually dominant in thin structures. Knowing the bending response of thin structures, for example, the moment-curvature relationship, is key to predict their mechanical behaviors. Pure bending can be achieved by fixing one end of the sample while letting the other end trace a cochleoidal curve and be oriented in specific directions. I design an exact single-degree-of-freedom linkage mechanism that can subject a sheet to pure bending.

In Chapter 4, I study the mechanics of the rotary pleating process to understand what combinations of processing and material parameters lead to successful pleating. Thin sheets and membranes can be pleated or folded for different purposes, such as reducing the volume in the stowed configuration [41, 42] and increasing contact areas of filter structures. Pleated structures are widely found in nature, for example, insect wings [43, 44] and plant leaves [45]. Mechanical pleating is a long-standing technique that deforms thin sheets into accordion-like filter structures. However, mechanical models of the pleating process appear to be absent in the literature, and the mechanics of pleating is not well understood. We adopt a one-dimensional approach and, based on an inextensible rod theory, we formulate mechanical pleating as a multi-point variable-arc-length boundary value problem. In our mechanical pleating model, material properties enter the system through a moment-curvature relationship, such as would be measured by a pure bend tester.

In Chapter 5, I study bistability of creased thin disks under removal of elastic singularities. We experimentally explore the bistable behavior of creased thin disks by varying the hole geometry and material thickness. Numerical continuation of an inextensible strip model [31, 38] enables us to systematically quantify the dependence of the bistability on the hole geometry, rest crease angle, crease stiffness, number of creases, and so on.

Bibliography

[1] E. Siéfert, E. Reyssat, J. Bico, and B. Roman. Programming curvilinear paths of flat inflatables. *Proceedings of the National Academy of Sciences*, 116(34):16692–16696, 2019.

[2] G. Arena, R. M. J. Groh, A. Brinkmeyer, R. Theunissen, P. M. Weaver, and A. Pirrera. Adaptive compliant structures for flow regulation. *Proceedings of the Royal Society A: Mathematical, Physical and Engineering Sciences*, 473(2204):20170334, 2017.

[3] B. Tavakol, M. Bozlar, C. Punckt, G. Froehlicher, H. A. Stone, I. A. Aksay, and D. P. Holmes. Buckling of dielectric elastomeric plates for soft, electrically active microfluidic pumps. *Soft matter*, 10(27):4789–4794, 2014.

[4] Y. Forterre, J. M. Skotheim, J. Dumais, and L. Mahadevan. How the venus flytrap snaps. *Nature*, 433(7024):421, 2005.

[5] O. Vincent, C. Weißkopf, S. Poppinga, T. Masselter, T. Speck, M. Joyeux, C. Quilliet, and P. Marmottant. Ultra-fast underwater suction traps. *Proceedings of the Royal Society B: Biological Sciences*, 278(1720):2909–2914, 2011.

[6] M. R. Morgan, R. J. Lang, S. P. Magleby, and L. L. Howell. Towards developing product applications of thick origami using the offset panel technique. *Mechanical Sciences*, 7: 69–77, 2016.

[7] Y. Chen, R. Peng, and Z. You. Origami of thick panels. *Science*, 349(6246):396–400, 2015.

[8] J. P. Duncan and J. L. Duncan. Folded developables. *Proc. R. Soci. Lond. A*, 383 (1784):191–205, 1982.

[9] M. A. Dias and B. Audoly. A non-linear rod model for folded elastic strips. *Journal of the Mechanics and Physics of Solids*, 62:57–80, 2014.

[10] D. Garrett, Z. You, and J. M. Gattas. Curved crease tube structures as an energy absorbing crash box. In *ASME 2016 International Design Engineering Technical Conferences and Computers and Information in Engineering Conference, Charlotte, North Carolina*, page V05BT07A017. American Society of Mechanical Engineers, 2016.

[11] D. Fuchs and S. Tabachnikov. More on paper folding. *The American Mathematical Monthly*, 106(1):27–35, 1999.

[12] E. T. Filipov, K. Liu, T. Tachi, M. Schenk, and G. H. Paulino. Bar and hinge models for scalable analysis of origami. *International Journal of Solids and Structures*, 124: 26–45, 2017.

[13] A. Gillman, K. Fuchi, and P. R. Buskohl. Truss-based nonlinear mechanical analysis for origami structures exhibiting bifurcation and limit point instabilities. *International Journal of Solids and Structures*, 147:80–93, 2018.

[14] B.Y. Dharmadasa, H.M.Y.C. Mallikarachchi, and F. López Jiménez. Characterizing the mechanics of fold-lines in thin kapton membranes. In *AIAA Spacecraft Structures Conference, AIAA SciTech Forum, Kissimmee, Florida,*, page 0450, 2018.

[15] T. Jules, F. Lechenault, and M. Adda-Bedia. Local mechanical description of an elastic fold. *Soft Matter*, 15(7):1619–1626, 2019.

[16] B. Thiria and M. Adda-Bedia. Relaxation mechanisms in the unfolding of thin sheets. *Physical Review Letters*, 107(2):025506, 2011.

[17] F. Lechenault, B. Thiria, and M. Adda-Bedia. Mechanical response of a creased sheet. *Physical Review Letters*, 112(24):244301, 2014.

[18] A. Papa and S. Pellegrino. Systematically creased thin-film membrane structures. *Journal of Spacecraft and Rockets*, 45(1):10–18, 2008.

[19] J. L. Silverberg, J.H. Na, A. A. Evans, B. Liu, T. C. Hull, C. D. Santangelo, R. J. Lang, R. C. Hayward, and I. Cohen. Origami structures with a critical transition to bistability arising from hidden degrees of freedom. *Nature Materials*, 14(4):389–393, 2015.

[20] J. L. Silverberg, A. A. Evans, L. McLeod, R. C. Hayward, T. Hull, C. D. Santangelo, and I. Cohen. Using origami design principles to fold reprogrammable mechanical metamaterials. *Science*, 345(6197):647–650, 2014.

[21] F. Lechenault and M. Adda-Bedia. Generic bistability in creased conical surfaces. *Physical Review Letters*, 115(23):235501, 2015.

[22] M. G. Walker and K. A. Seffen. On the shape of bistable creased strips. *Thin-Walled Structures*, 124:538–545, 2018.

[23] A. Boudaoud, P. Patrício, Y. Couder, and M. B. Amar. Dynamics of singularities in a constrained elastic plate. *Nature*, 407(6805):718, 2000.

[24] E. Cerda and L. Mahadevan. Conical surfaces and crescent singularities in crumpled sheets. *Physical Review Letters*, 80(11):2358, 1998.

[25] K. Matan, R. B. Williams, T. A. Witten, and S. R. Nagel. Crumpling a thin sheet. *Physical Review Letters*, 88(7):076101, 2002.

[26] T. A. Witten. Spontaneous free-boundary structure in crumpled membranes. *The Journal of Physical Chemistry B*, 113(12):3738–3742, 2009.

[27] B. Audoly and Y. Pomeau. *Elasticity and geometry: from hair curls to the nonlinear response of shells*. Oxford University Press, Oxford, 2010.

[28] S. S. Antman. Kirchhoff's problem for nonlinearly elastic rods. *Quarterly of applied mathematics*, 32(3):221–240, 1974.

[29] E. H. Mansfield. The inextensional theory for thin flat plates. *Quart. Journ. of Mech. and Applied Math.*, 8(3):338–352, 1955.

[30] R. E. Todres. Translation of W. Wunderlich's "On a developable Möbius band". *Journal of Elasticity*, 119(1-2):23–34, 2015.

[31] E. L. Starostin and G. H. M. van der Heijden. The shape of a Möbius strip. *Nature Materials*, 6(8):563–567, 2007.

[32] G. H. M. van der Heijden and J. M. T. Thompson. Lock-on to tape-like behaviour in the torsional buckling of anisotropic rods. *Physica D*, 112(1-2):201–224, 1998.

[33] E. L. Starostin and G. H. M van der Heijden. Cascade unlooping of a low-pitch helical spring under tension. *Journal of the Mechanics and Physics of Solids*, 57(6):959–969, 2009.

[34] T. Yu and J. A. Hanna. Bifurcations of buckled, clamped anisotropic rods and thin bands under lateral end translations. *Journal of the Mechanics and Physics of Solids*, 122:657–685, 2019.

[35] D. G. Ashwell. The equilibrium equations of the inextensional theory for thin flat plates. *Quart. Journ. of Mech. and Applied Math.*, 10(2):169–182, 1957.

[36] E. H. Mansfield. Bending, buckling and curling of a heated thin plate. *Proc. R. Soc. Lond. A*, 268(1334):316–327, 1962.

[37] D. F. Hinz and E. Fried. Translation and interpretation of Michael Sadowsky's paper "Theory of elastically bendable inextensible bands with applications to the Möbius band". *Journal of Elasticity*, 119(1-2):7–17, 2015.

[38] E. L. Starostin and G. H. M. van der Heijden. Equilibrium shapes with stress localisation for inextensible elastic Möbius and other strips. *Journal of Elasticity*, 119(1-2):67–112, 2015.

[39] E. L. Starostin and G. H. M. van der Heijden. Tension-induced multistability in inextensible helical ribbons. *Physical Review Letters*, 101(8):084301, 2008.

[40] A. P. Korte, E. L. Starostin, and G. H. M. van der Heijden. Triangular buckling patterns of twisted inextensible strips. *Proceedings of the Royal Society A*, 467(2125):285–303, 2010.

[41] N. Okuizumi, A. Muta, S. Matsunaga, H. Sakamoto, Y. Shirasawa, and O. Mori. Small-scale experiments and simulations of centrifugal membrane deployment of solar sail craft 'IKAROS'. In *52nd AIAA/ASME/ASCE/AHS/ASC Structures, Structural Dynamics and Materials Conference, Denver, Colorado*, page 1888, 2011.

[42] L. Wilson, S. Pellegrino, and R. Danner. Origami sunshield concepts for space telescopes. In *54th AIAA/ASME/ASCE/AHS/ASC Structures, Structural Dynamics, and Materials Conference, Boston, Massachusetts*, page 1594, 2013.

[43] D. J. S. Newman and R. J. Wootton. An approach to the mechanics of pleating in dragonfly wings. *Journal of Experimental Biology*, 125(1):361–372, 1986.

[44] C. J. C. Rees. Form and function in corrugated insect wings. *Nature*, 256(5514):200–203, 1975.

[45] H. Kobayashi, B. Kresling, and J. F. V. Vincent. The geometry of unfolding tree leaves. *Proceedings of the Royal Society of London. Series B: Biological Sciences*, 265(1391): 147–154, 1998.

Chapter 2

Bifurcations of anisotropic rods and thin bands under lateral end translations

The content of this chapter have appeared as is in the *Journal of the Mechanics and Physics of Solids*, volume 122, pages 657-685, 2019. The published paper can be found at: https://www.sciencedirect.com/science/article/pii/S0022509617307469.

Attribution

The work presented in this chapter was done in collaboration with J. A. Hanna, who contributed to the work through idea development, editing, and support.

Abstract

Motivated by observations of snap-through phenomena in buckled elastic strips subject to clamping and lateral end translations, we experimentally explore the multi-stability and bifurcations of thin bands of various widths and compare these results with numerical continuation of a perfectly anisotropic Kirchhoff rod. Our choice of boundary conditions is not easily satisfied by the anisotropic structures, forcing a cooperation between bending and twisting deformations. We find that, despite clear physical differences between rods and strips, a naive Kirchhoff model works surprisingly well as an organizing framework for the experimental observations. In the context of this model, we observe that anisotropy creates new states and alters the connectivity between existing states. Our results are a preliminary look at relatively unstudied boundary conditions for rods and strips that may arise in a va-

riety of engineering applications, and may guide the avoidance of jump phenomena in such settings. We also briefly comment on the limitations of current strip models.

2.1 Introduction

Thin rods and bands, the latter known also as strips or ribbons, display complex geometric response under simple end loadings and clampings. While much work has been done to explore these phenomena, most of the literature pertains either to periodic boundary conditions or highly symmetric end loadings such as a wrench, in which the end-to-end vector, loading vector, and twist are coaxial. Most of this is also limited to the analytically tractable case of isotropic rods; here and elsewhere in this paper, the term isotropic refers to the structure rather than the material, such that the cross section has no preferred bending direction. However, the space of possible boundary conditions is much wider, and includes conditions that can interact strongly with the anisotropy of a strip or any other elastic structure with a distinguished material frame. In many practical situations, the two ends of the structure may be clamped such that their material frames take any orientation with respect to each other and the end-to-end vector. As we will show, certain conditions conspire with the anisotropy to frustrate the system and couple its twist and writhe response. Clamped boundary conditions can not only create energy barriers through frustration, but may even introduce topological barriers between an undeformed ground state and excited states [1]. The present study is a preliminary exploration covering a small piece of this wider parameter space, as applied to anisotropic rods and bands. We begin with symmetrically clamped buckled strips of varying width, and subject their ends to a lateral displacement parallel to the width direction. The introduction of this "shearing" motion reveals a rich set of stable configurations and jump phenomena, including several snap-through instabilities, that to our knowledge do not appear in the literature (we encourage the reader to take a quick glance now at the supplementary video `widtheffect45.mp4` [2] to see examples of such stable states and snap-throughs). We compare experimentally determined stability ranges of various configurations to results from numerical continuation of the Kirchhoff rod equations, and find that a perfectly anisotropic rod model captures the complicated choreography of bifurcations of narrow bands, and provides much of the backbone of the behavior of wider bands. We reveal connections between various states, including higher-order unstable *elastica* modes and stable twisted states created by the rod's anisotropy.

While the Kirchhoff equations show themselves to be a surprisingly useful tool in the analysis of strip behavior, we wish to emphasize that there is no reason to assume that such a model, which assumes that cross sections remain perpendicular to the centerline, would be appropriate for strips. On the other hand, the common assumption that transverse bending of strips is governed by the constraint of developability can lead to difficulties of its own, particularly for narrow strips, issues that we will briefly touch upon in an appendix. Until such issues are resolved, it is advantageous to employ an easily implemented rod model from

which the strips inherit most, or even all, of their bifurcations. However, use of such a model should not be taken to imply that a narrow strip is equivalent to a rod.

Boundary conditions like those we explore here are potentially of interest in helping to avoid violent snap-throughs of connectors, hinges, and umbilicals in flexible and deployable systems. Geometries similar to ours appear as slipping folds [3] in deployable space membranes, buckled elements in flexible electronics and robotics, and decorative streamers in childrens' toys [4]. Multi-stable structures find use in compliant mechanisms [5] at all length scales. The behavior of strips under our loading conditions is likely related to the phenomenon of lateral-torsional buckling, known to structural engineers [6].

There is much prior work on the configurations of naturally straight rods. Work on the general behavior and classification of solutions includes that of Antman [7, 8], Maddocks [9], Nizette and Goriely [10], and Cognet and co-workers [11]. Neukirch and Henderson made a detailed investigation into the connectivity of solutions for rods subject to end thrusts and coaxial twists [12, 13]. Theory, numerics, and experiment show that circular cross section rods, an integrable system, when subject to such boundary conditions will buckle, hockle into a loop, or snarl into a self-contacting twisted structure [14, 15, 16, 17, 18, 19, 20, 21, 22]. Anisotropic rods, those with preferred bending directions, display even more complicated and potentially non-integrable behavior due to non-conserved twist [23, 24, 25, 26, 27, 28]. van der Heijden and Thompson [25] distinguish between weakly anisotropic and strongly anisotropic "tape-like" behavior such as that we will discuss in this paper. Integrability can also be destroyed by the addition of gravity [7, 29], but can be preserved under addition of extensibility and shearability [30, 31]. Early experiments by Green [32, 33] showed that twist under tension makes strips unstable to the formation of multiple loops, with only a single loop forming in the absence of tension. Recent work by Chopin and Kudrolli [34] extends these findings and reveals a rich set of possible deformations and patterns under tension and twist, many of them involving stretching. Aside from the present investigation, the only work we know of featuring lateral displacements is that of Morigaki and co-workers [35], who begin with a slightly laterally displaced loop configuration of a strip, pull the ends, and find behavior similar to the hockling and pop-out regimes of isotropic rods. Other interesting boundary conditions include freely hinged conditions [29, 36], and asymmetric rotation in the plane of buckling leading to snap-throughs [37]. Another much-studied corner of parameter space, due to its supposed relevance to DNA, is that of pre-twisted rings composed of isotropic or anisotropic rods [38, 39, 40, 41, 42, 43, 44]. The latter includes, as one particular case, the configurations of a narrow Möbius band [45, 46]. Dichmann, Li and Maddocks [47], Li and Maddocks 1996 [48], and Domokos and Healey [49] provide insight into the connectivity of various solutions of this type.

The current paper is organized as follows. We introduce the geometry of our problem and describe our experiments in Section 2.2, and present the anisotropic Kirchhoff rod model in Section 2.3. Results from experiments on narrow bands and numerical continuation of the Kirchhoff equations are compared in Section 2.4, through a series of slices through parameter space. In Section 2.5, a more global view is presented through the loci of bifurcation points

in parameter space, which also delineate regions of stability for different states. Experiments on bands of varying width are presented in Section 2.6 and compared with the results for narrow bands and rods. Many smooth and discontinuous bifurcations for both narrow and wide bands are shown in several supplementary videos [2], which complement the diagrams in Sections 2.4-2.6. We discuss a few additional points of interest in Section 2.7. In the Appendices, we show two types of configuration that exist as the bands approach the limits of developable deformation, where elastic energy focuses in conical defects at the clamped ends, give details on solving the boundary value problem, briefly discuss the minor effects of Poisson's ratio on the loci of bifurcation points, briefly contrast our results with those for isotropic (square) rods, and discuss problems that arise when employing strip models to describe the behavior of bands such as those in our experiments.

2.2 Geometry of the experiments, methods, and errors

The boundary conditions we impose are shown in Figure 2.1. We use thin (0.005 ±0.0005 inch / 0.127 ± 0.013 mm) bands cut from polyester shim stock (Artus Corp., Englewood, NJ) with free length $L = 240 \pm 0.5$ mm (≈ 5 mm clamped length on either side) and various widths, the most common being $D = 3 \pm 0.05$ mm, 30 ± 0.5 mm, and 60 ± 0.5 mm, corresponding to aspect ratios D/L of 1/80, 1/8, and 1/4, respectively. We use a Silhouette Cameo 3 cutting machine (Silhouette America, Lindon, UT) for the narrow bands, and a paper trimmer for the wider bands. The additional accuracy was necessary for narrow bands because bifurcations of highly twisted configurations were found to be sensitive to non-uniformities in width. With respect to an initially flat configuration, the boundary conditions consist of a symmetric tilt angle ψ_0 (±1°), a "compression" ΔL (±0.5 mm) in the length direction, and a lateral "shear" ΔD (±0.5 mm) parallel to the width direction at the ends. The clamping is parallel to the width direction with an accuracy of ±2° for $D/L = 1/80$, ±0.2° for $D/L = 1/8$, and ±0.1° for $D/L = 1/4$. Typically, we fix the compression and clamping angle, and use the normalized lateral shear displacement $\Delta D/L$ as the primary bifurcation parameter. We align the shear direction with gravity, which mitigates its influence. A bias of ≈ 0.5° in this alignment was introduced by the slope of the laboratory floor. We measure the range of stability for all observed configurations of the bands, many of which require manual manipulation to obtain. The bands are never kept in any particular deformed state for longer than a few minutes, to avoid possible viscous response that could affect results. With these precautions, results are reproducible with a typical variation of about ±2 mm (corresponding to ±1/120 $\Delta D/L$) between trials, although a very few narrow band states such as the $US\pm$ and W states at $\psi_0 = 60°$ show deviations of as much as ±5 mm. Near bifurcations that change connectivity, multiple trials may have qualitative differences; these are discussed when they arise in Section 2.4. All narrow band data come from averaging three trials; wide band data are single trials, other than some additional trials performed to estimate variation.

We describe the bands in terms of the geometry of a rod, a description that is most suitable

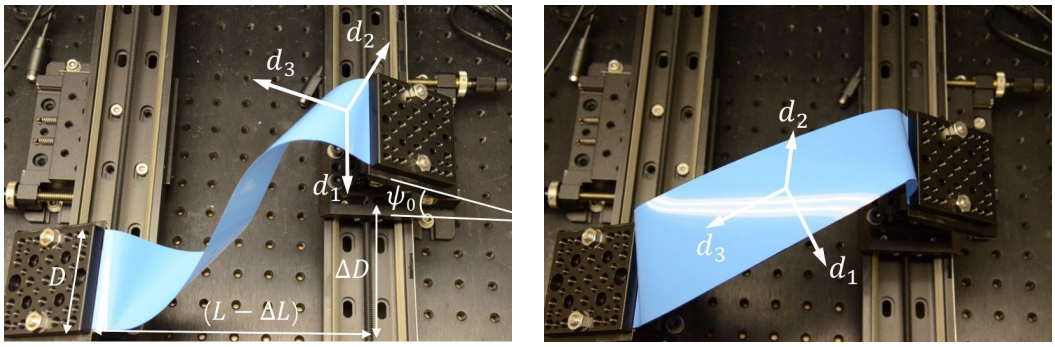

(a) (b)

Figure 2.1: A thin, rectangular band of width D and length L is symmetrically clamped with an angle ψ_0, "compression" ΔL, and "shear" ΔD. The centerline of the band carries an orthonormal director frame $(\boldsymbol{d_1}, \boldsymbol{d_2}, \boldsymbol{d_3})$ corresponding to the width direction, the surface normal, and the tangent, respectively. Shown here are (a) S-like and (b) U-like configurations.

for narrow bands, though quite distinct from the description of a band as a developable surface. The mechanics of an anisotropic rod will be discussed in the following section. The description involves an orthonormal material frame $(\boldsymbol{d_1}, \boldsymbol{d_2}, \boldsymbol{d_3})$ attached to the centerline of the band, with the three directors corresponding to the width direction, the surface normal, and the tangent, respectively. Figure 2.1 shows such a frame superimposed on two example configurations of a wide band, which we refer to as S-like and U-like, and which we will describe in more detail in Section 2.4.

Bands can, in theory, be approximated as developables until the shear displacement $\Delta D/L$ approaches a limiting value where such an isometric description is no longer possible. We discuss this further in Appendix A.1. Note that in describing the bands as developable surfaces, the straight line generators of the surface would not coincide with the material directors of the rod description; the geometry of a developable strip differs from that of a rod with undeformed cross section. Further comment can be found in Appendices A.2 and A.5.

2.3 Anisotropic rod model

We compare experimental results with a simple model of a perfectly anisotropic rod. This model assumes that the only way a band can deform is by bending around its width direction and twisting around its tangent. Bending around the surface normal is forbidden. The rod is inextensible and unshearable; its centerline is given by $\boldsymbol{X}(s)$, where s is the arc length, and the tangent can be identified with one of the directors, $\boldsymbol{X}' = \boldsymbol{d_3}$ (throughout this paper

a prime will denote an s-derivative). The kinematics of the frame $(\boldsymbol{d_1}, \boldsymbol{d_2}, \boldsymbol{d_3})$ are given by

$$\boldsymbol{d_i'} = \boldsymbol{\omega} \times \boldsymbol{d_i}\,, \tag{2.1}$$

$$\boldsymbol{\omega} = \kappa_1 \boldsymbol{d_1} + \tau \boldsymbol{d_3}\,, \tag{2.2}$$

where the Darboux vector $\boldsymbol{\omega}$ has no component normal to the strip. The generalized strains κ_1 and τ are the curvature in the easy (only) direction, and the twist about the tangent. For a perfectly anisotropic strip, the frame $(\boldsymbol{d_1}, \boldsymbol{d_2}, \boldsymbol{d_3})$ can be identified with the Frenet-Serret frame as $(\boldsymbol{b}, \boldsymbol{-n}, \boldsymbol{t})$, and the curvature κ_1 and twist τ with the curvature and torsion. This type of model has been used previously as an approximate model for the shape of elastic strips [45]; our present interest is primarily in bifurcations rather than shapes.

Linear and angular momentum balances are provided by the Kirchhoff equations for the contact force and moment $\boldsymbol{N}$ and $\boldsymbol{M}$ in the absence of gravity or other distributed loads or couples,

$$\begin{aligned} \boldsymbol{N'} &= \boldsymbol{0}\,, \\ \boldsymbol{M'} + \boldsymbol{d}_3 \times \boldsymbol{N} &= \boldsymbol{0}\,. \end{aligned} \tag{2.3}$$

Three quantities are conserved along the centerline [20],

$$\begin{aligned} C_1 &= \tfrac{1}{2}\boldsymbol{M} \cdot \boldsymbol{\omega} + \boldsymbol{N} \cdot \boldsymbol{d_3}\,, \\ C_2 &= \boldsymbol{N} \cdot \boldsymbol{N}\,, \\ C_3 &= \boldsymbol{N} \cdot \boldsymbol{M}\,. \end{aligned} \tag{2.4}$$

Isotropic rods conserve the twist as a fourth quantity; our system does not. The general anisotropic rod is known to be non-integrable, but we are unaware of any published results on the presence or lack of integrability for the perfectly anisotropic case. We resolve $\boldsymbol{N}$ and $\boldsymbol{M}$ on the moving frame as $\boldsymbol{N} = N_i \boldsymbol{d}_i$ and $\boldsymbol{M} = M_i \boldsymbol{d}_i$, and assume linear constitutive relations $M_1 = EI_1\kappa_1$ and $M_3 = GJ\tau$, where E is the Young's modulus and G is the shear modulus, I_1 is the principal moment of inertia of the cross-section in the easy direction, and GJ is the torsional rigidity. The other moment M_2 is a Lagrange multiplier enforcing the vanishing of curvature in the hard $\boldsymbol{d_2}$ direction. The ratio of E to G involves the elastically isotropic Poisson's ratio ν, which we set to 0.25 for the present study; this choice makes little difference to the results, as shown in Appendix A.3. There are thus six scalar balance equations. Reconstruction of the rod centerline and frame orientation is achieved through a quaternion representation leading to a set of thirteen equations. We solve these using the continuation package AUTO 07P [50]. Details, along with the specification of boundary conditions, are discussed in Appendix A.2.

2.4 Numerical and experimental results for narrow bands

In this section, we present experimental results on narrow bands ($D/L = 1/80$) and compare them with numerical results from the anisotropic Kirchhoff rod model. We restrict our

experimental parameter space to a single compression $\Delta L/L = 1/2$ and clamping angles $0 \le \psi_0 \le 60°$. Using the shear $\Delta D/L$ as a bifurcation parameter, we deform the bands to near the isometric limit, and find a rich and complicated landscape of stable configurations and both smooth and violent transitions. These observations, which depend strongly on clamping angle, are described surprisingly well by the naive model. We keep gravity out of the model, as its effects are easily accounted for, and in practical terms it would simply break some of the symmetry of the solutions we wish to explore and create more complicated and potentially confusing figures.

The boundary conditions we impose might be easily accommodated by an isotropic rod bending in what is a forbidden direction for the perfectly anisotropic strip. Instead, our frustrated system is induced to find some combination of allowed bending and twist in order to satisfy the constraints. In short, the shear indirectly causes a non-uniform twist, and as there are multiple ways for bending and twisting energy to compete, creates a highly multi-stable system. As the shear increases, the system shifts from being compressed to being in tension. To our knowledge, these boundary conditions have not been explored before in the literature. However, Morigaki's [35] recent experiments on tensioned loops can be interpreted in terms of our boundary conditions as a clamping angle ψ_0 of 180°, large compression ($\Delta L/L > 1$), and small shear $\Delta D/L$.

In general, the clamping angle will bias the strip towards two general types of configurations, with some seeming similarity to primary buckling modes of planar *elastica*. Small clamping angles favor S-like shapes that live both above and below the plane of clamping, and come in chiral pairs. High clamping angles favor U-like shapes that live mostly on one side of the plane of clamping, and are symmetric about their midpoints. Examples are shown in Figure 2.1. This is consistent with what is known about the rod equations, namely that all solutions are either reversibly symmetric about their midpoint or are reversibly symmetric pairs [12, 18, 49]. As we increase the clamping angle, we gradually lose many of the states that exist at low angles.

Figure 2.2 shows all the types of states we observe in narrow bands, alongside renderings based on numerical solutions of the perfectly anisotropic rod equations, for a shallow clamping angle $\psi_0 = 15°$ and various values of shear $\Delta D/L$. We name the states in a manner that roughly describes their shapes. There are no fitting parameters; boundary conditions and viewing angle are the same between experiments and numerics. The numerical solutions are rendered as strips representing the rod frame (Appendix A.2), with the same width as the actual bands, but we note that *the actual bands will deform into a surface that is different than the surface representing the rod frame*, so comparisons must be made carefully. Throughout this paper, we are able to identify experimental and numerical states using a combination of factors including symmetry of the shapes and the number of inflections in centerline curvature and twist, rather than from details of the shape adopted by material off of the centerline. For later comparison with Figures 2.11 and 2.17 one needs to know that $s/L \in [0, 1]$ increases from right to left in the renderings.

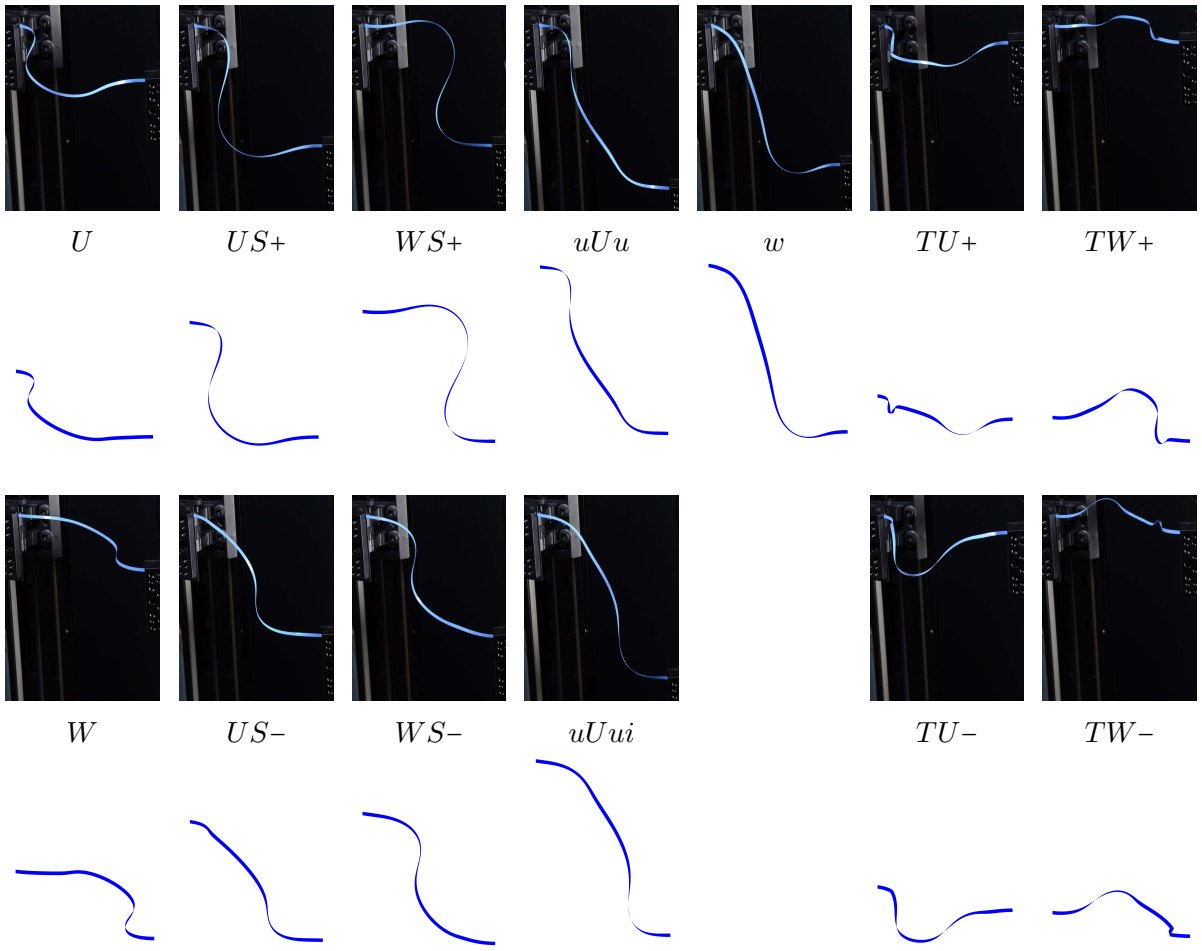

Figure 2.2: Comparison between experimental configurations of a narrow band ($D/L = 1/80$) and renderings of the rod frame based on numerical solutions of the perfectly anisotropic rod equations, with compression $\Delta L/L = 1/2$, clamping angle $\psi_0 = 15°$, and various values of shear $\Delta D/L$. Note that the bands deform into a surface different than the rod frame rendering. There are no fitting parameters; boundary conditions and viewing angle are the same between experiments and numerics. Gravity is roughly vertical in the experimental images, and is absent in the numerical solutions; its effects are greatest on the twisted solutions $TU\pm$ and $TW\pm$. Thirteen states are shown, including four symmetric $\pm$ pairs.

Gravity is roughly vertical in the experimental images, and is absent in the numerical solutions. Its effects are generally weak, although stronger on some solutions such as the overhanging twisted solutions $TU\pm$ and $TW\pm$. Overall, the Kirchhoff equations reproduce the shapes of stable states quite well. Thirteen states are shown, but this includes four symmetric $\pm$ pairs, so only nine distinct states exist. We may classify them into three families. First we define a coordinate y perpendicular to the clamping plane, sharing the same sign as ψ_0. The U family (U, $US\pm$, uUu and w) and W family (W, $WS\pm$ and $uUui$) tend to sit

on the side of positive and negative y, respectively, and are mirror images when $\psi_0 = 0°$. A family of twisted states ($TU\pm$ and $TW\pm$, mirror images when $\psi_0 = 0°$) exists at low values of shear. These states, which clearly display the non-conservation of twist in anisotropic rods, can be achieved by applying a twist near the center of a U or W state. Alternatively, we may separate the states into reversibly symmetric ± pairs and reversibly symmetric single solutions.

We now present a sequence of slices through parameter space for increasing values of clamping angle $0 \le \psi_0 \le 60°$, showing the evolving solution manifolds and corresponding rod shapes for the Kirchhoff equations alongside experimentally determined ranges of stability of narrow band states. It is not difficult to link observed states with numerical solutions through qualitative comparison of the shapes and inferences about stability information from the types of bifurcations encountered. Changes in connectivity of the solution manifolds are also reflected in experimental data and verified in supplementary videos [2]. The slices will display the connectivity of the solution curves before and after certain transitions. These transitions are pinpointed more accurately using two-parameter continuation of bifurcation points in clamping angle-shear space, as will be shown in more detail in Figure 2.18 in Section 2.5. The shear $\Delta D/L$ is the bifurcation parameter. The system is mirror-symmetric around zero shear, but we plot a small portion of the numerical negative shear results to show the loop structure of various states near the origin. For the vertical (response) axis, we choose the integrated height above the plane of clamping $\int_0^1 y\,ds$, a quantity that converges to zero for all states as the limiting shear deformation is approached, and which is identical for each ± pair. A strip of finite width has a shear limit, discussed in Appendix A.1, beyond which stretching must occur. For a compression $\Delta L/L = 1/2$, this limit is $\Delta D/L \approx 0.854$ for our narrow bands, and $\Delta D/L = \sqrt{3}/2 \approx 0.866$ for an ideal rod with zero width. We perform narrow-band experiments and continue solutions only up to 0.82, which avoids damaging the band as well as numerical stiffness issues. Solution manifolds are obtained by continuation of angle and/or displacement boundary conditions from known solutions, typically from a circle deformed through the first buckled mode of planar *elastica*. Some branches, such as twisted state branches, are isolated on the cross sections we present but can be reached by continuation in the full parameter space. Curves we wish to emphasize are plotted in black, while other closely related or connected curves are shown in grey; often, particularly at higher angles, black and grey will be used for different portions of a single continuous curve. We show more of these grey curves at lower angles on some of the plots, and replace them with dashed lines at higher angles, and often remove them entirely to overlay additional numerical or experimental results. Stability information is not shown anywhere on these plots, although it can often be inferred. An infinite number of other states exist, and are of course not shown. Branch points, and occasionally some fold bifurcations, are marked with symbols; unmarked intersections of the manifolds do not correspond to any bifurcation. Because of the ± symmetry of the integrated height response parameter $\int_0^1 y\,ds$, most pitchfork bifurcations look like half of a pitchfork, as two lines overlap. Numbers on the figures identify particular bifurcations whose loci will be shown later in Figure 2.18 in

Section 2.5.

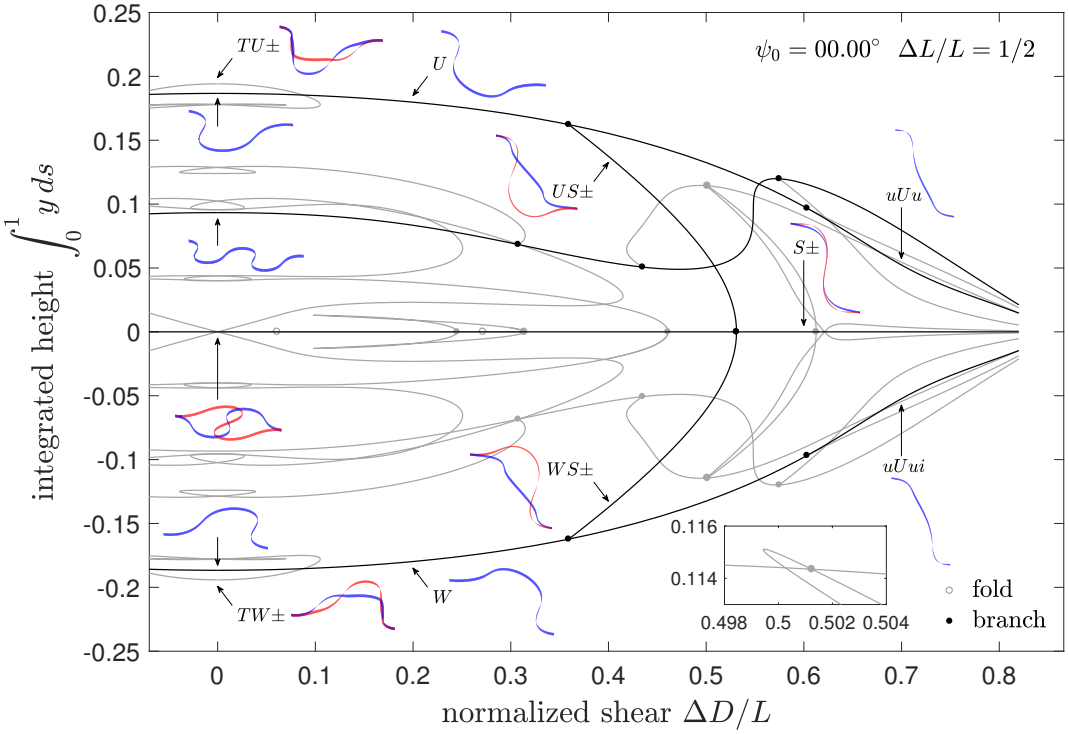

Figure 2.3: Some solutions (curves and renderings from the arrowed locations) and bifurcations (disks) of the perfectly anisotropic Kirchhoff rod for clamping angle $\psi_0 = 0°$. Stability information is not shown; black and grey are used for emphasis only. The solution curves are symmetric about the zero-height axis and the zero-shear axis. Red and blue shapes are ± pairs that share a single curve on the diagram.

Figure 2.3 shows some of the solution manifolds for the symmetric case of zero clamping angle $\psi_0 = 0°$. Also shown are rod frame renderings of numerical solutions at several points along the curves, many of which we identify with the configurations named in Figure 2.2. The ± pairs are drawn as red and blue. Several turning points (fold bifurcations) and branch points are observed, some of which are overlapping pairs. The states shown include the first few stable and unstable planar modes of Euler *elastica*, which are unlabeled. The loop-like curves near zero shear are highly twisted states, many of which are unstable, some of which connect with the *elastica* modes. All even-numbered modes of planar elastica and states continued from these will sit on top of one another on the horizontal axis of symmetry (zero integrated height). The connectivity along this axis is very complicated, including many (possibly an infinite number) of branch and fold bifurcations, as will be revealed when we proceed to a nonzero value of ψ_0. We show only a few branch points here, and our choice of response parameter hides the presence of folds when $\psi_0 = 0$. This raises interesting questions. Can we assume that the entire infinite family of planar buckled modes connect through bifurcations to one or more twisted states? And how are the pitchforks distributed along the axis?

We are able to identify these numerical states with the stable states observed experimentally, and infer information about stability and bifurcation types. We now recognize that the U and uUu states lie on a single branch connected to the first-mode planar *elastica*, but are separated by two bifurcations and an unstable stretch. We will refer to this entire branch as the U branch, except when it may cause confusion. There is a supercritical pitchfork at $\Delta D/L \approx 0.36$ that connects the U and $US\pm$ states and causes loss of stability of the U branch; stability is regained through a subcritical pitchfork at $\Delta D/L \approx 0.60$, with the second set of stable configurations referred to as uUu. There are two supercritical pitchforks on the zero-height axis of symmetry at $\Delta D/L \approx 0.53$, one linking the $US+$ and $WS+$ states to a stable $S+$ state, the other linking the $US-$ and $WS-$ states to a stable $S-$ state. The $S\pm$ states only exist at zero clamping angle, because the pitchforks on the horizontal axis will be broken at any non-vanishing angle. The unstable states on the low-shear side of these bifurcations connect back to the two unstable second-mode *elastica* shapes shown at zero shear. Note that at zero clamping angle, the US and WS states are equivalent. Upon symmetric change in the clamping angle, they will be distinct, and the connectivity described here will change. In this study, we don't consider asymmetric changes in clamping angle, which observation suggests will stabilize either the second-mode *elastica* or a pair of S-like planar shapes, depending on the value of the compression. By shearing the unstable third-mode *elastica* and following the branch to high shear, we encounter three branch points, none of which appear to create any stable states. Between the second and third of these, there is a steep, but not yet folded back, section of the curve that will, upon a small change of clamping angle, become a stable section in between two folds. We plot the companion curve below the horizontal axis in grey, as it will never acquire a stable segment. Of the many twisted states at low shear, only two pairs of twisted states $TU\pm$ and $TW\pm$ (equivalent at zero clamping angle) are observed experimentally. The two loops upon which they lie are complicated pretzel-like curves, each of which provides four (pairs of) states at zero shear, of which only one is experimentally observed in narrow bands.

In Figure 2.4, we compare the solutions of the anisotropic rod equations with experimental narrow band stability data for $\psi_0 = 0°$, shown using red curves. No experimental data was obtained for negative shear, so the data is truncated at the $\Delta D/L = 0$ axis. Many solution curves have been removed from the figure for clarity. Only the horizontal extent of the red experimental curves has any meaning. The vertical position of these curves follows the corresponding solutions for ease of comparison, with $\pm$ pairs separated by a small gap, or the data is plotted as a horizontal line if no corresponding solution exists. For example, the very short red line representing the w state is observed experimentally, although in theory it should not appear until the clamping angle is slightly increased to $\psi_0 \approx 0.135°$. This discrepancy is likely due to some error in clamping or in vertical alignment in the presence of gravity; the system can be quite sensitive to boundary conditions close to a bifurcation. Similar comments can be made about any other asymmetries about the horizontal axis at $\psi_0 = 0°$. In this and subsequent figures, gravity is responsible for observed asymmetries between $\pm$ pairs, breaking pitchfork bifurcations like that between the U and $US\pm$ states, such that U always connects with $US+$. The $US-$ and $WS+$ states are thus isolated states

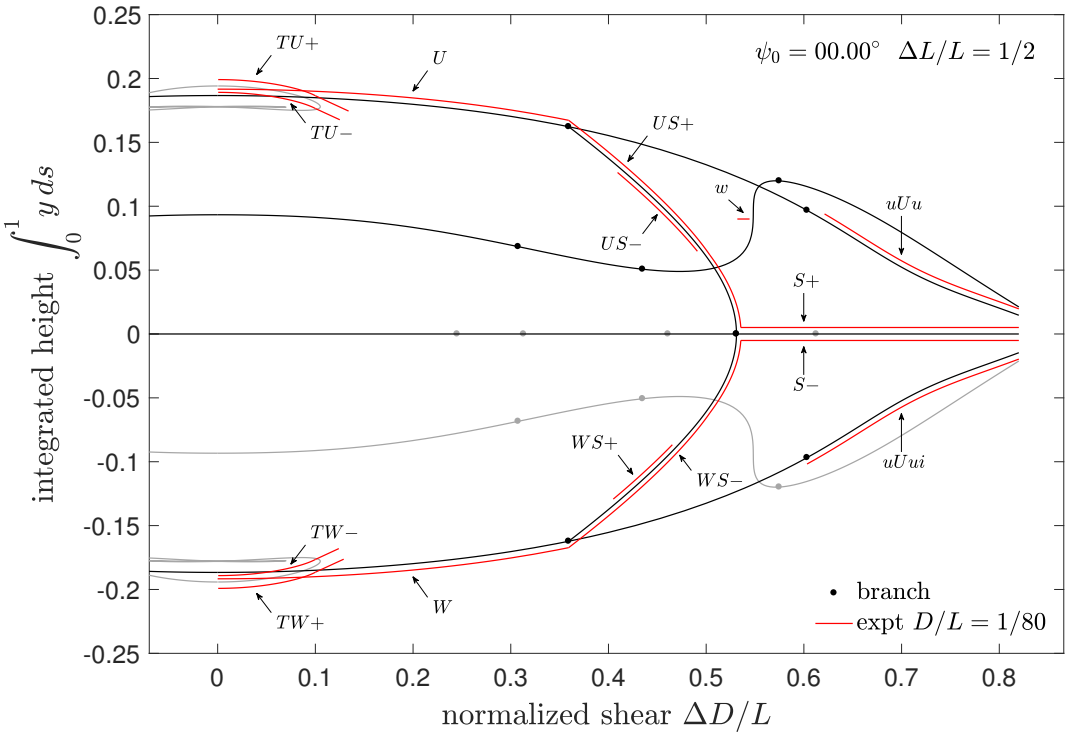

Figure 2.4: Experimental data (red curves) from narrow bands for clamping angle $\psi_0 = 0°$, compared with numerical solutions of the anisotropic rod equations (black and grey curves). Some solution curves branching from bifurcation points have been removed from the diagram for clarity. The horizontal extent of the red curves is the range of stability (typical variation $\approx \pm 0.01\,\Delta D/L$), while the vertical position of the curves is not measured data, but is made to follow near the numerical curves whenever a comparison is possible. No data was taken for $\Delta D/L < 0$. Gravity causes asymmetry between $\pm$ data. A stable w state does not theoretically appear until $\psi_0 \geq \approx 0.135°$, but is observed in experiments, likely due to error in clamping or alignment. There is a smooth path from the first mode of planar *elastica*, through the U, $US+$, and $S+$ states or the W, $WS-$, and $S-$ states, to approach the limiting shear.

in between two fold bifurcations, and observed only by manual manipulation of the band, only because of the presence of gravity in a particular orientation. This qualitative behavior was confirmed by augmenting the rod equations with a gravity term (see equations (A.15) in Appendix A.2). We observe that a first-mode *elastica* will smoothly deform through the U, $US+$, and $S+$ states or through the W, $WS-$, and $S-$ states, to approach the limiting shear, with the $\pm$ choices being results of gravitational bias in this orientation. This process, and many other bifurcations corresponding to Figure 2.4, are illustrated in the supplementary video `transition0.mp4` [2]. We will see that the numerical W-WS-S path will be broken by any nonzero clamping angle, while the U-US-S path will become a U-US path at nonzero angle, and will eventually be broken at higher angles, with two merging events leading to

a new smooth U-w-$uUui$ path. At $\psi_0 = 0°$, the uUu and $uUui$ states also approach the limiting shear, but are not smoothly connected to planar configurations.

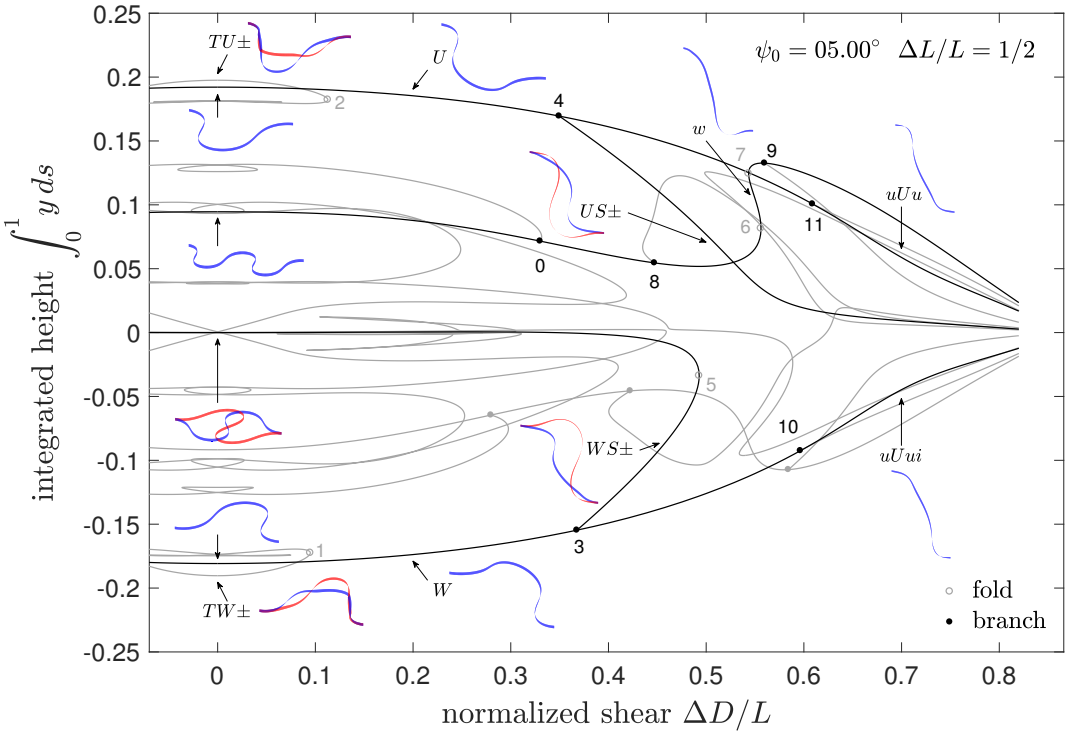

Figure 2.5: from narrow bands for Some solutions (curves and renderings from the arrowed locations) and bifurcations (open and closed disks, some numbered) of the perfectly anisotropic Kirchhoff rod for clamping angle $\psi_0 = 5°$. Many bifurcations have been broken, and paths approaching the limit have been affected. Two folds 6 and 7 and the w state have been created.

Figures 2.5 and 2.6 show some solution manifolds, renderings, and experimental stability data for a small clamping angle, $\psi_0 = 5°$. In Figure 2.5 and some subsequent figures, some bifurcations have been numbered for convenient description and for further discussion in Section 2.5 and Appendix A.3. The nonzero clamping angle has broken the symmetry between the U and W families that live primarily above and below the horizontal axis in the figures. At low shear, we can think of U as the primary first-mode *elastica* state, and W as the corresponding inverted state (as the clamping angle increases, its shape will more closely resemble its name, or perhaps an M depending on one's orientation). All the branch bifurcations on this axis, and some off of the axis, have been broken, creating numerous folds, and revealing the complex asymmetric connectivity of the curves. The breaking of the primary black pitchforks on the horizontal axis leads to the overlapping fold bifurcation pair 5 on the $WS\pm$ branch, now separated by a jump from the $US\pm$ branch, which branch has now merged with $S\pm$ and smoothly approaches the limiting shear. Further increases in angle will shorten the stable range of the $WS\pm$ branch. Two folds 6 and 7 and an intermediate w

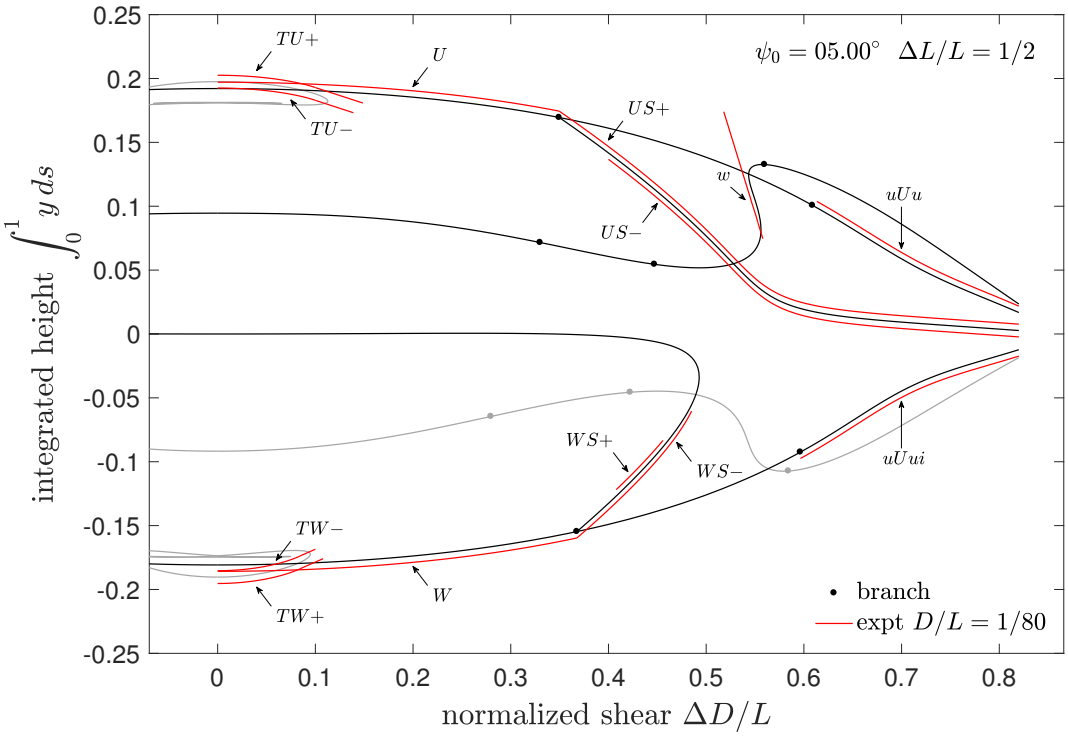

Figure 2.6: Experimental data (red curves) from narrow bands for clamping angle $\psi_0 = 5°$, compared with numerical solutions of the anisotropic rod equations (black and grey curves). Many solution curves have been removed from the diagram for clarity. The horizontal extent of the red curves is the range of stability (typical variation $\approx \pm 0.01\,\Delta D/L$), while the vertical position of the curves is not measured data, but is made to follow near the numerical curves whenever a comparison is possible. No data was taken for $\Delta D/L < 0$. There is still a smooth path from the first mode of planar *elastica*, through the U and $US+$ states, to approach the limiting shear, but the corresponding path through $WS-$ has been broken; $WS\pm$ states will now jump to $US\pm$ states at intermediate shears.

state have been created on an upper black branch. The creation occurs at $\psi_0 \approx 0.135°$ and corresponds to a cusp in ψ_0-$\Delta D/L$ space, which will be seen later in Figure 2.18. Increasing the clamping angle extends the stable range of the w state; the corresponding inverted grey branch becomes shallower in slope, and will never produce a stable state under our choice of clamping path. All of these features of the rod equation solutions are consistent with the experimental data.

In subsequent figures, we remove many of the complicated grey solution curves, indicating their existence with small stretches of dashed lines.

Figure 2.7 shows some solution manifolds and experimental stability data for a clamping angle $\psi_0 = 15°$. Paths from zero to limiting shear have not changed. However, the stable extent of the w state has increased, while that of the $WS\pm$ states has decreased, with

$WS+$ nearly disappearing due in part to the gravity-induced asymmetry. The primary twisted states $TU\pm$ are relatively unaffected by the clamping angle change, but their inverted partners, the $TW\pm$ states, now exist over a shorter extent. In experiments, we observe that the $WS\pm$ states jump to the corresponding $US\pm$ states upon increasing shear, while the $WS+$ state jumps to the $WS-$ state, and the $US-$ state jumps to the $US+$ state, upon decreasing shear, due to gravity-induced folds. The w state jumps to the limiting $uUui$ state upon increasing shear, and to the $US+$ branch upon decreasing shear. Many of these transitions are illustrated in the supplementary video `transition15.mp4` [2]. We note that much of the complexity of the solution manifolds arises from the anisotropy of the rod; Appendix A.4 shows relatively simple solution manifolds for isotropic rods that may be compared with Figures 2.3 and 2.7.

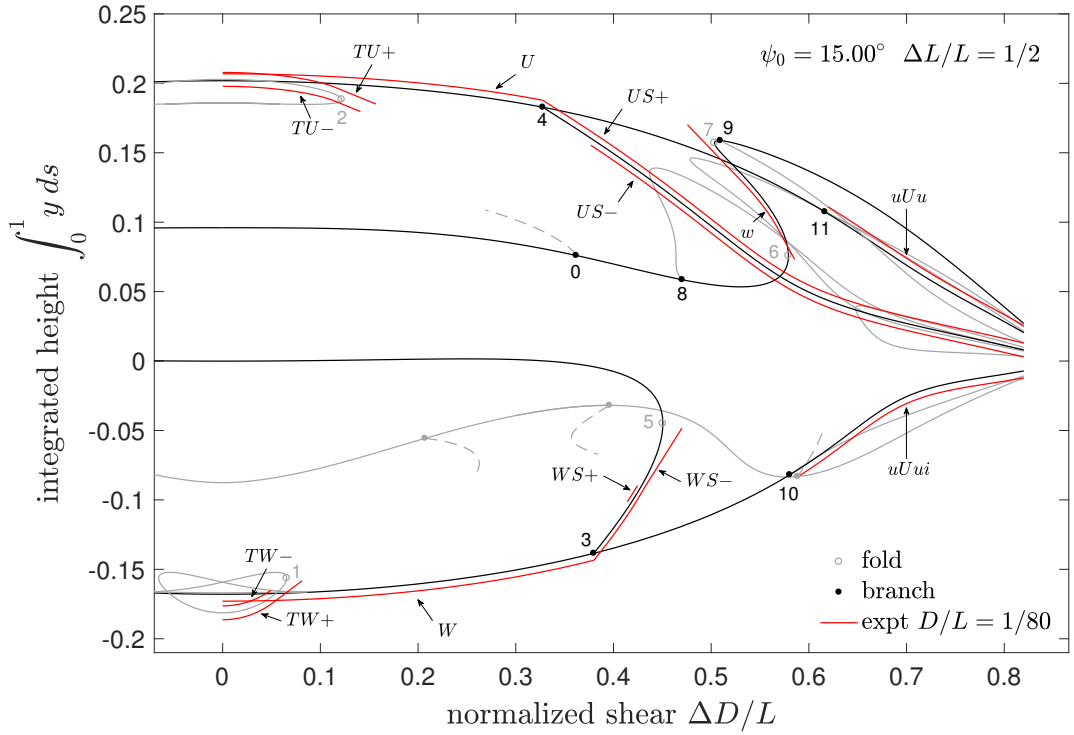

Figure 2.7: Some solutions (black and grey curves) and bifurcations (open and closed disks, some numbered) of the perfectly anisotropic Kirchhoff rod equations for clamping angle $\psi_0 = 15°$, along with experimental data (red curves). The horizontal extent of the red curves is the range of stability (typical variation $\approx \pm 0.01\,\Delta D/L$), while the vertical position of the curves is not measured data, but is made to follow near the numerical curves whenever a comparison is possible. No data was taken for $\Delta D/L < 0$. Numerically, the w branch has been elongated, and the $WS\pm$ and $TW\pm$ branches have been shortened. Experimentally, the $WS+$ state has nearly disappeared, in part due to the action of gravity.

As we increase the clamping angle, there are many complicated changes to the solution structure. Among these, the isolated $TW\pm$ loop partially merges with some of the compli-

cated grey twisted curves (which we have already removed from the figures for clarity). The stable $TW\pm$ states disappear at around $\psi_0 \approx 26.89°$. We don't show these, and many other, transitions here.

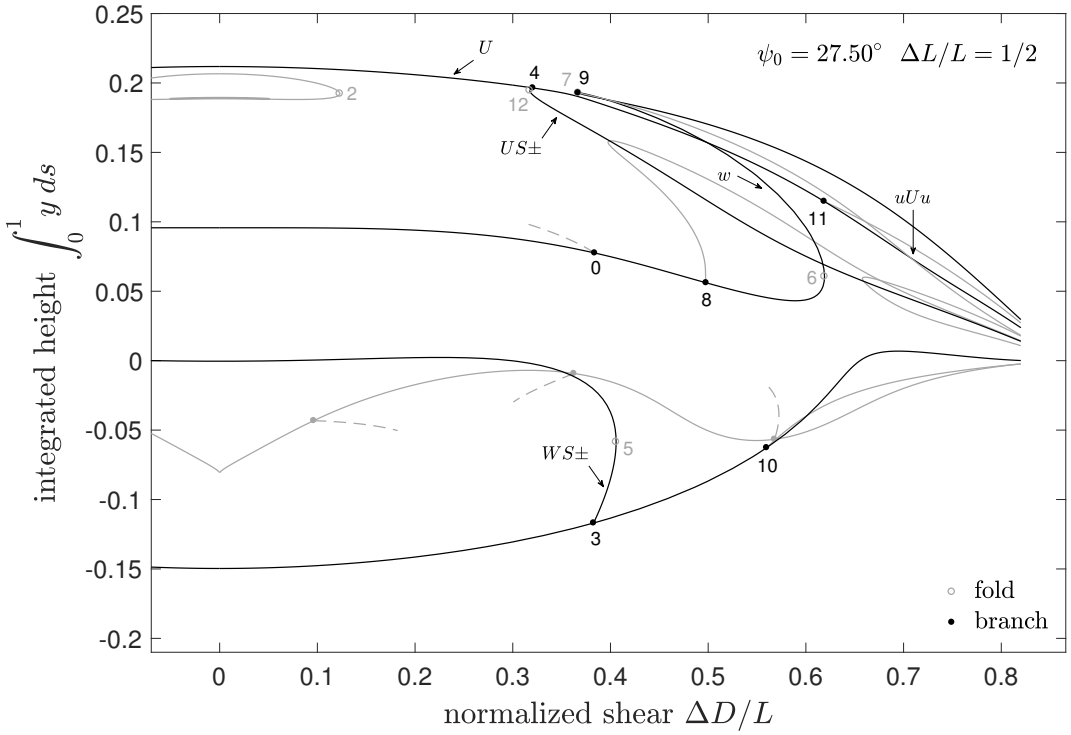

Figure 2.8: Some solution curves and bifurcations (open and closed disks, some numbered) of the perfectly anisotropic Kirchhoff rod for clamping angle $\psi_0 = 27.5°$. Pitchfork 4 has transformed from super- to sub-critical, and a new fold 12 has appeared. The U state will now (weakly) jump to a US branch, which can be followed to the limit. Fold 7 of the w branch is approaching the U branch. Details of this region and subsequent transitions are shown in Figure 2.9.

Some solution manifolds at $\psi_0 = 27.5°$ are shown in Figure 2.8. The $WS\pm$ branch has nearly disappeared. At $\psi_0 \approx 26.29°$, pitchfork bifurcation 4 transforms from super- to sub-critical, and a new fold bifurcation 12 appears. This means that the U-US path is no longer smooth. Fold bifurcation 7 of the w branch is approaching the U branch, and will merge through a complicated sequence shown in detail in Figure 2.9. At $\psi_0 \approx 27.71°$, the branch containing the w state touches the U branch, and then splits to form two new folds 13 and 18. This causes the uUu branch to detach from the U branch and attach to the unstable part of the w branch to form an isolated branch that emerges from and loops back to the limiting shear. At $\psi_0 \approx 27.75°$, folds 18 and 7 annihilate each other through a cusp in the $\Delta D/L - \psi_0$ plane. Subcritical pitchfork 4 and branch point 9 annihilate each other at $\psi_0 \approx 28.15°$; it appears that we can identify point 9 as a subcritical pitchfork at least for the small window of angles preceding this annihilation event, although stability information inferred from experiments

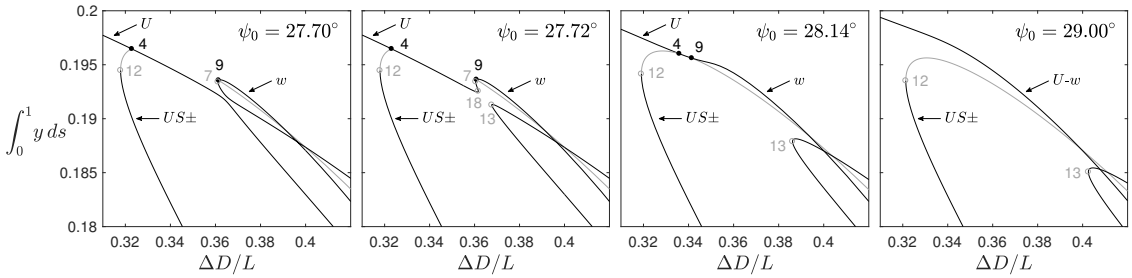

Figure 2.9: Details of several transitions that change the connectivity of solution curves. Closed and open disks are branch and turning points, respectively. First, the w branch collides with the U branch, and the high-shear portion that includes the uUu branch detaches from U and attaches to part of w. Then, folds 18 and 7 annihilate. Then, subcritical pitchforks 4 and 9 annihilate, detaching the $US\pm$ branches from the U branch, while U attaches smoothly to w.

does not allow us to make this identification in general. This annihilation process detaches the $US\pm$ branches from the U branch, while U attaches smoothly to w so that they are no longer distinct states, and the U-US transition no longer occurs. Now the primary first and third modes of planar *elastica* are on the same curve, separated by a fold 6 and two branch points 8 and 0.

Figure 2.10 shows some solution manifolds and experimental stability data for a clamping angle $\psi_0 = 30°$. Both the $US\pm$ and uUu branches are clearly detached from what is now the U-w branch, which is approaching and will soon collide with the $uUui$ branch. Due to proximity to bifurcations that change connectivity of the solutions, the experimental data is not all consistent. We draw red dotted lines to indicate that we often observe smooth transitions from U-w to $US+$ and from $uUui$ to U-w, though at least half of the time these transitions do not occur and the data follow qualitatively with the numerical solutions. The solid red lines correspond to these "correct" data. Clearly, the system is sensitive to the presence of two nearby bifurcations in parameter space. The jump from U-w to $uUui$ is weak and hard to observe. This is now the main path to the limiting shear.

At $\Delta D/L = 0.625$, there are five stable states. Figure 2.11 shows the numerically determined axial force N_3, the curvature κ_1, the twist τ, and the energy density $\varepsilon = \frac{1+\nu}{2}\kappa_1^2 + \tau^2$, with $\nu = 0.25$, for these states. At this value of shear, all states have a higher energy density near the clamps than in the middle. Interestingly, we observe that the uUu state (primarily above the clamping plane) is purely tensile ($N_3 > 0$), while the corresponding $uUui$ state (primarily below the clamping plane) is compressive towards its ends and slightly tensile in the middle, although the depression at the center can be compressive at lower values of shear. In general, higher shear will lead to increased tension as the limiting states are approached.

At $\psi_0 \approx 30.62°$, the U-w branch collides with the $uUui$ branch. This merge-split event leads to a continuous U-w-$uUui$ path from first mode planar *elastica* to approach the limiting shear.

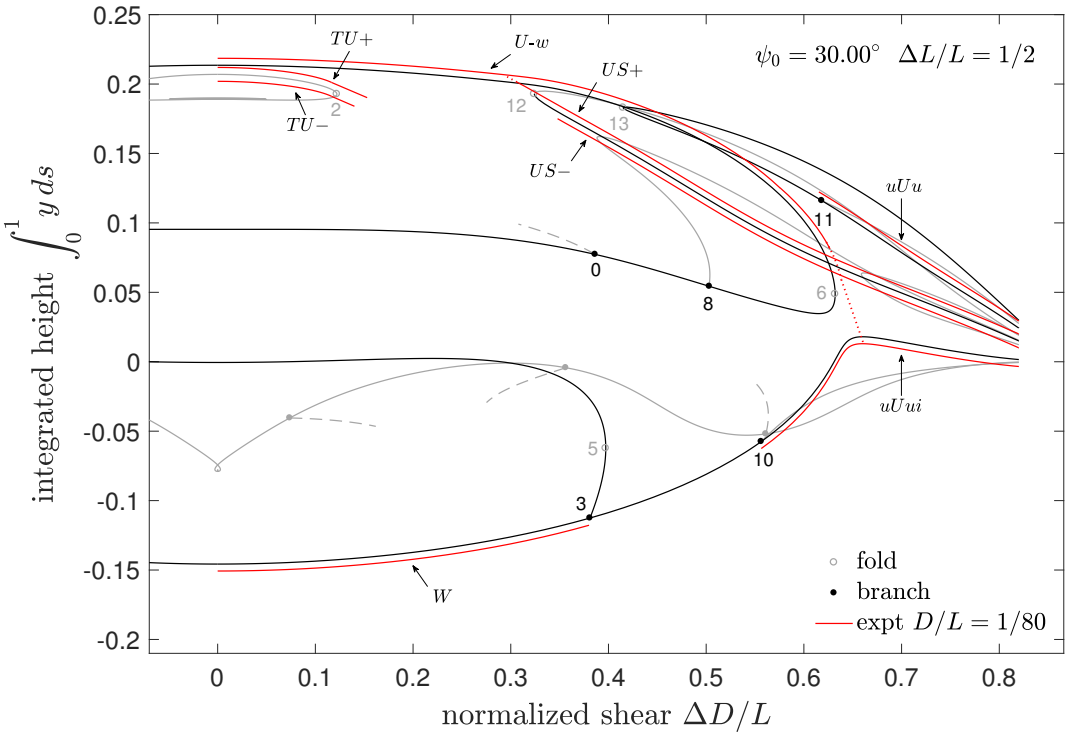

Figure 2.10: Some solutions (black and grey curves) and bifurcations (open and closed disks, some numbered) of the perfectly anisotropic Kirchhoff rod equations for clamping angle $\psi_0 = 30°$, along with experimental data (red curves). The horizontal extent of the red curves is the range of stability (typical variation $\approx \pm 0.01\,\Delta D/L$), while the vertical position of the curves is not measured data, but is made to follow near the numerical curves whenever a comparison is possible. No data was taken for $\Delta D/L < 0$. Numerically, the newly formed U-w branch, which terminates in a fold rather than reaching the limit, is approaching the $uUui$ branch. Red dotted lines indicate that sometimes smooth transitions from U-w to $US+$ and from $uUui$ to U-w are observed, which is inconsistent with the rest of the data (red solid lines) and the connectivity of the numerical solutions.

However, part of the original $uUui$ branch remains, and can be seen between pitchfork 10 and a new fold 14 in Figure 2.12. Figure 2.12 shows some solution manifolds and experimental stability data for a clamping angle $\psi_0 = 37°$. Now the primary third mode and the inverted first mode of planar *elastica* are on the same curve, separated by several branch points 3, 10, 8, and 0, and a fold 14. The $WS\pm$ states have a very narrow extent, and will soon disappear (at $\psi_0 \approx 41.74°$) as the supercritical pitchfork 3 absorbs the fold 5 and becomes subcritical, a process we will clearly see later in Figure 2.18. Already we do not observe them in the experiments. Some of the grey curves in the lower half of previous figures, including the inverted third mode counterpart to the upper branch that contains the w state, have been removed, as they have collided with other very complicated states that we have already removed. We retain a small grey hairpin curve near the limiting shear, as

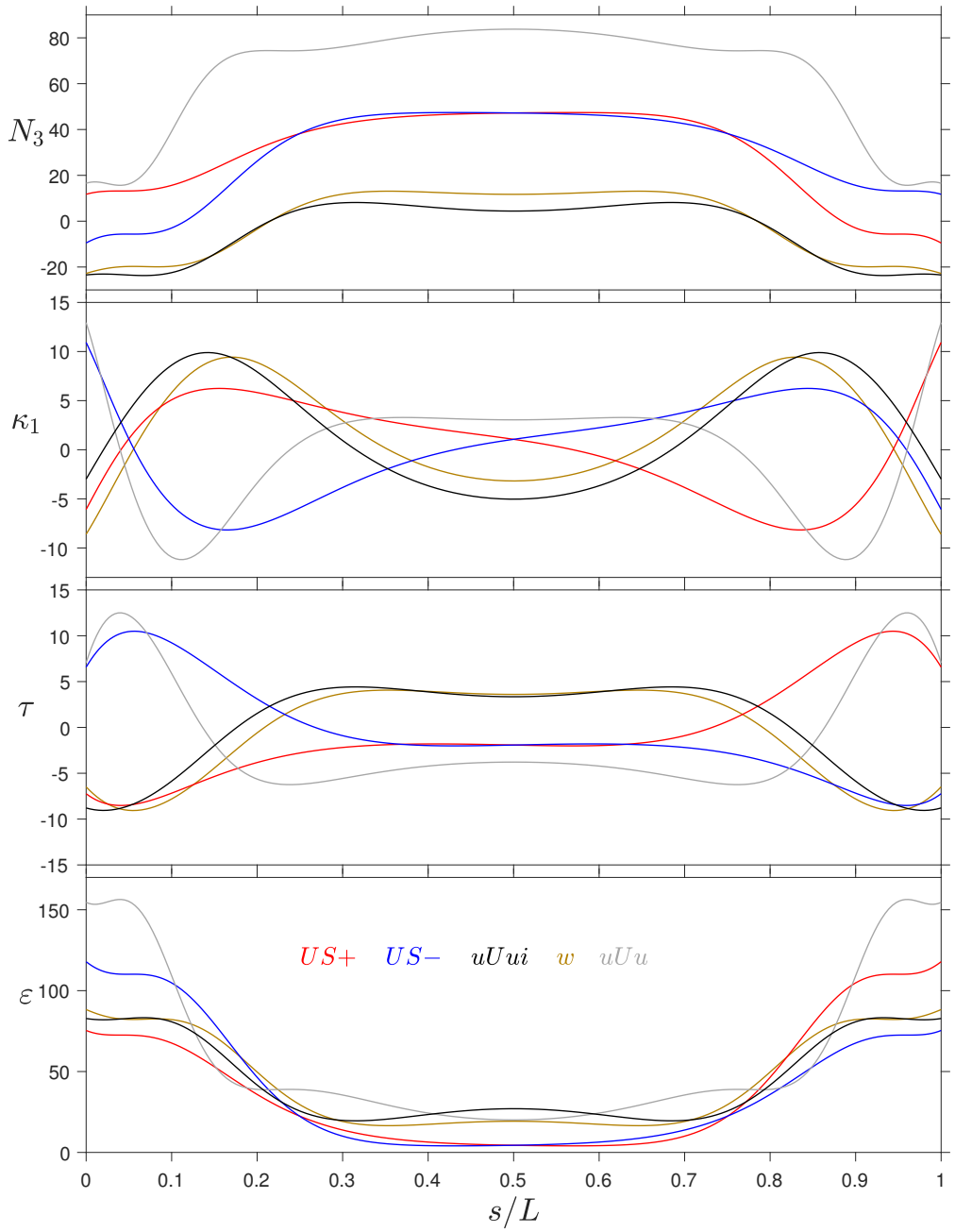

Figure 2.11: For five stable configurations at $\psi_0 = 30°$, $\Delta L/L = 1/2$, and $\Delta D/L = 0.625$, we plot the axial force N_3, the curvature κ_1, the twist τ, and the energy density $\varepsilon = \frac{1+\nu}{2}\kappa_1^2 + \tau^2$, with $\nu = 0.25$. The $uUui$, w and uUu states are reversibly symmetric about their midpoint, while the $US\pm$ states are a reversibly symmetric pair. Increasing s/L corresponds to moving from right to left on any curve renderings in the text.

it will eventually link up with one of the black curves at higher angles. The experiments

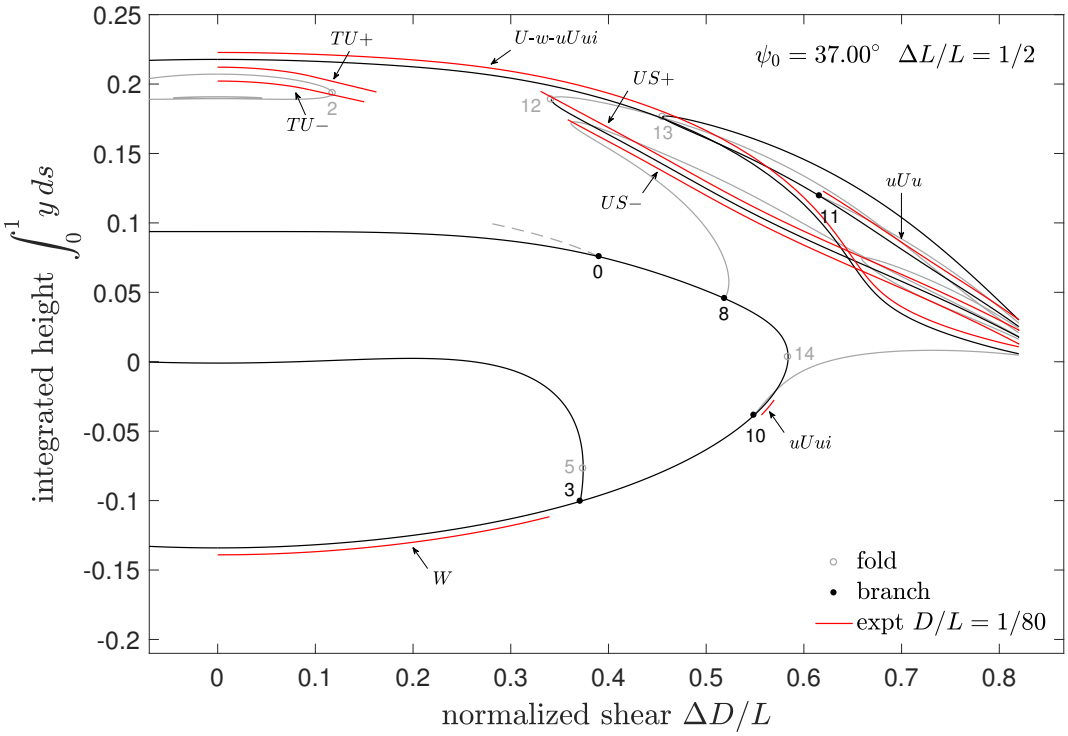

Figure 2.12: Some solutions (black and grey curves) and bifurcations (open and closed disks, some numbered) of the perfectly anisotropic Kirchhoff rod equations for clamping angle $\psi_0 = 37°$, along with experimental data (red curves). Some of the grey curves from prior diagrams have been removed. The horizontal extent of the red curves is the range of stability (typical variation $\approx \pm 0.01\,\Delta D/L$), while the vertical position of the curves is not measured data, but is made to follow near the numerical curves whenever a comparison is possible. No data was taken for $\Delta D/L < 0$. Numerically, the *U-w* branch has collided with the *uUui* branch, creating a *U-w-uUui* branch and a small residual *uUui* branch. These are also observed experimentally. There is now a continuous *U-w-uUui* path from first mode planar *elastica* to approach the limiting shear. The $WS\pm$ states are close to disappearing numerically, and are not observed experimentally.

confirm the changes in connectivity, including the presence of a residual *uUui* branch with short extent at intermediate shear. Interestingly, this *uUui* shape continues to jump to the *U-w-uUui* branch upon increasing shear, and to the *US−* branch upon decreasing shear, even as the range of stability shrinks and these bifurcations (fold and subcritical pitchfork) approach the same value of shear. This, along with the relatively steep slope of the branch, imply that the shapes change significantly over a narrow range of shear. Many transitions are illustrated in the supplementary video `transition37.mp4` [2].

Figure 2.13 shows some solution manifolds and experimental stability data for a clamping angle $\psi_0 = 45°$, after a collision between pitchfork 3 and fold 5 at $\psi_0 \approx 41.74°$ has made $WS\pm$ states unstable, and a collision-annihilation of branch points 8 and 10 at $\psi_0 \approx 44.27°$ has

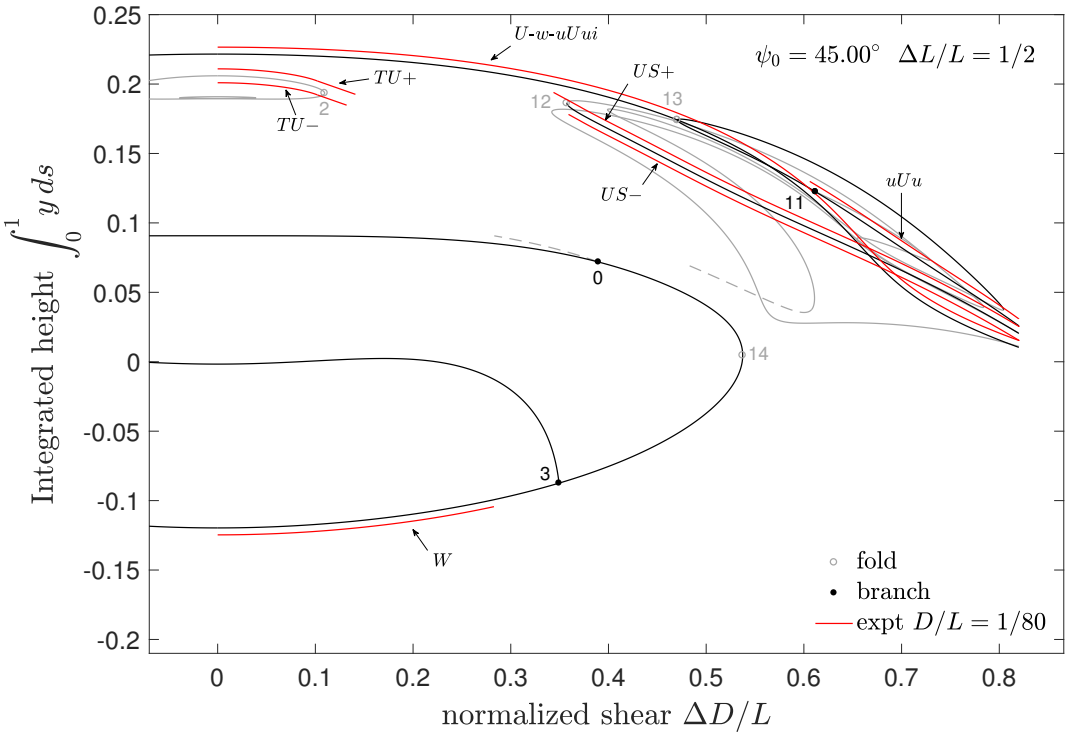

Figure 2.13: Some solutions (black and grey curves) and bifurcations (open and closed disks, some numbered) of the perfectly anisotropic Kirchhoff rod equations for clamping angle $\psi_0 = 45°$, along with experimental data (red curves). One grey curve has been truncated with a dashed line. The horizontal extent of the red curves is the range of stability (typical variation $\approx \pm 0.01\,\Delta D/L$), while the vertical position of the curves is not measured data, but is made to follow near the numerical curves whenever a comparison is possible. No data was taken for $\Delta D/L < 0$. The $WS\pm$ states have become unstable, and the residual $uUui$ branch has disappeared.

eliminated the residual $uUui$ branch. Details of the latter process are shown in Figure 2.14. Some complicated changes in connectivity of unstable (unobserved) states have occurred near the limiting shear, and one curve has turned back to link up with states we have already removed; we use a dashed line to truncate this curve. This connection is actually short-lived and will soon be lost again, so this dashed line will not appear again in subsequent figures.

Figure 2.15 shows some solution manifolds and experimental stability data for a clamping angle $\psi_0 = 55°$. At $\psi_0 \approx 52.09°$, a pair of subcritical pitchforks is born on the uUu branch at $\Delta D/L \approx 0.789$. By $\psi_0 = 55°$, one pitchfork 15 remains, the other has exited to the right at high shear, while a fold 16 has entered from the right. The details of this process are not known, but from the loci shown later in Figure 2.18, it seems that there is a curve splitting at high shear that we don't observe. Other curves have also developed folds that move in from the limiting shear, and additional complicated changes in connectivity of unstable (unobserved) states have occurred. At this angle, the $US\pm$ branch turns around

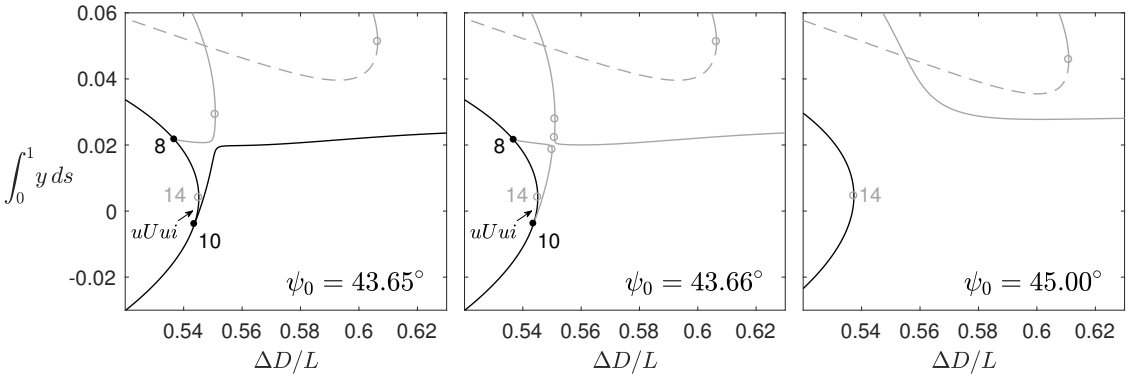

Figure 2.14: Details of several transitions that change the connectivity of solution curves. The annihilation of branch points 8 and 10 occurs at fold point 14 and leads to the disappearance of the residual $uUui$ branch. Closed and open disks are branch and turning points, respectively.

at $\Delta D/L \approx 0.856$ and connects to the loopy grey curves. We experimentally observe that both $US\pm$ states lose stability before this value of shear, although for the $US+$ state this is at a value of shear higher than what we show in the figures. Bifurcation 3 should now take the W state to the U-w-$uUui$ branch instead of the $US\pm$ branch. This change in path actually begins to happen at lower angles due to the destabilizing effects of gravity on the W state, as can be seen in Figure 2.13. Therefore, starting with any planar state at this high clamping angle and simply applying shear, we will approach the limit through a U-like state, and not an S-like state. Experimental results on the short uUu branch are inconsistent, in that sometimes the state is not observed. The data shown are for "correct" observations. The system is sensitive due to its proximity to an event at $\psi_0 \approx 56.29°$, when subcritical pitchforks 11 and 15 annihilate each other, leading to the disappearance of the uUu state.

Figure 2.16 shows some solution manifolds and experimental stability data for a clamping angle $\psi_0 = 60°$. The terminal fold 17 of the $US\pm$ branch now appears at a lower shear, $\Delta D/L \approx 0.771$. Experiments are qualitatively consistent with the solutions, with gravity significantly destabilizing the W state at this high angle and asymmetrizing the $US\pm$ transitions with respect to fold 17.

Transitions at $\psi_0 = 55°$ and $\psi_0 = 60°$ are shown in the supplementary video `transition5560.mp4` [2]. It can be seen that the $US+$ to U-w-$uUui$ transition through fold 17 at $\psi_0 = 60°$ involves a rapid rotation of one end. A similar rapid rotation is seen during local snap-through events in the tensile loading of slit sheets [51]. This transition is explored further in Figure 2.17, which plots the bending energy density $\varepsilon = \frac{1+\nu}{2}\kappa_1^2$, with $\nu = 0.25$, the twist energy density τ^2, and the total energy density for the states just before and after this transition. It can be seen that the jump relieves a high concentration of bending energy at one end and partially relieves some twisting energy near that end while shifting its maximum to the end, and partially relieves some twisting energy at the other end. Some of the energy has moved into

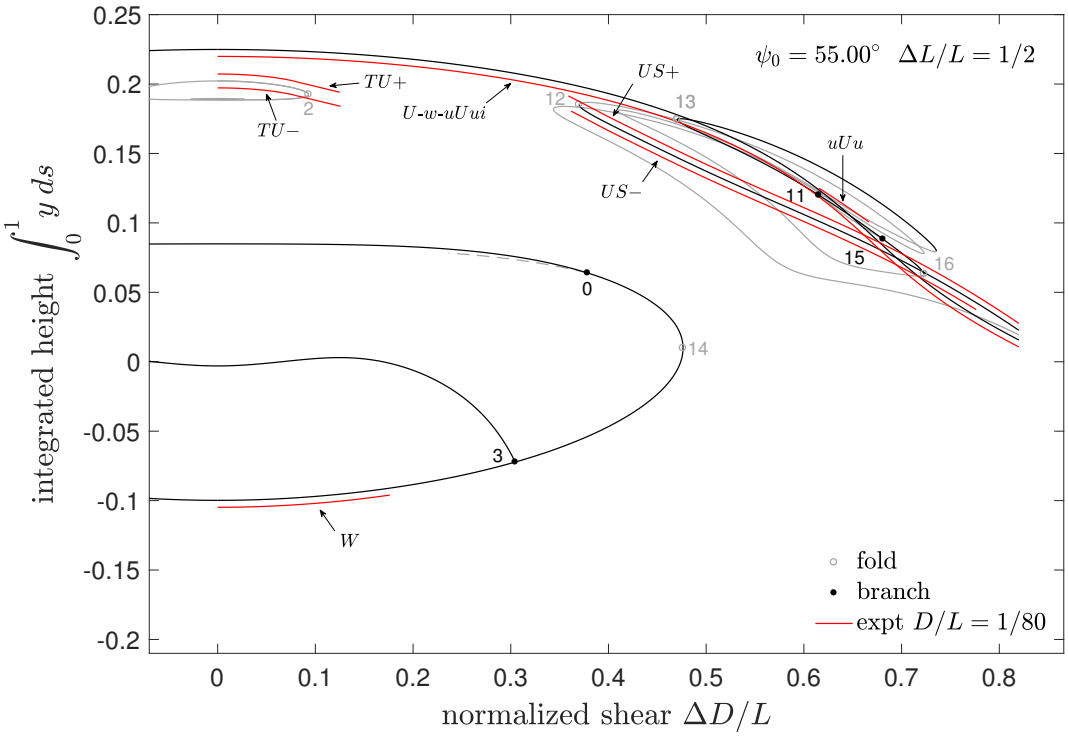

Figure 2.15: Some solutions (black and grey curves) and bifurcations (open and closed disks, some numbered) of the perfectly anisotropic Kirchhoff rod equations for clamping angle $\psi_0 = 55°$, along with experimental data (red curves). The horizontal extent of the red curves is the range of stability (typical variation $\approx \pm 0.01\,\Delta D/L$), while the vertical position of the curves is not measured data, but is made to follow near the numerical curves whenever a comparison is possible. No data was taken for $\Delta D/L < 0$. Several changes have occurred and are described in the text. The $US\pm$ branch has a fold at higher shear than what we show here, and connects back to the loopy grey curves. The uUu branch is not always observed experimentally.

the central expanse of the rod, but this region stores relatively little elastic energy either before or after the transition, most of it in twist.

If we continue to increase the clamping angle above $\psi_0 = 60°$, the twisted $TU\pm$ loops will shrink and disappear through the annihilation of two folds at $\psi_0 \approx 74.03°$. The loopy structure of $US\pm$ also shrinks and disappears after undergoing some complicated transitions which we do not investigate here. Additionally, the subcritical pitchfork 3 delimiting the stability of the W state approaches the zero-shear axis and annihilates with its negative-shear twin to eliminate the stable W state at $\psi_0 \approx 76.95°$— this is the classic snap-through of an inverted *elastica* arch under end rotations [37]. After this, the only remaining stable configuration is U-w-$uUui$. We did not proceed past clamping angles of $\psi_0 = 80°$.

To conclude this section, we remark that, despite some variable results due to sensitivity of

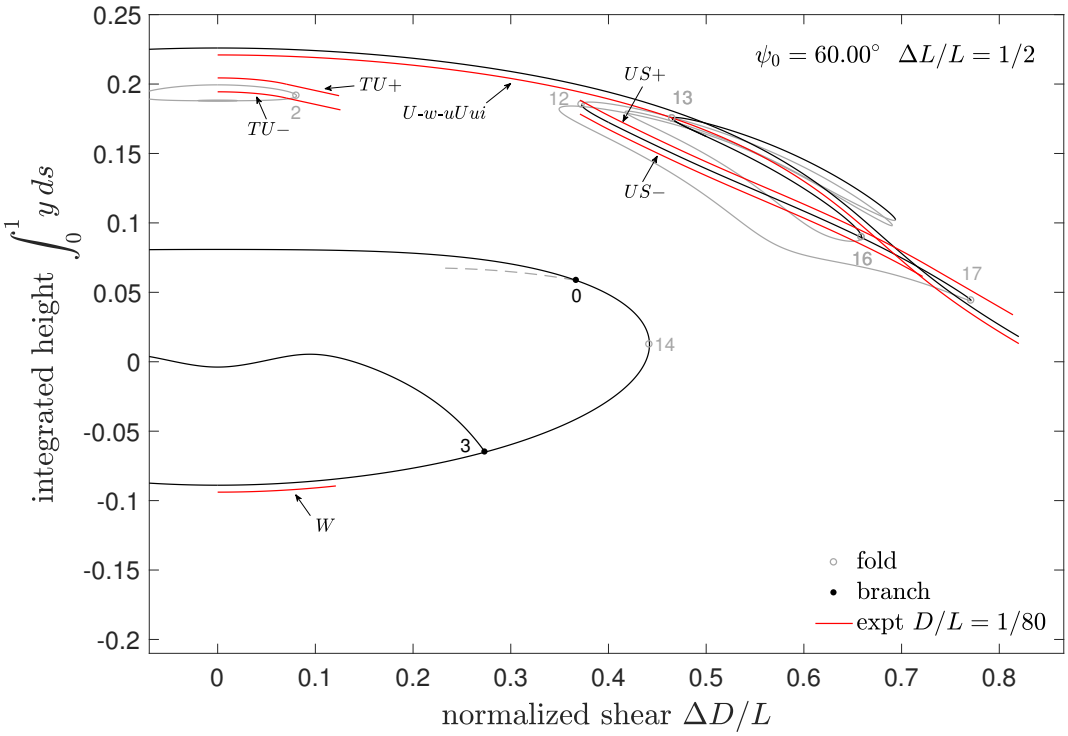

Figure 2.16: Some solutions (black and grey curves) and bifurcations (open and closed disks, some numbered) of the perfectly anisotropic Kirchhoff rod equations for clamping angle $\psi_0 = 60°$, along with experimental data (red curves). The horizontal extent of the red curves is the range of stability (typical variation $\approx \pm 0.01\,\Delta D/L$), while the vertical position of the curves is not measured data, but is made to follow near the numerical curves whenever a comparison is possible. No data was taken for $\Delta D/L < 0$. The uUu branch has disappeared, and the fold 17 on the $US\pm$ branch appears at a lower shear. Experimentally, the W state is significantly destabilized by gravity.

the system near bifurcations, all of our experimental observations for narrow bands seem to be explained by the anisotropic Kirchhoff model, with allowance for the effects of gravity.

2.5 Loci of bifurcations related to stable states

The complicated landscape of connectivity changes surveyed in the previous section can be better understood by tracing the loci of bifurcation points of the perfectly anisotropic Kirchhoff equations in a higher-dimensional parameter space. For our present study at fixed compression $\Delta L/L = 1/2$, this is the two-dimensional space spanned by normalized shear $\Delta D/L$ and clamping angle ψ_0. Figure 2.18 shows the paths traced in this space by many fold and branch points, numbered as on figures in Section 2.4. Most of these are connected in some way with states observed in experiments, and thus delineate regions of stability for

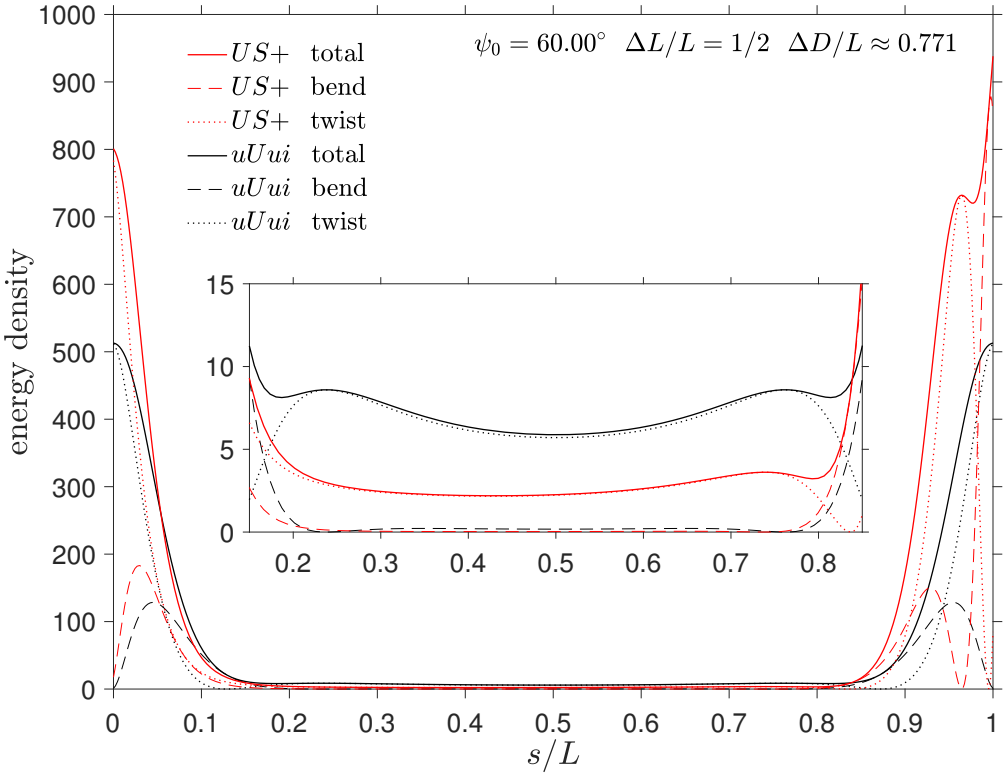

Figure 2.17: The bending energy density $\varepsilon = \frac{1+\nu}{2}\kappa_1^2$ with $\nu = 0.25$, the twist energy density τ^2, and the total energy density for the two states before and after the $US+$ to $uUui$ transition, the latter being the high shear portion of the U-w-$uUui$ branch. The jump relieves a high concentration of bending energy at the $s = 1$ end of the $US+$ state. The central expanse of the rod, shown in the inset, stores relatively little elastic energy, most of it in twist. Increasing s/L corresponds to moving from right to left on any curve renderings in the text.

various configurations. The leftmost inset shows the cusp that gives rise to folds 6 and 7 and the w state at the small value of clamping angle $\psi_0 \approx 0.135°$. The middle inset corresponds to the complicated series of transitions shown in Figure 2.9. The upper right inset corresponds to the merge-split event between the w and $uUui$ branches at $\psi_0 \approx 30.62°$. The turning points connecting pitchfork 4 and branch point 9, and pitchforks 11 and 15, represent the annihilation events between these two pairs of bifurcations at $\psi_0 \approx 28.15°$ (Figure 2.9) and $\psi_0 \approx 56.29°$, respectively. Continuing along the 15 curve, there is another turning point at higher shear, which implies that 15 and another pitchfork appear together on the uUu branch at $\psi_0 \approx 52.09°$, with the other moving off to higher shears, as discussed earlier with respect to Figure 2.15. Between folds 12 and 17, there are two turning points and a cusp, indicating some complicated behavior involved in the disappearance of the $US\pm$ states at clamping angles above 70°. The diagram is symmetric about zero shear; note the asymmetry between folds 1 and 2 that govern the disappearance of twisted states, such that 1 has a cusp on the zero-shear line, while 2 has a smooth turning point. The diagram also has a

symmetry about zero clamping angle, but in a pairwise sense; for example, curves 1 and 2 will exchange their identities upon crossing this axis.

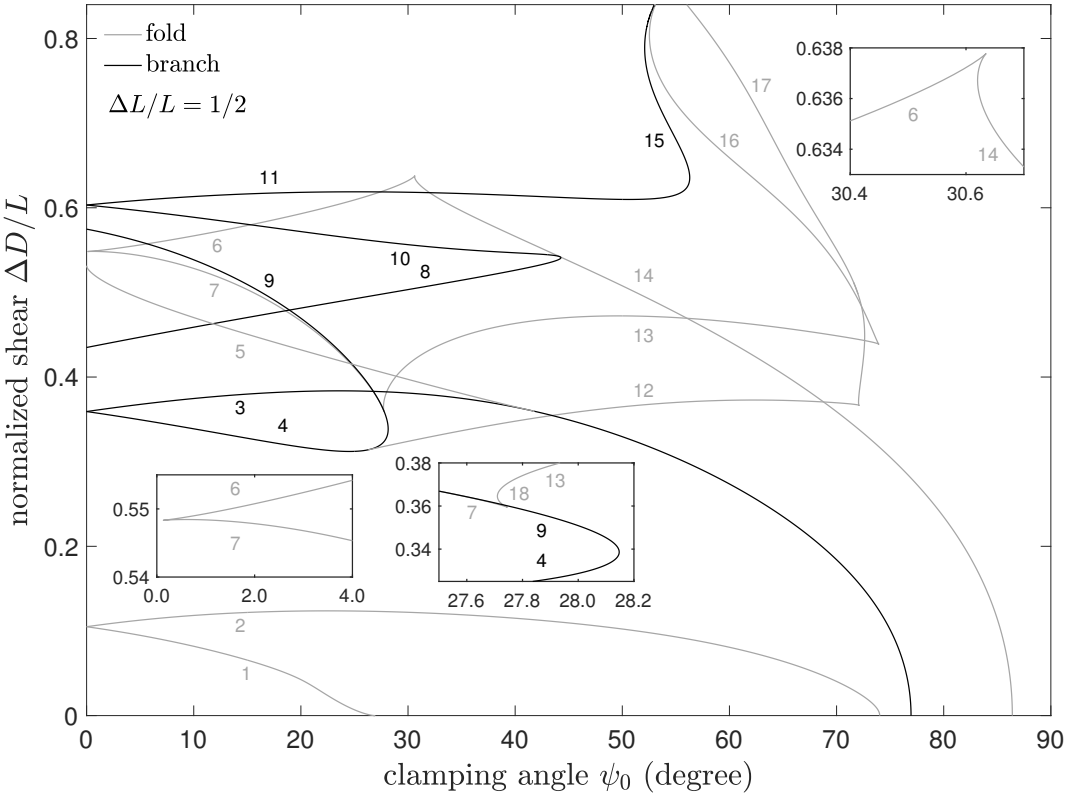

Figure 2.18: Loci of various bifurcations for the perfectly anisotropic Kirchhoff rod in the plane spanned by clamping angle ψ_0 and shear $\Delta D/L$, at fixed compression $\Delta L/L = 1/2$. Numbers correspond to those on figures in Section 2.4.

The loci provide some information about regions of stability. For example, with reference to the positive shear and clamping angle quadrant shown here, the $TU\pm$ and $TW\pm$ states are stable below curves 2 and 1, respectively, and the W state is stable below curve 3. The $WS\pm$ states are stable in the region between curves 3 and 5. The $US\pm$ states are stable above and to the left of a curve connecting the loci of 4, 12, and 17.

It is clear that clamping at large angles reduces the number of available states, and thus the occurrence of jump events. We can use a diagram like Figure 2.18 to avoid such violent events. For example, we might wish to transform a large clamping angle, large shear $US+$ state to a large clamping angle, small shear U state, without experiencing the jump that would occur upon simply reducing the shear. Instead, we can decrease the clamping angle, decrease the shear, and increase the clamping angle again. Thus we avoid crossing line 12, corresponding to a fold-induced jump, and instead cross line 4, corresponding to a supercritical pitchfork. For another example, we can transform a small clamping angle, large shear w state to either a small clamping angle, small shear U state or a small clamping angle, large(r) shear $uUui$ state

by first increasing the clamping angle, then shearing back or forward, and finally decreasing the clamping angle again. This avoids crossing lines 7 or 6, which are fold-induced jumps, and makes use of the continuous *U-w-uUui* branch available at large clamping angles.

2.6 Width effects: from rods to ribbons to plates

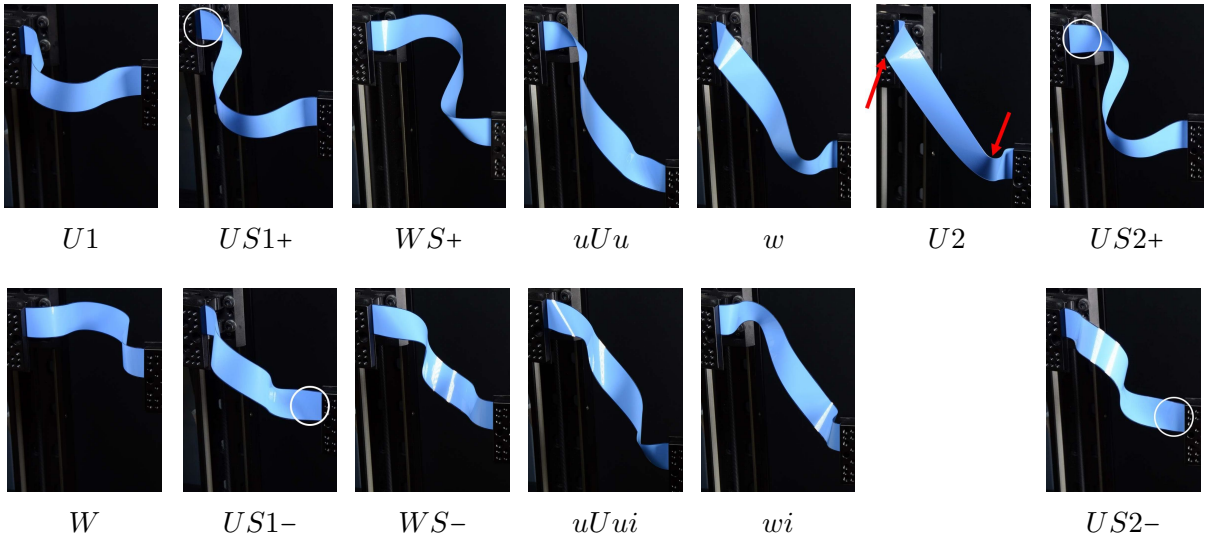

Figure 2.19: Some experimental configurations observed in wide bands, with aspect ratio $D/L = 1/8$, compression $\Delta L/L = 1/2$, clamping angle $\psi_0 = 5°$, and various values of shear $\Delta D/L$. Twisted states are not shown. Gravity is roughly vertical in these images. The $US1\pm$ and $US2\pm$ states are separated by weak local jumps in the circled regions. At very low clamping angles, there is a similar separation of $WS\pm$ into $WS1\pm$ and $WS2\pm$ states, but these have already merged at this clamping angle. The $U1$ and $U2$ states will become connected at higher clamping angles. The red arrows on the $U2$ state point at regions of focused curvature.

In this section, we present experimental results on wide bands ($D/L = 1/8, 1/4$) and compare them with the narrow band ($D/L = 1/80$) experiments and the anisotropic Kirchhoff rod model for a couple of choices of clamping angle ($\psi_0 = 0°, 15°$) at the same compression $\Delta L/L = 1/2$. The effects of gravity become less important as the width of the band increases. The behavior of twisted states for intermediate width bands is quite complicated, including the appearance of new stable states and self-contact. Reserving a deeper exploration for future study, we leave this behavior out of the present discussion, other than to present later a few examples of twisted states for various intermediate width bands in Figure 2.22. Also shown there are indented states, which become possible for very wide bands, and are another topic we reserve for future study. For the wider $D/L = 1/4$ bands, no twisted states are observed. Aside from twisted states, several new states appear in wide bands, but these

still appear to be related to the states we have already seen for narrow bands, and we can attempt to organize all the results around the Kirchhoff solutions. The reversible symmetry properties of the Kirchhoff equations appear to persist in all of the experimentally observed wide band states.

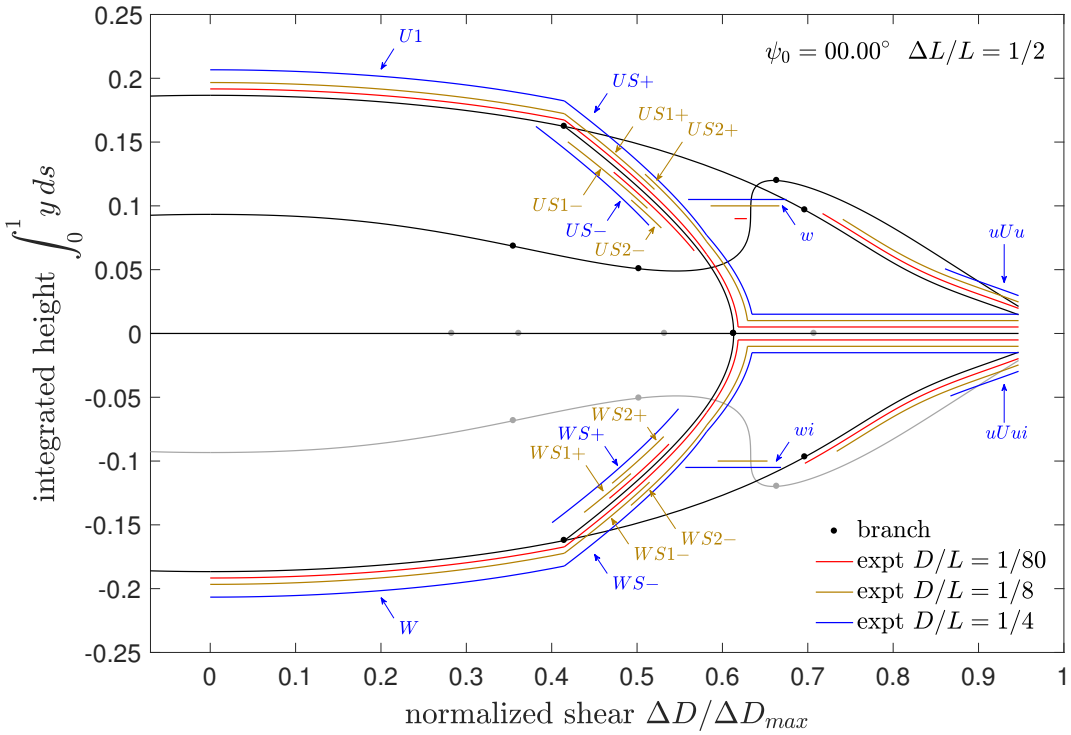

Figure 2.20: Experimental data (red, brown, and blue curves) from narrow and wide bands, normalized by limiting shear, for clamping angle $\psi_0 = 0°$, compared with numerical solutions of the anisotropic rod equations (black and grey curves). Twisted states are not included. The horizontal extent of the experimental curves is the range of stability (estimated error $\approx \pm 0.01\,\Delta D/L$), while the vertical position of the curves is not measured data, but is made to follow near the numerical curves whenever a comparison is possible. No data was taken for $\Delta D/L < 0$. The $US\pm$ states are split into two states for the intermediate-width bands. For the widest bands, the pitchforks between $U1$ and $US\pm$ and W and $WS\pm$ are only weakly broken by gravity, and transitions to either of the $\pm$ pair are observed.

Figure 2.19 shows some of the states we observe in wide bands for a band of aspect ratio $D/L = 1/8$, a shallow clamping angle $\psi_0 = 5°$, and various values of shear $\Delta D/L$. We name the states with reference to those found in narrow bands. The U state is now called $U1$, as there is a $U2$ branch stabilized at higher shears; the two will eventually connect at higher clamping angles. Increasing the shear in the $U2$ state leads to focusing of generators and bending energy, as indicated by the two red arrows. The intermediate width bands ($D/L = 1/8$) now feature two sets of $US\pm$ states, which are separated by weak local jumps in the circled regions. At very low clamping angles, there is a similar separation of $WS\pm$

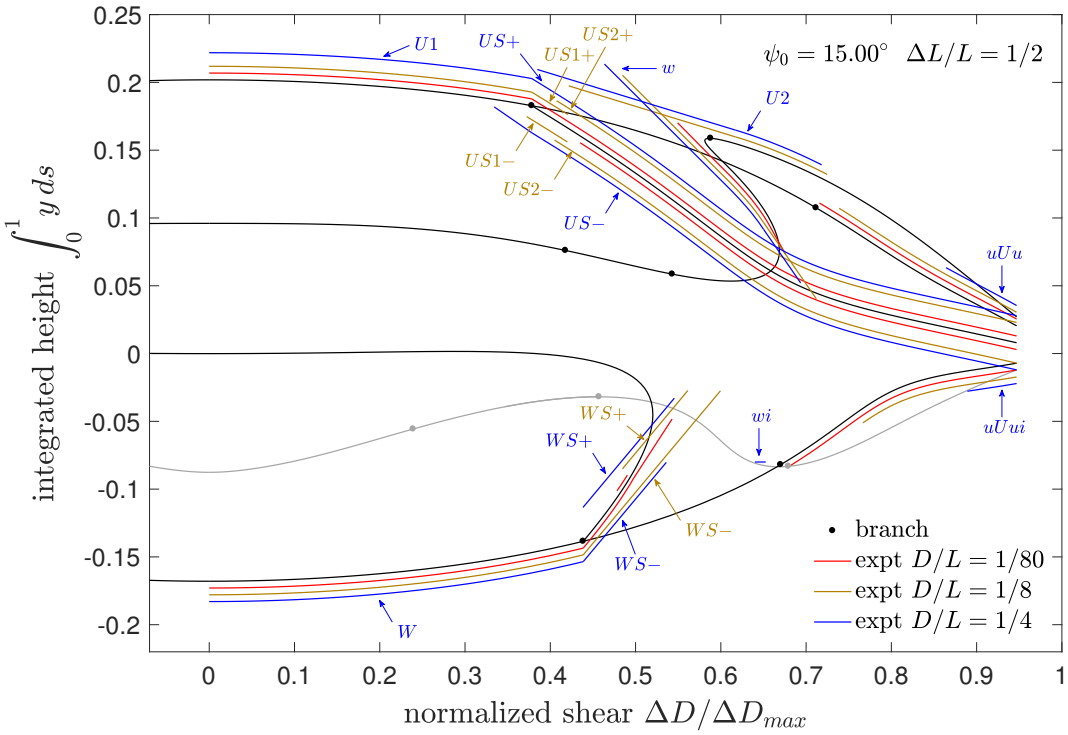

Figure 2.21: As in Figure 2.20, but with clamping angle $\psi_0 = 15°$. The $U2$ state first appears at small nonzero clamping angles. For the widest bands, the pitchforks between $U1$ and $US\pm$ and W and $WS\pm$ are only weakly broken by gravity, and transitions to either of the $\pm$ pair are observed.

into $WS1\pm$ and $WS2\pm$ states, but these have already merged with each other into a single $WS\pm$ set at this small clamping angle. Twisted states are also present, but not shown in this figure. The inverted version of the w state, the wi state, is observed in wide bands.

To compare bands of different width, we now normalize the shear ΔD using the limiting shear for a band of given width, as discussed in Appendix A.1. We have $\Delta D_{max} \approx 207.85$ mm for $D/L = 1/80$, $\Delta D_{max} = 180.00$ mm for $D/L = 1/8$ and $\Delta D_{max} \approx 156.33$ mm for $D/L = 1/4$. Figures 2.20 and 2.21 show some solution manifolds for the perfectly anisotropic Kirchhoff rod, along with experimental data for narrow and wide bands for clamping angles $\psi_0 = 0°$ and $\psi_0 = 15°$, respectively. Twisted states are not included. While the $U2$ state is not present at zero clamping angle, it begins to exist at small nonzero clamping angles, and can be seen in Figure 2.21. Based on its shape, it seems to correspond to a state observed in the Kirchhoff solutions but which is experimentally unstable for narrow bands. For wide bands, the w state can be reached by gently poking the stable $U2$ state so that it buckles inwards near its midpoint. At both clamping angles, it is clear that increasing the width of the band stabilizes the w and wi states and destabilizes the uUu and $uUui$ states. Recall that the w state does not appear for the Kirchhoff solutions until a small nonzero clamping angle. The states all seem to follow the Kirchhoff rod backbone, but there is clearly an additional

jump (probably two folds?) separating the $US1\pm$ and $US2\pm$ states, and another separating the $WS1\pm$ and $WS2\pm$ states, for intermediate width bands ($D/L = 1/8$) at sufficiently low clamping angles. This effect is shown in the supplementary video `widtheffect15.mp4` [2]. For the widest bands ($D/L = 1/4$), the pitchforks between $U1$ and $US\pm$ and W and $WS\pm$ are only weakly broken by gravity, and transitions to either of the $\pm$ pair are observed, in contrast to the consistently biased choices made by narrow bands.

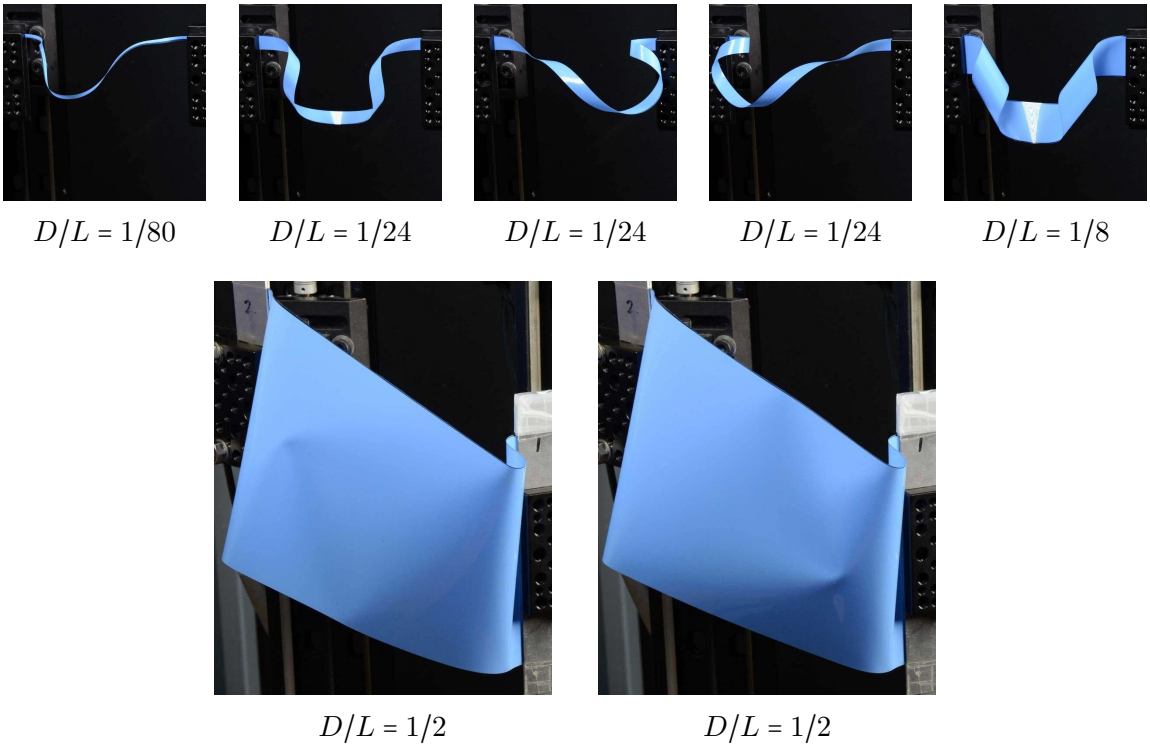

$D/L = 1/80$ $D/L = 1/24$ $D/L = 1/24$ $D/L = 1/24$ $D/L = 1/8$

$D/L = 1/2$ $D/L = 1/2$

Figure 2.22: Examples of states stabilized by width effects. Twisted states, different from the narrow band state shown in the upper left, are stabilized and then destabilized or eliminated by self-contact issues by increasing width. Each twisted state shown is a $-$ state, and there exist corresponding $+$ states. A pair of indented states exist for very wide bands; the elastic defects are stable only for a very narrow range of shear. All bands are compressed to $\Delta L/L = 1/2$; the bands with $1/80 \leq D/L \leq 1/8$ are clamped at $\psi_0 = 0°$ and the very wide band with $D/L = 1/2$ is clamped at $\psi_0 = 30°$.

At slightly higher clamping angles, the $U1$ and $U2$ states become connected for wider bands. This is in contrast to the Kirchhoff solutions and narrow band data, for which the $U1$ state (called U in the prior Section 2.4) merges with the w state. At higher clamping angles, shearing the $U1$-$U2$ state will lead to two successive snap-throughs to the w and $uUui$ states. These transitions are shown in the supplementary video `widtheffect45.mp4` [2], where it can be clearly seen that the violence of the first snap-through increases with increasing width. In general, greater width exaggerates the effect of energy focusing of the generators of a developable strip [52, 53, 54]; the snap-through transitions release some of this stored

bending energy. The limiting shear is approached *via* one of four possible limiting states, either the S-like $US\pm$ pair or the U-like uUu and $uUui$ states. These contain highly focused conical singularities near their ends, as shown in Appendix A.1.

No other new states were observed in experiments at $\psi_0 = 30°$, $45°$, or $60°$, although interesting changes in connectivity do occur, one of which is shown in the supplementary video `widtheffect45.mp4` [2].

We briefly mention some other states that are stabilized by width effects, some of which are shown in Figure 2.22. At a width $D/L = 1/24$, the narrow band $D/L = 1/80$ twisted state pair is replaced by three other $\pm$ pairs. These states are sensitive to boundary conditions; one can play by hand with a band of $D/L = 1/40$ and see all eight twisted states by changing compression and clamping angle. Depending on the state, application of shear may lead to a snap-through, a looped structure, or self-contact. At a width of $D/L = 1/8$, the intermediate-width $\pm$ pair has become unstable, and at higher widths the symmetric intermediate-width state requires self-contact. For very fat bands, such as the $D/L = 1/2$ bands shown in in the figure, there is a pair of stably indented states, each of which contains a pair of "d-cones". These elastic defects are only stable for a very narrow range of applied shear, and upon decreasing or increasing shear will respectively annihilate or propagate through the structure to emerge through the boundaries, enabling a snap-through transition. Both the twisted and indented examples suggest rich avenues of research, which we reserve for future work.

2.7 Further discussion

We have presented experimental results on the stability of thin elastic bands subject to compression, shear, and symmetric clamping. The Kirchhoff equations for perfectly anisotropic rods serve as a surprisingly good guide to the behavior of these bands, particularly when they are narrow in width. We have explored only a limited region of the parameter space of boundary conditions and band geometry, but have already stumbled on many new stable configurations and jump phenomena. Here we briefly discuss some confusing issues and avenues for future work.

First we note again that there is a distinct difference between a Kirchhoff rod, whose cross section remains orthogonal to its centerline, and a developable strip. This difference is quite obvious in an image like Figure 2.1b, where the director $\boldsymbol{d_1}$ associated with the slice of material perpendicular to the rod centerline is clearly not aligned with a straight line (generator) on the strip. This "rod"'s cross section is actually bending in the width direction. This is why our renderings of the Kirchhoff solutions as strips representing the rod frame are not equivalent to renderings of isometrically deforming elastic strips. This point is reiterated in Appendix A.2. However, the assumption of developability is itself problematic, particularly when applied to narrow strips. We refer the reader to Appendix A.5 for a

demonstration of the limitations of strip models in the present context.

From the behavior of wider bands, we might have expected that branch point 9 in the Kirchhoff solutions would be a pitchfork bifurcation with a stable $U2$-like state on one side. We do not observe any such stable state for narrow bands. For wider bands, the $U2$ state is somewhat shell-like, with synclastic curvature, and one can pop back and forth between $U2$ and the slightly indented w state. In contrast, width appears to destabilize the highly bent and twisted uUu and $uUui$ states. The stability of twisted states at low shear also shows a complicated dependence on width. These and more complicated stabilization effects, such as the narrow range of boundary conditions allowing one to create defects by indenting very wide plate-like bands such as those shown in Figure 2.22, raise interesting questions about the boundaries between rod-like, plate-like, and shell-like behavior in thin sheets. In order to capture such width effects, one needs either a model of a two-dimensional plate or strip, or a Cosserat rod model with a more complicated structure derived from such a two-dimensional model [55, 56, 57]. In some such models, the width of the band can appear as a potential continuation parameter. However, strip models lead to difficulties in numerical implementation because of the singular way in which they handle inflection points, which must be added by hand and cannot arise spontaneously during continuation. These models will not admit rod-like solutions such as those shown in Figures 2.11 and 2.17, where the twist, which for strips is identified with the torsion, does not vanish simultaneously with the curvature. More importantly, without some further modification, such models cannot be used to continue solutions such as those of the U-w-$uUui$ branch, in which inflection points smoothly appear during deformation.

The full space of boundary conditions includes positions and general tilts in all directions, such that the director frames at the end points may take arbitrary values in the space of rotations SO(3). In addition to energy barriers leading to multi-stability and jump phenomena, the non-simply-connected nature of SO(3) can also create topological barriers to deformation. This fact– related to the famous "belt trick" of Dirac– implies a lower bound on elastic energy for rods subject to boundary conditions in which the end tangents are parallel [1]. It would be of great interest to expand these results to arbitrary boundary conditions, which would require some consideration of how to define an appropriate linking number for open rods [20, 58, 59, 60].

Our elastic system has an analogue in the geometric controls literature, in which the orientation of the frame of our perfectly anisotropic rod appears as the orientation of a vehicle that can pitch and roll, but cannot yaw, and the elastic energy appears as a quadratic cost function for the two allowed controls [61]. However, without constraints on path length in the controls problem, the analogy is only strictly correct for an elastic setup in which the rod is not clamped, but is allowed to vary its length by sliding in or out of sleeves. The ability to satisfy boundary conditions that favor a forbidden bending or steering rotation through an indirect combination of other allowed rotations reflects the fact that the commutator of two infinitesimal rotations in $\mathbb{E}^3$ provides the third.

Acknowledgments

We thank G H M van der Heijden for helpful discussions, particularly regarding the treatment of singularities in Appendix A.5. We also thank M A Dias and T J Healey for helpful comments, and P S Krishnaprasad for the reference [61].

Bibliography

[1] J. C. Baez and R. Dandoloff. Topological lower bound on the energy of a twisted rod. *Physics Letters A*, 155(2-3):145–147, 1991.

[2] Six supplementary videos are available at: http://www.sciencedirect.com/science/article/pii/S0022509617307469.

[3] M. Arya, N. Lee, and S. Pellegrino. Wrapping thick membranes with slipping folds. In *2nd AIAA Spacecraft Structures Conference, AIAA SciTech Forum, (AIAA 2015-0682)*, 2015.

[4] Such toys are known under various names, including princess wands and spinsations. For videos, see http://www.hippie-sticks.com/.

[5] L. L. Howell. *Compliant Mechanisms*. John Wiley & Sons, 2001.

[6] P. Mandal and C. R. Calladine. Lateral-torsional buckling of beams and the Southwell plot. *International Journal of Mechanical Sciences*, 44(12):2557–2571, 2002.

[7] S. S. Antman and C. S. Kenney. Large buckled states of nonlinearly elastic rods under torsion, thrust, and gravity. *Archive for Rational Mechanics and Analysis*, 76(4):289–338, 1981.

[8] S. S. Antman and K. B. Jordan. Qualitative aspects of the spatial deformation of non-linearly elastic rods. *Proceedings of the Royal Society of Edinburgh*, 73A:85–105, 1974/75.

[9] S. Kehrbaum and J. H. Maddocks. Elastic rods, rigid bodies, quaternions and the last quadrature. *Philosophical Transactions of the Royal Society of London A*, 355: 2117–2136, 1997.

[10] M. Nizette and A. Goriely. Towards a classification of Euler-Kirchhoff filaments. *Journal of Mathematical Physics*, 40(6):2830–2866, 1999.

[11] O. Ameline, S. Haliyo, X. X. Huang, and J. A. H. Cognet. Classifications of ideal 3D elastica shapes at equilibrium. *Journal of Mathematical Physics*, 58:062902, 2017.

[12] S. Neukirch and M. E. Henderson. Classification of the spatial equilibria of the clamped elastica: Symmetries and zoology of solutions. *Journal of Elasticity*, 68(1-3):95–121, 2002.

[13] M. E. Henderson and S. Neukirch. Classification of the spatial equilibria of the clamped elastica: Numerical continuation of the solution set. *International Journal of Bifurcation and Chaos*, 14(04):1223–1239, 2004.

[14] J. Coyne. Analysis of the formation and elimination of loops in twisted cable. *IEEE Journal of Oceanic Engineering*, 15(2):72–83, 1990.

[15] T. Yabuta, N. Yoshizawa, and N. Kojima. Cable kink analysis: cable loop stability under tension. *Journal of Applied Mechanics*, 49:584–588, 1982.

[16] Y. Miyazaki and K. Kondo. Analytical solution of spatial elastica and its application to kinking problem. *International Journal of Solids and Structures*, 34(27):3619–3636, 1997.

[17] V. G. A. Goss, G. H. M. van der Heijden, J. M. T. Thompson, and S. Neukirch. Experiments on snap buckling, hysteresis and loop formation in twisted rods. *Experimental Mechanics*, 45(2):101–111, 2005.

[18] G. H. M. van der Heijden, S. Neukirch, V. G. A. Goss, and J. M. T. Thompson. Instability and self-contact phenomena in the writhing of clamped rods. *International Journal of Mechanical Sciences*, 45(1):161–196, 2003.

[19] J. M. T. Thompson and A. R. Champneys. From helix to localized writhing in the torsional post-buckling of elastic rods. *Proceedings of the Royal Society A*, 452(1944): 117–138, 1996.

[20] G. H. M. Van der Heijden and J. M. T. Thompson. Helical and localised buckling in twisted rods: A unified analysis of the symmetric case. *Nonlinear Dynamics*, 21(1): 71–99, 2000.

[21] S. Goyal, N. C. Perkins, and C. L. Lee. Nonlinear dynamics and loop formation in Kirchhoff rods with implications to the mechanics of DNA and cables. *Journal of Computational Physics*, 209:371–389, 2005.

[22] B. D. Coleman, I. Tobias, and D. Swigon. Theory of the influence of end conditions on self-contact in DNA loops. *Journal of Chemical Physics*, 103(20):9101–9109, 1995.

[23] A. Mielke and P. Holmes. Spatially complex equilibria of buckled rods. *Archive for Rational Mechanics and Analysis*, 101(4):319–348, 1988.

[24] A. R. Champneys and J. M. T. Thompson. A multiplicity of localized buckling modes for twisted rod equations. *Proceedings of the Royal Society A*, 452(1954):2467–2491, 1996.

[25] G. H. M. van der Heijden and J. M. T. Thompson. Lock-on to tape-like behaviour in the torsional buckling of anisotropic rods. *Physica D*, 112(1-2):201–224, 1998.

[26] P. B. Béda, A. Steindl, and H. Troger. Postbuckling of a twisted prismatic rod under terminal thrust. *Dynamics and Stability of Systems*, 7(4):219–232, 1992.

[27] E. Buzano. Secondary bifurcations of a thin rod under axial compression. *SIAM Journal on Mathematical Analysis*, 17(2):312–321, 1986.

[28] A. Goriely, M. Nizette, and M. Tabor. On the dynamics of elastic strips. *Journal of Nonlinear Science*, 11(1):3–45, 2001.

[29] C.-L. Lu and N. C. Perkins. Complex spatial equilibria of U-joint supported cables under torque, thrust and self-weight. *International Journal of Non-Linear Mechanics*, 30(3):271–285, 1995.

[30] D. M. Stump. The hockling of cables: a problem in shearable and extensible rods. *International Journal of Solids and Structures*, 37(3):515–533, 2000.

[31] Y. M. Shi, A. E. Borovik, and J. E. Hearst. Elastic rod model incorporating shear and extension, generalized nonlinear Schrödinger equations, and novel closed-form solutions for supercoiled DNA. *Journal of Chemical Physics*, 103(8):3166–3183, 1995.

[32] A. E. Green. The equilibrium and elastic stability of a thin twisted strip. *Proceedings of the Royal Society A*, 154(882):430–455, 1936.

[33] A. E. Green. The elastic stability of a thin twisted strip–II. *Proceedings of the Royal Society A*, 161(905):197–220, 1937.

[34] J. Chopin and A. Kudrolli. Helicoids, wrinkles, and loops in twisted ribbons. *Physical Review Letters*, 111(17):174302, 2013.

[35] Y. Morigaki, H. Wada, and Y. Tanaka. Stretching an elastic loop: Crease, helicoid, and pop out. *Physical Review Letters*, 117(19):198003, 2016.

[36] N. C. Perkins. Planar vibration of an elastica arch: Theory and experiment. *Journal of Vibration and Acoustics*, 112:374–379, 1990.

[37] R. H. Plaut and L. N. Virgin. Vibration and snap-through of bent elastica strips subjected to end rotations. *Journal of Applied Mechanics*, 76(4):041011, 2009.

[38] B. D. Coleman and D. Swigon. Theory of self–contact in Kirchhoff rods with applications to supercoiling of knotted and unknotted DNA plasmids. *Philosophical Transactions of the Royal Society A*, 362(1820):1281–1299, 2004.

[39] R. S. Manning and J. H. Maddocks. Symmetry breaking and the twisted elastic ring. *Computer Methods in Applied Mechanics and Engineering*, 170(3-4):313–330, 1999.

[40] K. A. Hoffman, R. S. Manning, and J. H. Maddocks. Link, twist, energy, and the stability of DNA minicircles. *Biopolymers*, 70(2):145–157, 2003.

[41] F. Tanaka and H. Takahashi. Elastic theory of supercoiled DNA. *Journal of Chemical Physics*, 83(11):6017–6026, 1985.

[42] M. Wadati and H. Tsuru. Elastic model of looped DNA. *Physica D*, 21(2-3):213–226, 1986.

[43] I. Tobias, B. D. Coleman, and W. K. Olson. The dependence of DNA tertiary structure on end conditions: Theory and implications for topological transitions. *Journal of Chemical Physics*, 101(12):10990–10996, 1994.

[44] E. L. Starostin. Three-dimensional shapes of looped DNA. *Meccanica*, 31(3):235–271, 1996.

[45] L. Mahadevan and J. B. Keller. The shape of a Möbius band. *Proceedings of the Royal Society A*, 440(1908):149–162, 1993.

[46] A. Moore and T. J. Healey. Computation of elastic equilibria of complete Möbius bands and their stability. *Mathematics and Mechanics of Solids*, 24(4):939–967, 2019.

[47] D. J. Dichmann, Y. W. Li, and J. H. Maddocks. Hamiltonian formulations and symmetries in rod mechanics. In *Mathematical Approaches to Biomolecular Structure and Dynamics*, pages 71–113. Springer, 1996.

[48] Y. Li and J. H. Maddocks. On the computation of equilibria of elastic rods part I: Integrals, symmetry and a Hamiltonian formulation. ICES REPORT 96-29, The Institute for Computational Engineering and Sciences, The University of Texas at Austin, June 1996. `www.ices.utexas.edu/media/reports/1996/9629.pdf` .

[49] G. Domokos and T. J. Healey. Hidden symmetry of global solutions in twisted elastic rings. *Journal of Nonlinear Science*, 11(1):47–67, 2001.

[50] E. J. Doedel, R. C. Paffenroth, A. R. Champneys, T. F. Fairgrieve, Y. A. Kuznetsov, B. E. Oldeman, B. Sandstede, and X. Wang. AUTO-07P: Continuation and bifurcation software for ordinary differential equations.
`indy.cs.concordia.ca/auto/` , 2007.

[51] M. A. Dias, personal communication.

[52] A. P. Korte, E. L. Starostin, and G. H. M. van der Heijden. Triangular buckling patterns of twisted inextensible strips. *Proceedings of the Royal Society A*, 467(2125):285–303, 2010.

[53] E. L. Starostin and G. H. M. van der Heijden. Equilibrium shapes with stress localisation for inextensible elastic Möbius and other strips. *Journal of Elasticity*, 119(1-2):67–112, 2015.

[54] J. Chopin and A. Kudrolli. Disclinations, e-cones, and their interactions in extensible sheets. *Soft Matter*, 12(19):4457–4462, 2016.

[55] E. L. Starostin and G. H. M. van der Heijden. The shape of a Möbius strip. *Nature Materials*, 6(8):563–567, 2007.

[56] M. A. Dias and B. Audoly. A non-linear rod model for folded elastic strips. *Journal of the Mechanics and Physics of Solids*, 62:57–80, 2014.

[57] B. Audoly and K. A. Seffen. Buckling of naturally curved elastic strips: The ribbon model makes a difference. *Journal of Elasticity*, 119(1-2):293–320, 2015.

[58] J. C. Alexander and S. S. Antman. The ambiguous twist of Love. *Quarterly of Applied Mathematics*, 40(1):83–92, 1982.

[59] G. H. M. van der Heijden, M. A. Peletier, and R. Planqué. On end rotation for open rods undergoing large deformations. *Quarterly of Applied Mathematics*, 65(2):385–402, 2007.

[60] C. B. Prior and S. Neukirch. The extended polar writhe: a tool for open curves mechanics. *Journal of Physics A*, 49(21):215201, 2016.

[61] J. Baillieul. Geometric methods for nonlinear optimal control problems. *Journal of Optimization Theory and Applications*, 25(4):519–548, 1978.

Chapter 3

Exact and approximate mechanisms for pure bending of thin sheets

Attribution

This chapter represents a collaborative work with Prof. James Hanna, who contributed to the work through idea development, editing, and support. This work is presently under revision for publication in *Mechanism and Machine Theory*. It is presented here just as it has been submitted to the journal. The submitted manuscript can be found at: https://arxiv.org/abs/1905.07484.

Abstract

Direct measurement of the moment-curvature response of sheets or wires up to high curvatures can aid in modeling creasing, pleating, and other forming operations. We consider theoretical issues related to the geometry of pure bending. We present a linkage design that, for homogeneous deformation of the sample, results in an exact pure bending state up to arbitrarily high curvature, by combining a cochleoidal trajectory with an angle-doubling mechanism. The full mechanism is single degree of freedom and position controlled, a desirable feature for measurement of soft materials. We also present an optimal approximation to the cochleoid using a more easily implemented circular trajectory, and compare this with an existing commercial system for fabric testing. We quantify the error of the approximate test by calculating the deformation of an Euler *elastica*, a structure with linear moment-curvature response. While the circular mechanism can approximate the exact boundary conditions quite well up to moderately large curvatures, the resulting curvature of the test sample still deviates significantly from homogeneous response. We also briefly discuss ex-

pectations of localization behavior in pure bending tests.

3.1 Introduction

The response of sheet materials to bending is an important element in understanding diverse operations, such as the forming of metallic panels, and pleat and crease formation in fabrics or deployable structures made of composites or polymers. While established standards exist to measure elastic bending moduli at low curvatures or through *elastica* theory for larger deformations, the measurement of elastic-plastic moment-curvature response at high curvatures has been attempted through a variety of disparate approaches.

Ideally one would like to predict deformation in a forming process, involving complex loadings, by employing constitutive information obtained from one or a few simple mechanical tests. A well-known example of such a test involves uniaxial tensile deformation, wherein the ends of a sample are displaced and the material experiences a uniform elongation, unless its properties are such as to promote strain localization. In the present work we consider the analogous operation of pure bending, wherein both the position and orientation of the ends of the sample are prescribed so as to allow a uniform curvature, so long as material properties permit. We detail an exact and a related approximate mechanism for generating this deformation, in which a uniformly deforming sample adopts the shape of circular arcs of decreasing radius. The resulting moment-curvature curve [1] can serve as the primary input to modeling of thin sheet forming processes where in-plane loading and stretching are minimal, such as some pleating and folding operations in which the sheet can be approximated as inextensible. The current work does not address combined stretching and bending conditions which may be important for some applications.

Direct measurement of the moment-curvature response of a sheet is preferable over inference of the bending properties from tensile and compressive measurements for two reasons. First, the sheet material may have complex anisotropic constitutive properties such that reconstruction of the bending behavior is difficult. Second, it is not feasible to measure compressive response of a thin sheet, and for materials produced only in sheet form there may not exist any corresponding bulk object whose compressive response can be measured. In fact, there are situations in which it might be more feasible to infer tensile and compressive behavior from bending measurements [2, 3] than the other way around.

The mechanics of crease formation and recovery have application to textiles and folded deployable structures. Approaches to this question in both fields are typically based on a test geometry in which a piece of material is simply compressed between rigid platens [4, 5, 6, 7, 8, 9, 10, 11], although other approaches to creating a crease have been employed [12, 13, 14, 15]. Extracting moment-curvature data from these or other non-uniform bending tests requires either visual measurements of geometric features or an interpretation of the data in the light of some constitutive information [10, 15, 16, 17, 18].

The earliest position controlled pure bending device of which we are aware is that of Isshi [19], which employed a cochleoidal groove and a set of gears to guide the position and orientation of one end of a fiber or fabric sample. A variant of this device was constructed by Popper and Backer [20]. The Kato Tech KES-FB-2 machine performs a related approximate test as part of a suite of measurements known in the woven fabric community as the Kawabata Evaluation System (KES). Though marketed as a "Pure Bending Tester", the instrument manual indicates a circular, rather than exact cochleoidal, path for the sample end, along with a set of gears and a compensating crank for orientation purposes [21]. In this paper, we present both a design for a linkage to perform an exact pure bending test, as well as an optimal circular approximation, either achievable with a single actuation. In contrast to a uniaxial tensile test, the choice of whether position and orientation control are achieved by manipulating one or both ends of the sample has nontrivial effects on the geometry of the resulting motions. One possible approach to pure bending is a synchronized rotation of both, and linear translation of one or both, ends of the sample using a minimum of three actuators [22]. A more complicated choreographed motion was implemented by Hoefnagels and co-workers in the context of *in situ* SEM of thin films [23].

In theory, pure bending can also be achieved through force control, for example by applying a pure moment to one or both ends of a sheet sample while allowing the end to end distance to change freely. Frictional resistance to this relative motion will prevent achievement of a pure bending state, so such constructions are not ideal for soft materials or weak structures. An early construction by Eeg-Olofsson applied a moment to a textile sample through the action of a magnetic field on a coil floating in a pool of mercury [24]. Seffen and Pellegrino tested composite structures with a device that controls the orientation of the sample ends while allowing them to slide freely on a linear track [25]. An interesting device for composites testing is that of Murphey and co-workers, a fixture for a universal testing machine featuring rotating clamps, ball bearings, and rails [26, 27, 28]. There are other force controlled bending testers that rely on free movement of elements [29, 30], sometimes aided by interconnected pulleys [31, 32, 33].

Many approximate bending tests have been devised for sheet metals and other materials. Some seek to extend the classic four-point test to moderate curvatures by allowing some freedom of motion at the sample ends [34, 35, 36]. Fixtures for universal testing machines have been devised to achieve moderate or high curvature bending [37, 38, 39, 40, 41]. The curvature distribution in such samples is more uniform than in simple compression between two platens, but is still far from uniform. Other works [42, 43] that bend metals up to high curvatures provide little detail about the geometry. Other approaches include end loading with free rotation [44], and direct position control [45, 46].

In this paper, we develop an exact single-degree-of-freedom linkage design that can subject a sheet to pure bending, by augmenting a mechanism to generate motion along a cochleoid with an angle-doubling mechanism. We also present a similar bending mechanism by replacing the cochleoidal motion by a simple circular approximation, and show that an existing commercial fabric tester is close to optimal among this class of approximations. We compare exact and

approximate approaches using the simple Euler *elastica*, and reveal a surprisingly significant deviation in curvatures between the two. We also briefly discuss localization in pure bending.

3.2 The geometry of pure bending, and an exact mechanism

A uniaxial tensile test imposes an increasing distance between the ends of a straight specimen. Under these conditions, some insufficiently work-hardening materials will experience localized deformation in the form of a necking instability. However, most specimens will, for some range of strains, respond with an ideal uniform elongation, allowing measurement of the material's tensile stress-strain curve. Analogously, a pure bending test can provide the moment-curvature response of a sheet if it can impose a deformation such that the sample can respond with an ideal uniform curvature. This means that samples should adopt the shape of circular arcs of decreasing curvature. If one end of the sample is fixed, the motion of the other end will be along a curve known as a cochleoid [47], while the end orientations must also adjust accordingly. The relevant geometric parameters are shown in Figure 3.1. The polar equation of a cochleoid traced by a sample of length L is

$$r(\varphi) = L\frac{\sin\varphi}{\varphi}\,, \tag{3.1}$$

where φ is measured clockwise from the fixed, vertically-oriented end of the sample. The corresponding bending angle $\beta = 2\varphi$ is inversely related to the radius of curvature of the sample, $r_0 = L/\beta$.

We will first present a mechanism to trace the cochleoid, and then add another mechanism to double φ to β at the moving end.

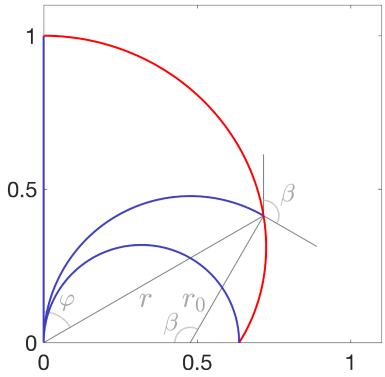

Figure 3.1: Part of a cochleoid (red curve) describing the locus of endpoints of an arc of length $L = 1$ (blue curves) of progressively decreasing radius of curvature r_0. Also shown are the bending angle $\beta = L/r_0$ and the polar coordinates of the cochleoid r and φ, with the latter measured clockwise from the vertical.

3.2.1 A mechanism to generate the cochleoid

The cochleoid sub-mechanism follows the example of Artobolevskii [48], which exploits the inversive relationship between the cochleoid and a special curve known either as the quadratrix of Dinostratus or the trisectrix of Hippias, names that reflect its other potential uses [49]. The quadratrix is easily generated. Its equation $\rho(\varphi)$ is defined by $r(\varphi)\rho(\varphi) = R_{\text{inv}}^2$ for inversion of the cochleoid with respect to a circle of radius R_{inv}. As shown in Figure 3.2a, if a line initially on one side of a square (NP) translates parallel to itself, and another initially perpendicular line (MN) rotates (about M), so that the two lines coincide at their final position on another side (QM) of the square, the quadratrix is the locus of intersection of these two steadily moving lines [49]. Figure 3.2b shows a rack and pinion system (light grey) to move point A along the quadratrix (red dashed line), using the motion of bars EA and IA coupled through sliders at A, with EA fixed perpendicularly to the rack and IA attached to, and rotating with, the pinion wheel. To this system, a Peaucellier-type inversor (grey) is attached at the fixed origin O at the center of the wheel and at point A, so that point C moves along the cochleoid (red solid line). The sample (not shown) has one end fixed at O and the other at the moving point C. This mechanism has only one internal degree of freedom [48].

The inversor links satisfy OB = OD = l, AB = BC = CD = DA = m. The inverting circle relating C and A has its center at O and a radius given by $R_{\text{inv}}^2 = l^2 - m^2$. Points O, C, and A are collinear. As $r(\varphi)$ and $\rho(\varphi)$ respectively describe the positions of points C and A, a bit of trigonometry involving O, B, and the midpoint between A and C provides the expression

$$m^2 - \left(\frac{\rho(\varphi) - r(\varphi)}{2}\right)^2 + \left(r(\varphi) + \frac{\rho(\varphi) - r(\varphi)}{2}\right)^2 = l^2\,,$$

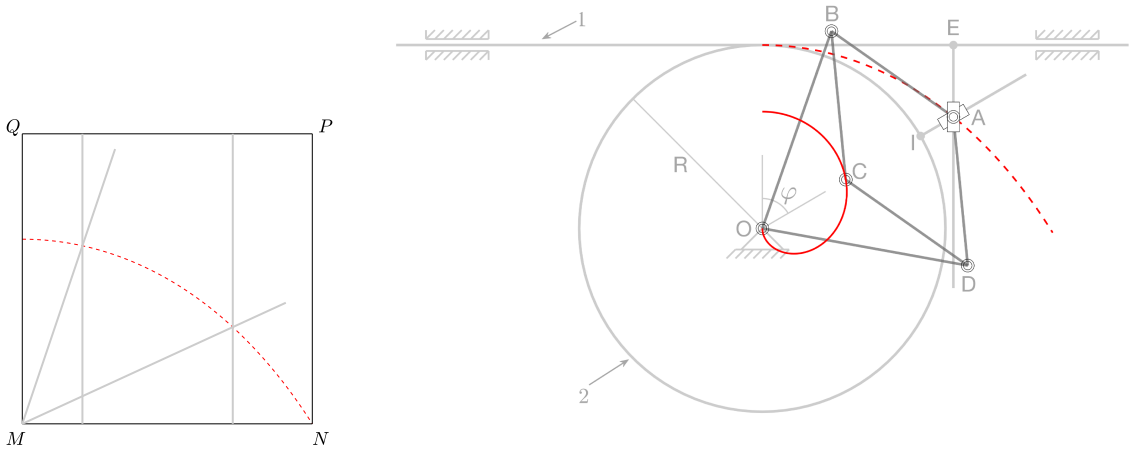

(a) (b)

Figure 3.2: (a) The cochleoid's inverse (dashed red) is given by the locus of intersection of two lines, one initially along NP and translating, the other initially along MN and rotating about M, such that the two later coincide along QM. (b) After [48]. A rack and pinion system (light grey) generates the dashed red curve through translation of bar EA and rotation of bar IA. This curve is inverted into the cochleoid (solid red) by a Peaucellier-type linkage OABCD (grey).

which upon simplification reveals that the wheel size $\rho(0) = R$ is related to the lengths of the links and the sample $r(0) = L$ by $LR = R_{\text{inv}}^2 = l^2 - m^2$.

3.2.2 Adding an angle-doubling mechanism

At the moving point C, the sample end must be oriented at twice the angle from the vertical turned by the wheel, $\beta = 2\varphi$. To double the angle φ, we exploit a simple construction [50] involving identical-length links arranged in a wedge as in Figure 3.3a. The lower triangle corresponds to CGH in Figure 3.3b, where an angle-doubling linkage (black) has been added to the cochleoid mechanism of Figure 3.2b. Bar OC is attached to, and rotates with, the wheel, while bar GC rotates at twice its rate, so that it is oriented at $\beta = 2\varphi$ from the vertical. The distances GH and GC are fixed and identical, bar GH is kept vertical through a double-slider connection at F on the rack, and the hinge-slider at H slides along bar OC. Note that point H passes over point C when $\varphi = \pi/2$. The sample (blue arc) is clamped vertically at the fixed point O and in the orientation of bar GC at the moving point C.

The angular scope of the combined mechanism is limited by a singular parallel configuration adopted by the kite-shaped inversor at a finite angle. The maximum curvature achievable depends on the choice of link lengths and wheel radius, and can be made arbitrarily large. Details are shown in Appendix B.1.

The combined mechanism may be implemented as a multi-level structure. It may also be practical to displace some elements laterally with respect to their positions in Figure 3.3b, namely the connection E and slider F which could sit on a separate parallel track instead of directly on the rack and pinion system. Torque can be measured by a sensor at the origin O. The mechanism has one internal degree of freedom, and can be driven either by a motor to rotate the gear or by a linear actuator to translate the rack.

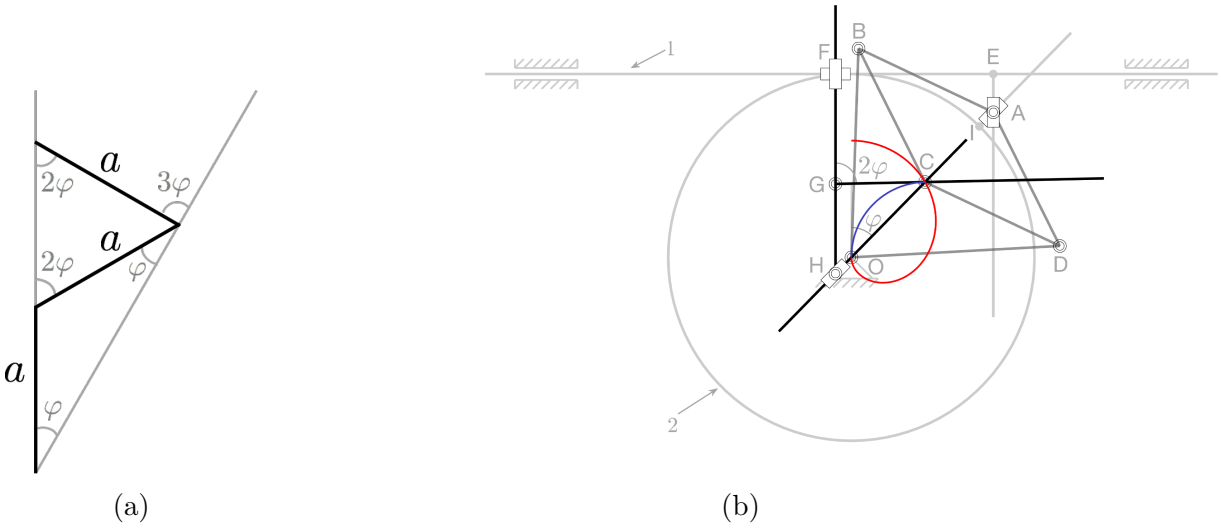

(a) (b)

Figure 3.3: (a) Generating multiples of a fundamental angle φ using equal length links in a wedge [50]. (b) An angle-doubling mechanism (black) is added to the cochleoid mechanism of Figure 3.2b. Bar GC rotates to twice the angle of bar OC. The sample (blue arc) is clamped vertically at the fixed point O and in the orientation of bar GC at the moving point C.

3.3 An approximate circular mechanism, and comparison with other testers

The exact mechanism introduced in Section 3.2 is complex. It is worth investigating whether a simpler approximate mechanism might serve as a reasonable substitute. The approximation we consider involves replacing the cochleoid with a circular arc, similarly to what is done in the commercial KES fabric tester [21], while retaining orientation control through an angle-doubling linkage as in Section 3.2.2. The latter should be comparable or more accurate than the unspecified approximate angular compensation performed by the KES tester [21], and could in theory be replaced by a gear train as in Isshi's tester [19].

We restrict our consideration to circular trajectories that coincide with the cochleoid in the unbent state, and are symmetric with respect to bending in either direction. This leaves

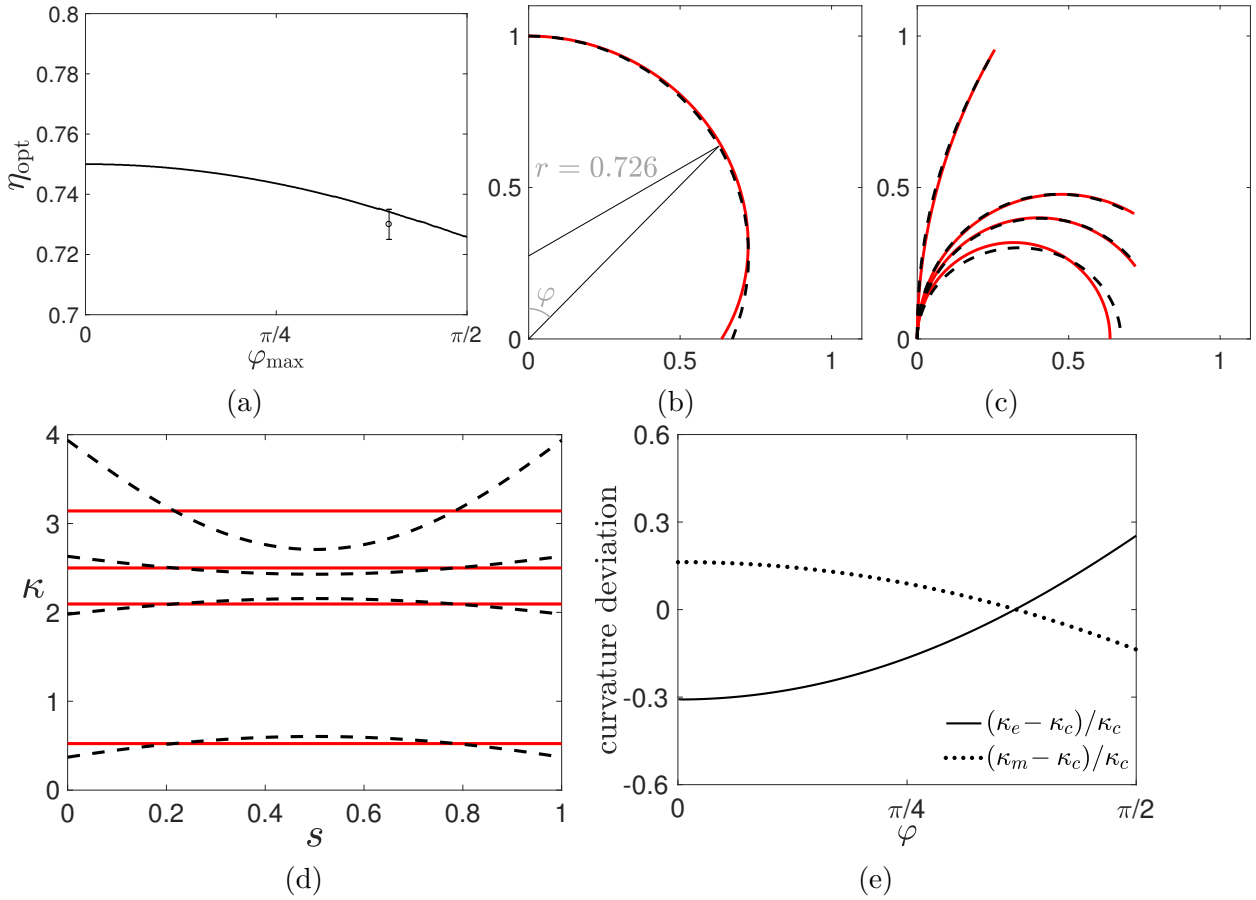

Figure 3.4: (a) Optimal radius η_{opt} of the approximate circular trajectory as a function of the maximum bending angle $\varphi_{\max}$ reached by the tester. The error is comparable to the thickness of the curve. The single data point corresponds to the the KES value 0.73 ± 0.005 at $\varphi_{\max} = \frac{5}{4}$. Other subfigures use the value $\eta_{\text{opt}} = 0.726$ corresponding to $\varphi_{max} = \frac{\pi}{2}$ to compare the response of an Euler *elastica* under exact (solid red) and approximate (dashed black) boundary conditions, including a mechanism to double φ. (b) Sample end positions. (c) Sample configurations and (d) Curvature distributions at bending angles $\varphi = \frac{\pi}{12}, \frac{\pi}{3}, \frac{5}{4}, \frac{\pi}{2}$. (e) Normalized curvature deviations at the ends (solid black) and middle (dotted black) of the sample as a function of the bending angle φ.

only the circle's radius η as a parameter; the polar equation for the circle is $r_a(\varphi;\eta) = \sqrt{\eta^2 - (1-\eta)^2 \sin^2\varphi} + (1-\eta)\cos\varphi$. The circle's center does not sit at the origin, and the angle to be doubled is φ, which is not the angle turned by the circle. We designate the best approximation, for a particular maximum angle $\varphi_{\max}$ reached by the tester, as that which minimizes the area between the approximate circle $r_a(\varphi;\eta)$ and the ideal cochleoid $r(\varphi)$, $\int_0^{\varphi_{\max}} \frac{1}{2}|r(\varphi)^2 - r_a(\varphi;\eta)^2|\, d\varphi$. Numerically determined values of the optimal radius $\eta_{\text{opt}}(\varphi_{max})$ are shown in Figure 3.4a, along with the KES value corresponding to $\eta\left(\frac{5}{4}\right) = 0.73 \pm 0.005$ (we note that the Kato Tech manual [21] states a range of ±0.05, but we believe this must

be a misprint). The KES value is consistent with the optimal circle. For further analysis, we choose a larger maximum angle than that of the KES machine, corresponding to a half-circle configuration $\beta = \pi$, $\varphi_{max} = \frac{\pi}{2}$, whose optimal approximating circle has radius $\eta_{\text{opt}}\left(\frac{\pi}{2}\right) = 0.7257 \pm 0.0001$, which we truncate as $\eta = 0.726$.

Figure 3.4b compares this approximate (dashed black) circular trajectory with the exact (solid red) cochleoidal trajectory. The curves are quite close up to an angle of about $\varphi = \frac{5}{4}$, which is the maximum angle used by the KES tester [21]. However, this is somewhat misleading. If we combine the approximate trajectory with a mechanism to double the angle φ, we can quantitatively compare the response of a particular material to the exact and approximate boundary conditions imposed. We take as the simplest possible example the Euler *elastica*, an inextensible planar curve with linear moment-curvature response. The method of solution is detailed in Appendix B.2. Figures 3.4c and 3.4d show configurations and curvature distributions $\kappa(s)$, where s is the arc length along the curve, for bending angles $\varphi = \frac{\pi}{12}, \frac{\pi}{3}, \frac{5}{4}, \frac{\pi}{2}$; recall that the sample is bent to subtend an angle of 2φ. From Figure 3.4d, we see that the curvature error for an *elastica* has a simple unimodal form, with roughly equal excess and deficit in curvature, and with an inversion at moderate curvatures such that the maximum of curvature changes from being at the middle of the sample to being at the edges as the imposed curvature increases. Figure 3.4e shows the normalized end and middle curvature deviations $(\kappa_e - \kappa_c)/\kappa_c$ and $(\kappa_m - \kappa_c)/\kappa_c$, where κ_e, κ_m and κ_c are the end, middle, and ideal curvatures, for bending up to a half-circle configuration. Despite very small differences in boundary positions up to $\varphi = \frac{5}{4}$, the sample curvature under the approximate mechanism can show significant deviation from the ideal value at low bending angles, on the order of 30%, leading to large errors in measured moment-curvature response. Thus, one would expect discrepancies between bending moduli inferred from such a test and standard low-curvature tests.

3.4 Discussion

Exact information about the end orientations in the KES tester is not available, but we believe the resulting theoretical errors are at least as large as those of the approximate mechanism shown in Figure 3.4, which has a slightly better position approximation, leading to a better orientation approximation.

Aside from theoretical errors, experimental error can arise from difficulties in implementing any mechanism. Given the sensitivity of the curvature distribution to small errors in end position and orientation, it is not surprising to see significant errors in bending strains even in testers with multiple synchronized actuators to control boundary conditions, as for example in Figure 9 of [22]. Our first attempt at implementing the exact mechanism of Section 3.2 has suffered similar issues due to flexibility and excess play of components.

As the mechanism is intended for use on very soft sheets, we have treated the link elements

as rigid lines in our analysis. However, for testing of stiff materials, it is expected that machine stiffness effects will be considerably more complex than in a simple tensile test. In either case, sufficiently thick links should be employed. We have also implicitly assumed quasi-static motions of the mechanism, ignoring any inertial effects.

Our choice of linkage is not unique. An alternate inversor, such as that of Hart, could be used to generate the cochleoid from the quadratrix. We could have employed two cochleoids, or approximate circles, to rotate the sample ends about the center.

The geometry of a pure bend test raises questions not present in the uniaxial tensile test. For example, if we wish to avoid sample failure near the grips, it is not clear what the equivalent of a "dog bone" shaped sample would be. Reducing the cross section, and thus the bending resistance, would lead to a different local curvature that in turn affects the global geometry, and thus the local contact moment along the sample. Another obvious question without an obvious answer is how to interpret localization. What is the equivalent of the Considère criterion for pure bending? The balances of force and moment on an inextensible elastic rod are given by the Kirchhoff equations, which in the absence of body or other distributed forces can be integrated with respect to arc length s to obtain

$$\mathbf{n} = \mathbf{P}\,, \tag{3.2}$$

$$\mathbf{m}(s) + \mathbf{x}(s) \times \mathbf{n} = \mathbf{J}\,, \tag{3.3}$$

where $\mathbf{x}(s)$ is the position of the body, $\mathbf{n}$ and $\mathbf{m}(s)$ are the local contact force and moment, and the constant vectors $\mathbf{P}$ and $\mathbf{J}$ are the conserved force and torque [51]. As the body is only loaded at its ends, the force balance (3.2) indicates that the contact force $\mathbf{n}$ is a constant. From the perspective of quasistatic flow localization [52], we consider perturbations of a base state parameterized by a small increment χ, such that all quantities $() = ()_0 + \frac{d()}{d\chi} d\chi$. Additionally noting that the contact moment is simply a function of the curvature $\kappa(s)$, we obtain a localization criterion from the torque balance

$$\frac{\partial \mathbf{m}(\kappa)}{\partial \kappa} \frac{d\kappa(s)}{d\chi} + \frac{d\mathbf{x}(s)}{d\chi} \times \mathbf{P}_0 + \mathbf{x}_0(s) \times \frac{d\mathbf{P}}{d\chi} = \frac{d\mathbf{J}}{d\chi} = 0\,. \tag{3.4}$$

Whether this criterion is satisfied clearly depends on the loading process. If the base state is pure bending, $\mathbf{P}_0 = 0$, we measure $\mathbf{m}_0 = \mathbf{J}_0$ at the sample end, and $\mathbf{x}_0(s)$ describes an arc of a circle with curvature κ_0, simplifying the equation (3.4) to

$$\frac{\partial \mathbf{m}(\kappa)}{\partial \kappa} = -\frac{\hat{\mathbf{r}}(s)}{\kappa_0} \times \frac{d\mathbf{P}}{d\chi} \Big/ \frac{d\kappa(s)}{d\chi}\,, \tag{3.5}$$

where the unit vector $\hat{\mathbf{r}}$ corresponds to a cylindrical coordinate system sharing its origin with the circular arc of the sample's base state. Choosing a particular shape perturbation $\frac{d\mathbf{x}}{d\chi}$, $\frac{d\kappa}{d\chi}$ follows immediately, as $\kappa^2 = \frac{d^2\mathbf{x}}{ds^2} \cdot \frac{d^2\mathbf{x}}{ds^2}$. However, the induced contact force $\frac{d\mathbf{P}}{d\chi}$ must

be determined from a full solution of the Kirchhoff equations and boundary conditions for the system. Once we know this, we can in principle determine when localization occurs in terms of the slope of the constitutive curve $\frac{\partial \mathbf{m}(\kappa)}{\partial \kappa}$. For a symmetric perturbation, we expect the constant vector $\frac{d\mathbf{P}}{d\chi}$ to be aligned with the end to end vector, and $\frac{d\kappa(s)}{d\chi}$ to have either a maximum in the center or two maxima on the sides, something easily seen by playing with an elastic band. To understand localization, we need to determine how each of these quantities scale with curvature. For a simple Euler *elastica*, perturbative analysis of the shape equation [51] near a circular solution seems to imply that $\frac{d|\mathbf{P}|}{d\kappa} \sim \kappa_0$, but we reserve further analysis for future work.

There appear to be few studies focused on the onset of plastic localization in forming operations where bending is the predominant deformation mode. Triantafyllidis and Samanta considered localization in combined bending and stretching of axisymmetric sheets [53]. Kyriakides and co-workers [54] observed localization arrest and propagation in shallow bending of tubes made from a Lüders-banding steel, and observed initiation of localization near the sides, rather than in the center.

3.5 Conclusions

We have presented exact and approximate single-degree-of-freedom mechanisms for the imposition of pure bending. Curvature in an approximately bent sample can deviate significantly from the nominal constant value. The test geometry raises interesting issues, particularly with regard to localization.

Acknowledgments

This work was supported by The NonWovens Institute (project 16-197). We thank N. A. Corbin, D. Link, and W. D. Hartley II for help building a prototype tester, H. Singh for helpful discussions, and S. Guevel and E. DenHartog for information about the Kato Tech KES-FB-2 machine.

Bibliography

[1] J. Hu, Z. Marciniak, and J. Duncan. *Mechanics of sheet metal forming*. Elsevier, 2002.

[2] V. Laws. Derivation of the tensile stress-strain curve from bending data. *Journal of Materials Science*, 16(5):1299–1304, 1981.

[3] R. A. Mayville and I. Finnie. Uniaxial stress-strain curves from a bending test. *Experimental Mechanics*, 22(6):197–201, 1982.

[4] R. Steele. A method for studying the deformation of fabrics in creasing. *Textile Research Journal*, 27(9):695–700, 1957.

[5] I. M. Stuart, P. Hetherington, and K. Baird. An investigation of cloth bending: Part I: Compression of looped fabrics. *Textile Research Journal*, 36(9):803–808, 1966.

[6] I. M. Stuart and R. K. Mann. An investigation of cloth bending: Part II: The remanent curvature hypothesis. *Textile Research Journal*, 37(7):613–618, 1967.

[7] J. C. H. Yee and S. Pellegrino. Folding of woven composite structures. *Composites Part A: Applied Science and Manufacturing*, 36(2):273–278, 2005.

[8] Y. Satou and H. Furuya. Mechanical properties of z-fold membrane under elasto-plastic deformation. *Journal of Space Engineering*, 4(1):14–26, 2011.

[9] A. C. Abbott, P. R. Buskohl, J. J. Joo, G. W. Reich, and R. A. Vaia. Characterization of creases in polymers for adaptive origami structures. In *ASME 2014 Conference on Smart Materials, Adaptive Structures and Intelligent Systems, Newport, Rhode Island*, page V001T01A009. American Society of Mechanical Engineers.

[10] B.Y. Dharmadasa, H.M.Y.C. Mallikarachchi, and F. López Jiménez. Characterizing the mechanics of fold-lines in thin kapton membranes. In *2018 AIAA Spacecraft Structures Conference, Kissimmee, Florida*, page 0450.

[11] T. Elder, D. Rozairo, and A. B. Croll. Origami inspired mechanics: Measuring modulus and force recovery with bent polymer films. *Macromolecules*, 52:690–699, 2019.

[12] C. O. Bostwick. Comparison of some methods for testing wrinkle recovery. *American Dyestuff Reporter*, 51:386–393, 1962.

[13] J. Skelton. The bending behavior of fabrics at high curvatures. *Textile Research Journal*, 41(2):174–181, 1971.

[14] A. Benusiglio, V. Mansard, A.-L. Biance, and L. Bocquet. The anatomy of a crease, from folding to ironing. *Soft Matter*, 8:3342–3347, 2012.

[15] G. Secheli, A. Viquerat, and G. Aglietti. The modeling of packaging folds in thin polymer films. AIAA SciTech Forum, doi:10.2514/6.2019-2254, 2019.

[16] T. G. Clapp, H. Peng, T. K. Ghosh, and J. W. Eischen. Indirect measurement of the moment-curvature relationship for fabrics. *Textile Research Journal*, 60(9):525–533, 1990.

[17] G. Sanford, A. Biskner, and T. Murphey. Large strain behavior of thin unidirectional composite flexures. In *51st AIAA/ASME/ASCE/AHS/ASC Structures, Structural Dynamics, and Materials Conference. Orlando, Florida*, page 2698, 2010.

[18] A. H. Sharma, TJ Rose, A. Seamone, T. W. Murphey, and F. López Jiménez. Analysis of the column bending test for bending of high strain composites. AIAA SciTech Forum, doi:10.2514/6.2019-1746, 2019.

[19] T. Isshi. Bending tester for fibers, yarns and fabrics. *Journal of the Textile Machinery Society of Japan*, 3(2):48–52, 1957.

[20] P. Popper and S. Backer. Instrument for measuring bending-moment curvature relationships in textile materials. *Textile Research Journal*, 38(8):870–873, 1968.

[21] Manual for pure bending tester KES-FB-2. Kato Tekko Co., Ltd., Kyoto.

[22] H. Koyama and K. Kawada. Development of computer-aided bending test machine. *Advanced Technology of Plasticity*, 3:1501–1506, 1990.

[23] J. P. M. Hoefnagels, A. P. Ruybalid, and C. A. Buizer. A small-scale, contactless, pure bending device for *in-situ* testing. *Experimental Mechanics*, 55(8):1511–1524, 2015.

[24] T. Eeg-Olofsson. Some mechanical properties of viscose rayon fabrics. *Journal of the Textile Institute Transactions*, 50(1):T112–T132, 1959.

[25] K. A. Seffen and S. Pellegrino. Deployment dynamics of tape springs. *Proceedings of the Royal Society A*, 455(1983):1003–1048, 1999.

[26] G. E. Sanford, E. V. Ardelean, T. W. Murphey, and M. M. Grigoriev. High strain test method for thin composite laminates. In *16th International Conference on Composite Structures. Porto, Portugal*, 2011.

[27] M. E. Peterson and T. W. Murphey. Large deformation bending of thin composite tape spring laminates. In *54th AIAA/ASME/ASCE/AHS/ASC Structures, Structural Dynamics, and Materials Conference. Boston, Massachusetts*, page 1667, 2013.

[28] T. W. Murphey, M. E. Peterson, and M. M. Grigoriev. Large strain four-point bending of thin unidirectional composites. *Journal of Spacecraft and Rockets*, 52(3):882–895, 2015.

[29] G. Arnold, S. Calloch, D. Dureisseix, and R. Billardon. A pure bending machine to identify the mechanical behaviour of thin sheets. In *6th. International ESAFORM Conference on Material Forming, Salerno, Italy*, pages 1–4, 2003.

[30] S. H. A. Boers, M. G. D. Geers, and V. G. Kouznetsova. Contactless and frictionless pure bending. *Experimental Mechanics*, 50(6):683–693, 2010.

[31] R. G. Hill and W. E. Anderson. The engineering properties of polymer matrix composite materials by a pure moment test. In *Composite Materials: Testing and Design (Second Conference)*, pages 219–236. ASTM International, 1972.

[32] J. M. Muñoz-Guijosa, V. Rodríguez de la Cruz, D. Fernández Caballero, A. Díaz Lantada, and J. Echávarri Otero. Simple testing system for pure bending tests with large deflections. *Experimental Mechanics*, 52(7):679–692, 2012.

[33] A. B. Perduijn and S. M. Hoogenboom. The pure bending of sheet. *Journal of Materials Processing Technology*, 51(1-4):274–295, 1995.

[34] S. Kyriakides and P. K. Shaw. Inelastic buckling of tubes under cyclic bending. *Journal of Pressure Vessel Technology*, 109(2):169–178, 1987.

[35] T. B. Zineb, A. Sedrakian, and J. L. Billoet. An original pure bending device with large displacements and rotations for static and fatigue tests of composite structures. *Composites Part B: Engineering*, 34(5):447–458, 2003.

[36] S. J. Cimpoeru and N. W. Murray. The large-deflection pure bending properties of a square thin-walled tube. *International Journal of Mechanical Sciences*, 35(3-4):247–256, 1993.

[37] Z. Marciniak and K. Kuczyński. The forming limit curve for bending processes. *International Journal of Mechanical Sciences*, 21:609–621, 1979.

[38] J. L. Duncan, S.-C. Ding, and W.-L. Jiang. Moment-curvature measurement in thin sheet–part I: equipment. *International Journal of Mechanical Sciences*, 41:249–260, 1999.

[39] J. L. Duncan, S.-C. Ding, and W.-L. Jiang. Moment-curvature measurement in thin sheet–part II: yielding and kinking in aged steel sheet. *International Journal of Mechanical Sciences*, 41:261–267, 1999.

[40] M. Weiss, H. Wolfkamp, B. F. Rolfe, P. D. Hodgson, and E. Hemmerich. Measurement of bending properties in strip for roll forming. In *International Deep Drawing Research Group 2009 International Conference. Golden, CO*, pages 521–532, 2009.

[41] J. M. Fernandez and T. W. Murphey. A simple test method for large deformation bending of thin high strain composite flexures. In *2018 AIAA Spacecraft Structures Conference. Kissimmee, Florida*, page 0942.

[42] M. Brunet, F. Morestin, and S. Godereaux. Nonlinear kinematic hardening identification for anisotropic sheet metals with bending-unbending tests. *Journal of Engineering Materials and Technology*, 123:378–383, 2001.

[43] J. Carbonnière, S. Thuillier, F. Sabourin, M. Brunet, and P. Y. Manach. Comparison of the work hardening of metallic sheets in bending-unbending and simple shear. *International Journal of Mechanical Sciences*, 51:122–130, 2009.

[44] M. R. Wisnom. On the high compressive strains achieved in bending tests on unidirectional carbon-fibre/epoxy. *Composites Science and Technology*, 43(3):229–235, 1992.

[45] W. Goldacker, S. I. Schlachter, R. Nast, H. Reiner, S. Zimmer, H. Kiesel, and A. Nyilas. Bending strain investigations on BSCCO(2223) tapes at 77 K applying a new bending technique. In *Advances in Cryogenic Engineering: Proceedings of the International Cryogenic Materials Conference*, volume 48, pages 469–476, 2002.

[46] D. L. Harris, A. A. Allegritti, M. Takayasu, and J. V. Minervini. Pure bending strand test of high performance Nb_3Sn wires. In *Advances in Cryogenic Engineering: Transactions of the International Cryogenic Materials Conference*, volume 54, pages 341–348, 2008.

[47] R. Ferréol. Cochleoid, Encyclopédie des Formes Mathématiques Remarquables. Prix Anatole Decerf 2008.

[48] I. I. Artobolevskii. *Mechanisms for the generation of plane curves*. Pergamon, 1964.

[49] T. L. Heath. *A History of Greek Mathematics*. Oxford University Press, 1960.

[50] J. Bryant and C. Sangwin. *How Round Is Your Circle?* Princeton University Press, 2008.

[51] H. Singh and J. A. Hanna. On the planar *elastica*, stress, and material stress. *Journal of Elasticity*, 136(1):87–101, 2019.

[52] S.L. Semiatin and J.J. Jonas. *Formability and Workability of Metals: Plastic Instability and Flow Localization*. ASM, Metals Park, OH, 1984.

[53] N. Triantafyllidis and S. K. Samanta. Bending effects on flow localization in metallic sheets. *Proceedings of the Royal Society of London A*, 406:205–226, 1986.

[54] S. Kyriakides, A. Ok, and E. Corona. Localization and propagation of curvature under pure bending in steel tubes with Lüders bands. *International Journal of Solids and Structures*, 45:3074–3087, 2008.

Chapter 4

Mechanics of pleating

The work presented in this chapter comes from an ongoing project studying mechanics of pleating. The contents of this chapter have not been published yet.

Attribution

The work presented in this chapter was done in collaboration with J. A. Hanna, who contributed to the work through idea development, editing, and support.

Abstract

The purpose of this study is to understand what combinations of processing and material parameters lead to successful pleat forming in soft textile sheets. Mechanical pleating is an elastic-plastic bending process that we formulate as a multi-point variable-arc-length boundary value problem for an inextensible rod, with a moment-curvature constitutive law as input. By assigning a certain moment-curvature response to pleating materials, and modeling the pleats as nonlinear hinges, we are able to conduct parametric simulations of the rotary pleating process in terms of processing and material parameters. We find that the horizontal space between the sleeve edge, where soft sheets are continuously injected in, and the pleated pack plays a key role in determining if any undesired localization/kink will occur. Other factors such as the pleat strength, pleat stiffness, and flexibility of the pleated pack also influence the pleating results. We obtain pleatability surfaces that identify portions of the parameter space which lead to successful/unsuccessful pleating. Our approach and results can be adapted to study other pleating processes, and inform models of folded deployable structures.

4.1 Introduction

Mechanical pleating is a long-standing technique that deforms thin sheets into accordion-like filter structures through pleat forming [1]. It is unknown what mechanical properties and/or microstructural parameters affect the success of pleating of nonwoven filter materials. Undesired localization occurs in pleating processes. We are particularly interested in understanding the physics behind the undesired localization, and helping the industry avoid pleating failures by adjusting the processing and material parameters.

Pleating falls under the general description of an elastic-plastic forming process followed by springback to a rest configuration. Pleats hold the overall shape of the pleated structures and the final shape is a competition between the mechanics of the pleats and the flexibility of the facets [2, 3]. Such processes applied to thin sheets have been studied at length for metallic materials in the automotive and other industries [4, 5]. Aside from the sheet forming community, there have been some studies on the mechanics of crease formation in elastic structures from folding-like compressive processes [6, 7, 8, 9]. Knowing the mechanics of creases/folds is key to predict the shapes, deployed and folded sizes, and dynamics of folded deployable structures ([10, 11, 12, 13, 14, 15]). Pleated structures are also commonly seen in nature, such as insect wings and plant leaves [16, 17, 18]. The pleated construction makes insect wings very light and also stiff enough to resist inertial and aerodynamic loads.

Pleating processes can be simplified as plane strain problems because pleated structures are usually thin and wide, and the deformation along the width direction is generally uniform. The current study focuses on the mechanics of the rotary pleating process (see Figure 4.1a [1].). There may be other factors that influence the pleating results, such as thermal processing, which are beyond the scope of this study. Based on an inextensible rod model, we formulate the rotary pleating process as a boundary value problem (BVP), where the moment-curvature relationship of pleating materials may be input as a constitutive law. Moment-curvature relationships up to moderate radii of curvature have been obtained and successfully employed to predict the forming response of sheet metals ([4, 19, 20, 21, 22, 23, 24]) and to understand large-deformation bending behaviors of thin high strain composites [25, 26]. The moment-curvature relationship of thin sheets can be measured with a bend tester [21, 26, 27, 28, 29, 30]. In this study, we use a hyperbolic tangent function to characterize the moment-curvature relationship of pleating materials that have an elastic-plastic response.

In a mechanical pleating process, materials typically enter the system through a sleeve-like boundary condition. Recently, it has been shown that across the sleeve edge, the axial force within the sleeve is not the same as the tension immediately on the other side [31, 32, 33]. A compressive force inside the flat sleeve will be generally amplified at the free side [34], while a tensile force within the sleeve will be reduced [35]. We have included the sleeve boundary condition and also the flexibility and movement of the pleated pack into our rotary pleating model.

Our rotary pleating model consists of a multi-point variable-arc-length BVP that incorporates continuous injection of materials and simultaneous pleating of multiple segments. The technique proposed by Ascher and Russell to formulate a multi-point variable-arc-length BVP as a standard two-point BVP, which can be solved by general purpose BVP solvers [36], has been successfully applied to study various boundary value problems [37, 38, 39]. We also adopt this technique and further solve the reformulated standard BVP with the continuation package AUTO 07P [40].

The current paper is organized as follows. In section 4.2, we introduce the rotary pleating model and the idea of reformulating a multi-point BVP into a standard two-point BVP. We define processing and material parameters. In section 4.3, we discuss several types of boundary conditions in the rotary pleating process. In section 4.4, we present numerical pleating results as bifurcation diagrams and pleatability surfaces. We discuss a few additional points of interest in Section 4.5.

4.2 Rotary pleating models and constitutive laws

The rotary pleater typically has two sets of rolls through which the soft sheets travel (see Figure 4.1a [1].). The first set of rolls employs score bars to weaken the sheets locally by scoring at the eventual pleat locations [1]. Soft sheets are then pushed out from the sleeve on the left into the flexible pack on the right. However, sometimes plastic localization occurs in unwanted locations, as shown in Figure 4.1d. We want to understand what combinations of material and processing parameters lead to successful rotary pleating.

In the rotary pleating process, materials being pleated are divided into several segments by the pleats. Each segment is regarded as a one-dimensional inextensible rod. We consider a planar deformation of an inextensible rod with some moment-curvature relation $M(\kappa)$. In our rotary pleating model, the material is being pushed from the sleeve, with the (negative) tension being an unknown scalar variable. The boundary conditions at the internal pleat are that the position, contact force, and contact moment are continuous. In addition, we need a constitutive model for the pleats themselves. These could, for example, be modeled as elastic-perfectly-plastic hinges.

The full rotary pleating model is shown in Figure 4.1b, where we have incorporated the flexibility and movement of the right pack. A minimal model that studies only the first two pleating segments, because of the periodic nature of the pleating process, is shown in Figure 4.1c. The steady moving speed of the right pack can be determined by the insertion speed of the material and the geometric parameter $\frac{d}{2l}$, where d and l are the pleating pitch and pleating depth of the pleated pack. The horizontal movement of the pleated pack, which is on the right side of the vertical gray line that represents the horizontal space h between the sleeve edge and the right pack, is constrained: 1) The leftmost pleat inside the pack is horizontally coupled with a linear spring that has a stiffness of K_s; 2) The other pleats

inside the pack move with a constant speed of $v_p = \frac{d}{2l} v_m$, where v_p is the horizontal traveling speed of the pack and v_m is the injection speed of materials. A rigid pack can be achieved by assigning v_p to all the pleats inside the pack. Processing parameters include $\frac{h}{l}$ and $\frac{y_{P_1}}{l}$. In Figure 4.1d, we show an undesired localization/kink based on a still from a real rotary pleater.

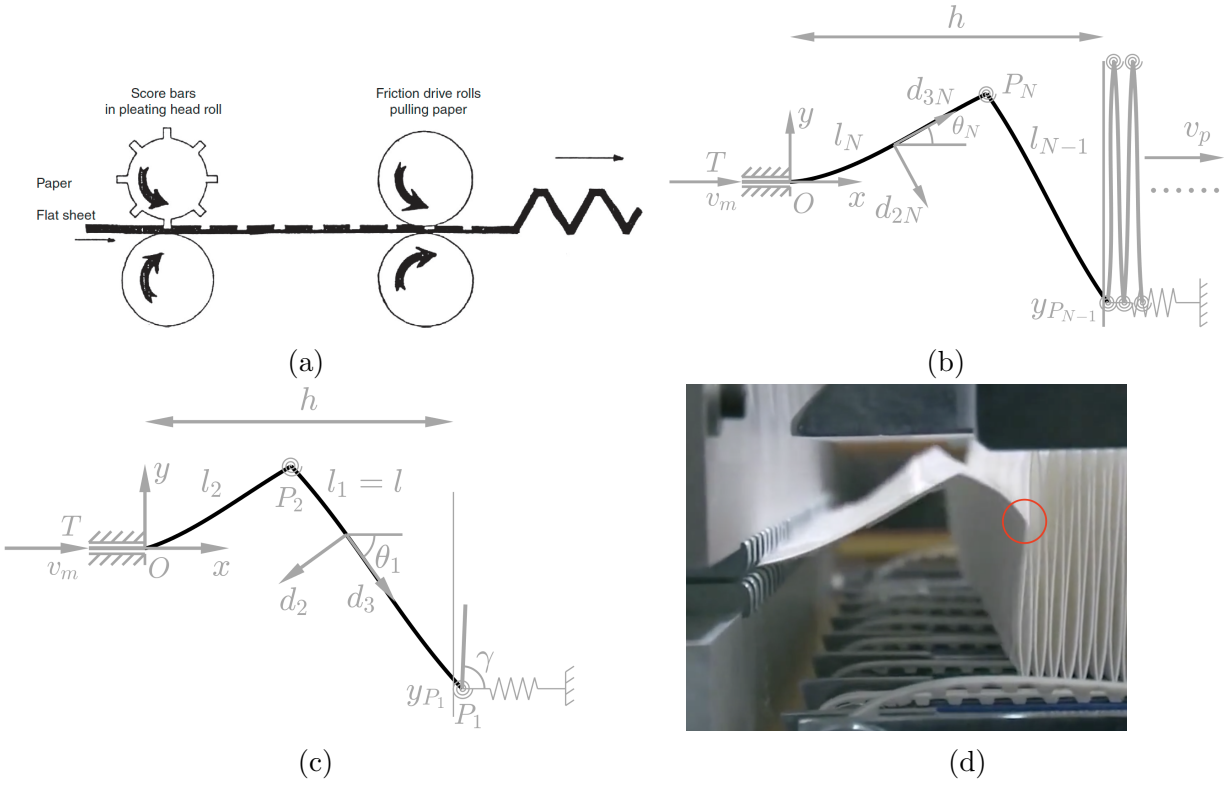

Figure 4.1: Rotary pleating: (a) A schematic of rotary pleating [1]. The left set of rolls employs score bars to weaken the sheets and the right set of rolls is used as an anvil. Sheets, weakened locally by scoring at the eventual pleat locations, are pushed out from the sleeve on the left into the flexible pack on the right. (b) Inextensible rod model for the rotary pleating process: Shown are N segments in total. Materials are continuously injected from the left sleeve. The length of the N_{th} segment keeps increasing until it reaches l, followed by insertion of a new pleat and a new segment. $(\boldsymbol{d}_{1i}, \boldsymbol{d}_{2i}, \boldsymbol{d}_{3i})$ is a right-handed orthonormal frame attached to the i_{th} segment. θ_i measures the angle between the tangent direction $\boldsymbol{d}_{3i}$ and the x axis. A linear spring is coupled to the leftmost pleat of the pack and a constant speed v_p is assigned to the other pleats inside the pack. (c) A minimal rotary pleating model that only studies the first two pleating segments. (d) Shown inside the red circle is an undesired localization/kink (taken from the video by Doublewin Corporation [41]).

A right-handed orthonormal frame $(\boldsymbol{d}_1, \boldsymbol{d}_2, \boldsymbol{d}_3)$ is attached to each segment, with $\boldsymbol{d}_1$ pointing out of the figure. The governing equations for the i_{th} pleating segment (both pleats and segments counted from right to left) can be written as

$$
\begin{aligned}
N_{2i}' - N_{3i}\kappa_i l_i &= 0\,,\\
N_{3i}' + N_{2i}\kappa_i l_i &= 0\,,\\
M_i'(\kappa_i) - N_{2i} l_i &= 0\,,\\
\theta_i' &= \kappa_i l_i\,,\\
x_i' &= l_i \cos\theta_i\,,\\
y_i' &= l_i \sin\theta_i\,,
\end{aligned}
\tag{4.1}
$$

where l_i represents the length of the i_{th} pleating segment. Throughout this work, a prime will denote an s_i derivative where s_i is the normalized coordinate, i.e., $s_i \in [0,1]$ for all the segments. Different segments "communicate" with each other through the connecting pleats. In the rotary pleating process, as material enters the system, the length of the leftmost segment continuously increases and can be used as a continuation parameter. We set the length of other finished pleating segments to 1.

Material enters our problem through a sleeve-like boundary condition. It has been shown that the negative tension T applied within the sleeve is not the same as the tension immediately on the other side [31, 32], and the compressive force inside the sleeve will be "amplified" at the free side [34]. If there is no plastic deformation at the sleeve edge, $(N_3 + M\kappa - \int M\kappa' ds)$ will be a conserved quantity [33]. Here N_3 is the tension inside the rod and M is the contact moment. The integral can be carried out once the moment-curvature relationship is specified. By evaluating the conserved quantity at the left and right side of the sleeve edge, we can immediately get a boundary condition that couples the jump in tension and moment.

We use a hyperbolic tangent function with a small linear term $M = A\tanh(B\kappa) + \epsilon\kappa$ to describe the moment-curvature relationship of the pleating materials. ϵ controls the final slope of the curve. By setting $\epsilon < 0\,, \epsilon = 0$, and $\epsilon > 0$, we can get a moment-curvature relationship that mimics strain-softening behavior, perfectly plastic behavior, and strain-hardening behavior, respectively. With $\epsilon \leq 0$, our rotary pleating model will break down when a kink occurs, where the curvature blows up locally. In all the simulations, we set ϵ to be a small number 0.001. When $\kappa = 0$, $\frac{dM}{d\kappa}|_{\kappa=0} = AB + \epsilon \approx AB$. Here AB is the material stiffness at the origin and has a unit of $N{\cdot}m^2$. When κ goes to large values, $\frac{dM}{d\kappa}|_{\kappa\to+\infty} \approx \epsilon$. A typical diagram with different values of ϵ is shown in Figure 4.2.

We model a pleat as a discrete nonlinear hinge and use another hyperbolic tangent function $M_p = C\tanh D(\theta - \theta_0)$ to describe the moment-angle relationship of it. CD is the pleat stiffness at the rest crease angle $\theta = \theta_0$ and has a unit of $N{\cdot}m$. In this work, we always set θ_0 to π, i.e. the pleat has a flat rest configuration after being scored. $\frac{AB}{CD}$ defines a length, which is similar to the *origami length* that determines whether the deformation of creases or facets is dominant in creased thin strips [11]. Here we adopt nonlinear constitutive laws for both the facets and the pleats, and $\frac{AB}{CD}$ controls the mechanical response only in the linear regime, i.e. around the origin. Once the pleat enters the plateau, it becomes almost completely soft. In numerics, $\frac{AB}{CD}$ should be compared with the length of the pleating segment that is

normalized to 1. Additionally, we assume both the materials and the pleats behave elastically and ignore the likely hysteresis that could influence unloading in the pleating process. With $M(\kappa) = A\tanh(B\kappa) + \epsilon\kappa$ being the moment-curvature relationship of pleating materials, the aforementioned sleeve boundary condition can be evaluated as

$$T - N_{3N}(0) = A\kappa_N(0)\tanh(B\kappa_N(0)) - \frac{A}{B}\ln[\cosh(B\kappa_N(0))] + \frac{\epsilon}{2}\kappa_N^2(0), \tag{4.2}$$

where T is the negative tension inside the sleeve, and $N_{3N}(0)$ and $\kappa_N(0)$ are the axial force and curvature in the N_{th} rod right at the sleeve edge, respectively.

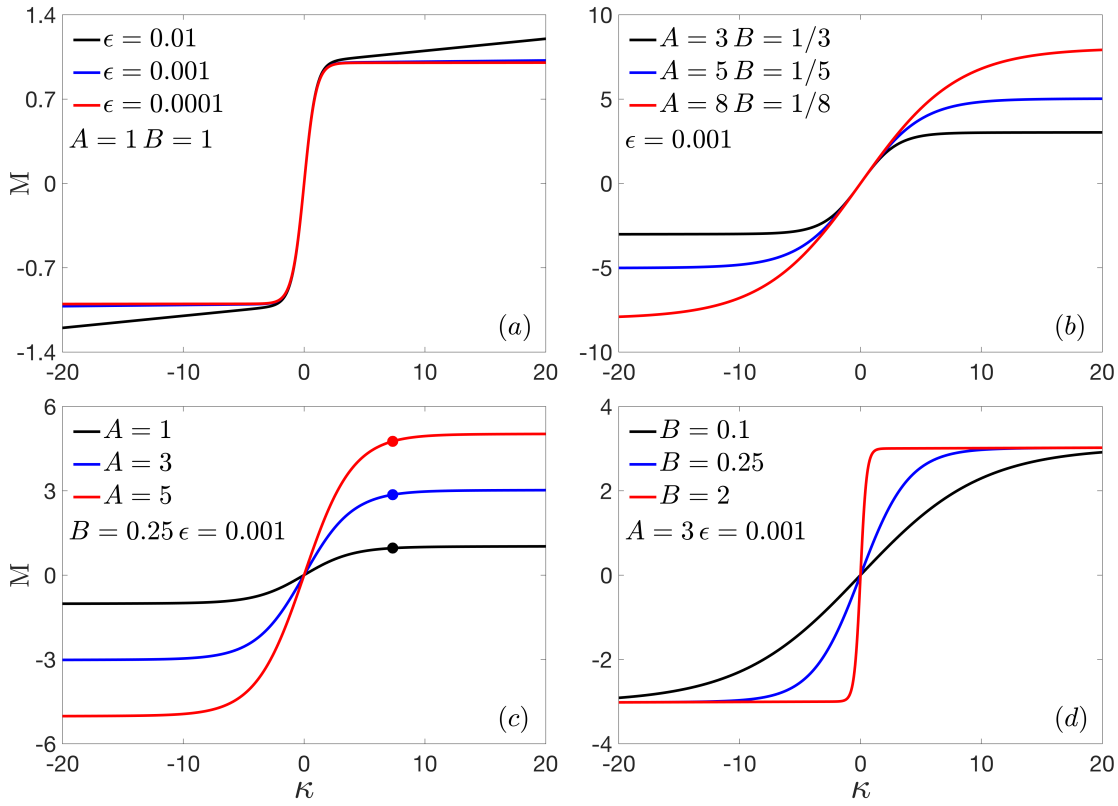

Figure 4.2: A hyperbolic tangent function with a small linear term $M = A\tanh(B\kappa) + \epsilon\kappa$: (a) Varied final slopes. (b) Varied localization curvatures and plateau moments with fixed initial stiffness (i.e., fixed AB). (c) Varied plateau moments with solid circles corresponding to a moment of $0.95A$. (d) Varied localization curvatures.

It is the competition between the mechanics of the pleats and the flexibility of the pleating segments that determines the shape and mechanical properties of the pleated structures. We define pleat strength P_{stren} as $\frac{C}{A}$, and pleat stiffness P_{stiff} as $\frac{CD}{AB}$. The pleat stiffness $\frac{CD}{AB}$ cannot be too small, otherwise the pleat will never reach the plateau moment, defined as $0.95C$. Here, a very large pleat stiffness simply means that the pleat will reach a plateau at a small bending angle. We assume that for a pleat with a flat rest configuration of π, the

angle at which the pleat reaches $0.95C$ should be larger than $\frac{\pi}{2}$, which leads us to consider only $\frac{P_{stiff}}{P_{stren}}B \geq 1.166$. Additionally, we assume a mirror symmetry between the upper and lower pleats and set $\frac{y_{P_1}}{l}$ to a fixed value of -0.5. Here we have neglected the inclination and deformation of the pleated pack. Under this assumption, our numerical results show that the vertical position of the upper pleats is very close to 0.5, which suggests that fixing the vertical position of the bottom pleats at -0.5 is reasonable. To summarize, in the rotary pleating model, processing parameters include $\frac{h}{l}$ and $\frac{y_{P_1}}{l}$. Material properties include: A, B, $P_{stren} = \frac{C}{A}$, $P_{stif} = \frac{CD}{AB}$, and the stiffness of the linear spring K_s that simulates the flexibility of the pleated pack.

4.3 Boundary conditions

We introduce a pre-pleating step to deform the first two pleating segments from flat into a configuration that fits the processing parameters of the pleater (see Figure 4.1c). In this step, the rightmost pleat P_1 moves continuously downward, and the length of the second pleating segment l_2 becomes an unknown scalar that is part of the solution. We introduce a trivial ordinary differential equation (ODE) $l_2' = 0$ to turn the variable-arc-length problem into a standard form. We set the axial force at the free side of the sleeve edge to zero, which helps insert a linear hinge with a rest length to the pleat P_1. The pleat P_1 is finally positioned at (h, y_{P_1}) to fit the processing parameters and a linear spring is attached to it to simulate the flexibility of the pack. The vertical position of the pleat P_1 is fixed.

The next step is to "turn on" the numerical pleating by continuously injecting materials from the left sleeve (see Figure 4.1b and 4.1c). In this step, the compression T inside the sleeve becomes an unknown scalar, while l_N (i.e., the length of the pleating segment that is connected to the sleeve) becomes a continuation parameter controlling the injection of material. We introduce a trival ODE $T' = 0$ to incorporate T into the boundary value problem. When l_N reaches 1, another pleat should be inserted right at the sleeve edge, followed by growing the $(N+1)_{th}$ pleating segment from 0 to 1.

In the rotary pleating process, there are several types of boundary conditions. The left end, where pleating materials are injected, corresponds to a *sleeve boundary condition*. The pleats between the sleeve edge and the pleated pack are termed *free pleats*. Note that in the rotary pleating process, the number of the *free pleats* can be either one or two. The pleats inside the pack are termed *constrained pleats*. The *constrained pleats* may further include two types: 1) The leftmost pleat inside the pack is termed a *flexibly constrained pleat* if a linear spring is attached to it; 2) All the other pleats inside the pack are termed *rigidly constrained pleats* and are given a constant speed of $\frac{d}{2l}v_m$. Considering N pleating segments with N pleats in total, we have $(6N+1)$ state variables (including the unknown scalar T). The fixed sleeve edge gives four boundary conditions and the rightmost pleat P_1 contains three boundary conditions. At each internal pleat, six boundary conditions/constraints need to be specified

to impose the continuity of positions and the balance of forces and moments. In total we get $(6N+1)$ boundary conditions, leading to a well-posed boundary value problem. We count the pleats and segments from right to left (see Figure 4.1b). At the rightmost (bottom) pleat we have:

$$x_1(1) = \frac{h}{l} + \delta_1 + (N - 3 - l_{30} + l_N)\frac{d}{2l}, y_1(1) = \frac{y_{P_1}}{l}, M_1(1) = M_p(\theta_1(1), \gamma), \tag{4.3}$$

where $\frac{y_{P_1}}{l} = -0.5$, and l_N is the length of the leftmost segment and serves as the continuation parameter. l_{30} is the inserting length of the third segment when the second pleat touches the gray line that represents the horizontal space (see Figure 4.1b). δ_1 is the horizontal displacement of the first pleat under the action of the linear spring before the second pleat touches the gray line. γ is related to the shape factor through $\gamma = \cos^{-1}(\frac{d}{2l})$. At the i_{th} *rigidly constrained pleat* ($i \in [2, N-3]$ for two *free pleats* and $i \in [2, N-2]$ for one *free pleat*) we have ,

$$\begin{aligned} x_{i-1}(0) = x_i(1), y_{i-1}(0) = y_i(1), x_i(1) = \frac{h}{l} + \delta_i + (N - i - 2 - l_{30} + l_N)\frac{d}{2l}, \\ y_{i-1}(0) = \frac{y_{P_{i-1}}}{l}, \kappa_{i-1}(0) = \kappa_i(1), M_i(1) = M_p(\theta_{i-1}(0), \theta_i(1)), \end{aligned} \tag{4.4}$$

where l_N and l_{30} has the same meaning as in equation (4.3). δ_i is the horizontal displacement of the i_{th} pleat under the action of the linear spring before the $(i+1)_{th}$ pleat touches the gray line. For the bottom pleats, we have $\frac{y_{P_{i-1}}}{l} = -0.5$. For the upper pleats, $\frac{y_{P_{i-1}}}{l}$ is set to the value when the $(i-1)_{th}$ pleat first touches the gray line, and we find it is always very close to 0.5. At the unique *flexibly constrained pleat*, i.e. $i = N-1$ (one *free pleat*) or $i = N-2$ (two *free pleats*), we have

$$\begin{aligned} x_{i-1}(0) =& x_i(1), y_{i-1}(0) = y_i(1), y_{i-1}(0) = \frac{y_{P_{i-1}}}{l}, \\ \kappa_{i-1}(0) =& \kappa_i(1), M_1(1) = M_p(\theta_{i-1}(0), \theta_i(1)), \\ K_s\left(x_{i-1}(0) - \frac{h}{l}\right) =& N_{3(i-1)}(0)\cos\theta_{i-1}(0) + N_{2(i-1)}(0)\sin\theta_{i-1}(0) \\ & - N_{3i}(1)\cos\theta_i(1) - N_{2i}(1)\sin\theta_i(1), \end{aligned} \tag{4.5}$$

where $\frac{y_{P_{i-1}}}{l}$ has the same meaning as in equation (4.4). At the *free pleat*, i.e., $i = N$ (one *free pleat*) or $i \in [N-1, N]$ (two *free pleats*) , we have

$$\begin{aligned} x_{i-1}(0) = x_i(1), y_{i-1}(0) = y_i(1), \kappa_{i-1}(0) = \kappa_i(1), M_1(1) = M_p(\theta_{i-1}(0), \theta_i(1)), \\ N_{3(i-1)}(0)\cos\theta_{i-1}(0) + N_{2(i-1)}(0)\sin\theta_{i-1}(0) - N_{3i}(1)\cos\theta_i(1) - N_{2i}(1)\sin\theta_i(1) = 0, \\ N_{2(i-1)}(0)\cos\theta_{i-1}(0) - N_{3(i-1)}(0)\sin\theta_{i-1}(0) - N_{2i}(1)\cos\theta_i(1) + N_{3i}(1)\sin\theta_i(1) = 0. \end{aligned} \tag{4.6}$$

At the sleeve boundary condition, we have

$$
\begin{aligned}
&x_N(0) = 0, y_N(0) = 0, \theta_N(0) = 0\,, \\
&T - N_{3N}(0) = A\kappa_N(0)\tanh(B\kappa_N(0)) - \frac{A}{B}\ln[\cosh(B\kappa_N(0))] + \frac{\epsilon}{2}\kappa_N^2(0)\,.
\end{aligned} \tag{4.7}
$$

4.4 Rotary pleating results

We use the continuation package AUTO 07P [40] to solve the BVP system consisting of equation (4.1), $T' = 0$, and the boundary conditions in section 4.3. Figure 4.3 shows numerical results of a successful rotary pleating with multiple segments. It is interesting that the compressive force T inside the sleeve is "amplified" at the free side, which agrees with the results in [34]. The jump/discontinuity in Figure 4.3 is caused by the "sudden" insertion of pleats. This is achieved by decreasing the pleat stiffness P_{stif} from a large value to the real pleat stiffness in an independent continuation step, in which a new (virtual) segment of zero length has been introduced right at the sleeve edge. In this step, the boundary conditions at the sleeve edge are the same as the ones with a segment of non-zero length at the sleeve edge. The next step is to "grow" the length of the new segment from 0 to 1. The force response quickly becomes periodic. For the rest of the paper, we use the minimal model that only studies the first two pleating segments (see Figure 4.1c) to conduct parametric modeling. In this minimal model, as material enters the system, the length l_2 of the left segment continuously increases and serves as a continuation parameter.

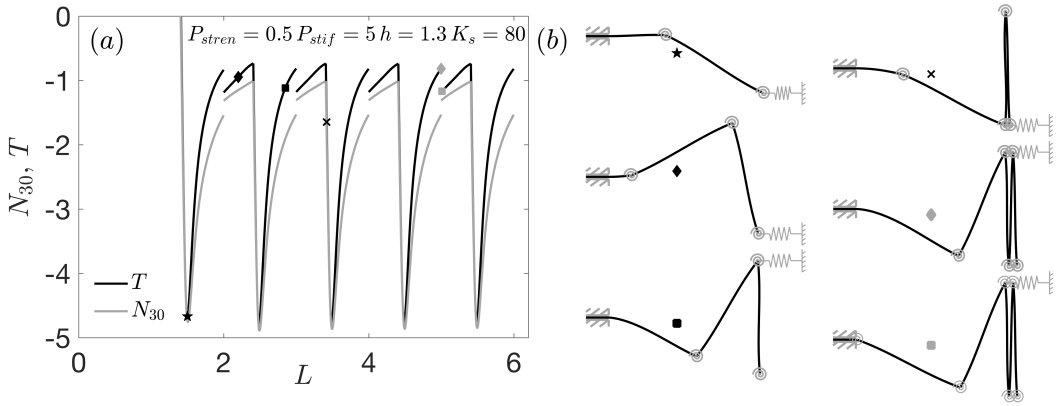

Figure 4.3: Rotary pleating results with $P_{stren} = 0.5, P_{stif} = 5, h = 1.3$, and $K_s = 80$. (a) The compressive force inside the sleeve (black) is amplified at the free side of the sleeve (gray). The jump/discontinuity at integer-lengths (i.e. $L = 2, 3, 4$ etc.) is caused by the insertion of pleats. (b) Shown are several pleating configurations from (a).

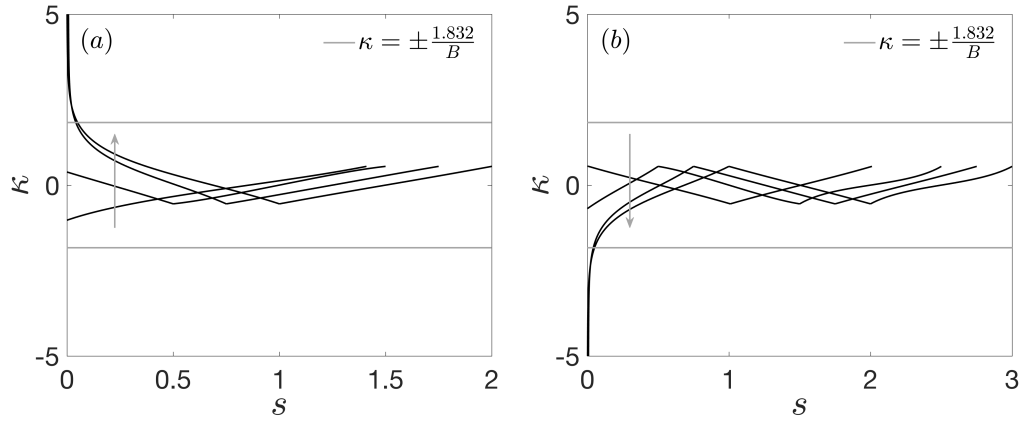

Figure 4.4: The evolution of curvature in the numerical pleating results from Figure 4.3. Arrows indicate the injection of material and the gray lines represent the curvature at 95% of the plateau moment A. (a) Inserting the second segment. The peak at the sleeve edge goes to as much as 14.4. (b) Inserting the third segment. The peak at the sleeve edge goes to as much as −15.8.

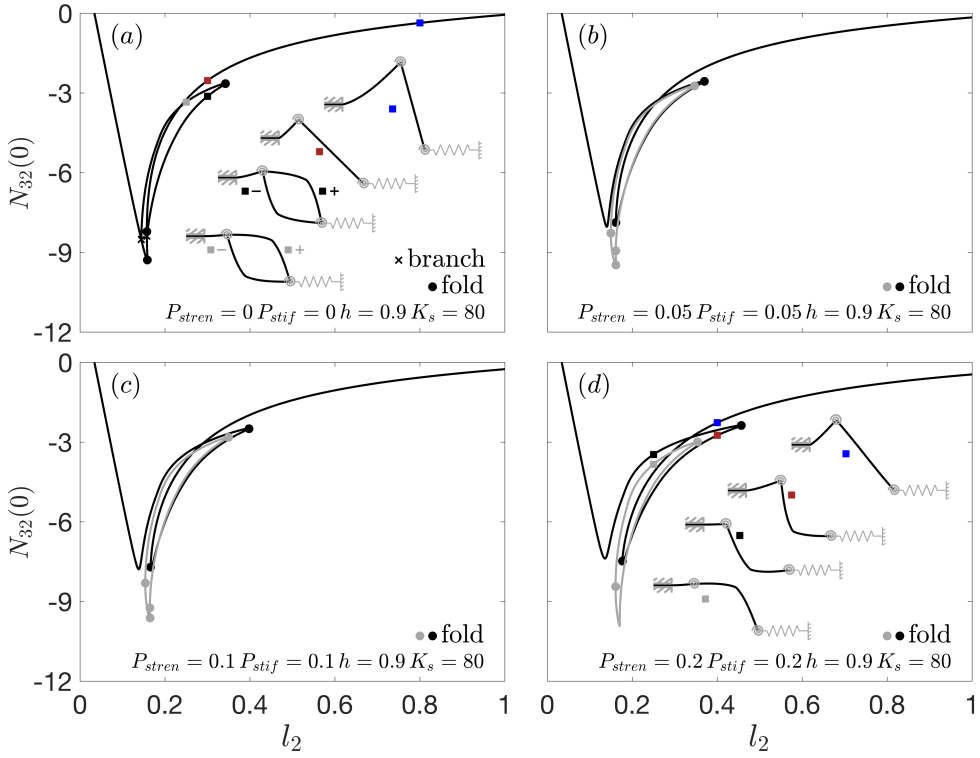

Figure 4.5: Rotary pleating results with $A = 1, B = 1, y_{P_1} = -0.5, h = 0.9, K_s = 80$, and different values of P_{stren} and P_{stif}. (a) With vanishing pleat strength, two additional solution branches with undesired localization connect with the main pleating curve through two branch points. (b)-(d) With increasing values of pleat strength and pleat stiffness, the two branch points are broken, causing one undesired branch to become an isolated loop and the other to connect with the main pleating curve.

Figure 4.4 shows the evolution of curvature in the numerical pleating results from Figure 4.3. The results suggest that large curvatures that tend to cause plastic deformations most likely occur at the sleeve edge, and the insertion of pleats can relieve the curvature localization. We assume that plastic deformations occur when the contact moment reaches 95% of the plateau moment A, i.e., $0.95A = A\tanh(B\kappa)$, leading to $\kappa = 1.832/B$.

Figure 4.5 shows numerical pleating results with a small horizontal space h of 0.9 and different pleat strengths P_{stren} and pleat stiffnesses P_{stif}. Unlike the successful pleating under a large value of h (see Figure 4.3), two additional branches that have an undesired localization/kink (see insets) in the first segment coexist with the main pleating curve. With zero pleat strength, the two branches coincide with each other and connect to the main pleating curve through two bifurcation points, which will lead to pleating failure. The pleating shapes on one loop have a kink pointing upward, while on the other loop it points downward. Increasing pleat strength and pleat stiffness breaks the bifurcation points and causes one branch to become an isolated loop and the other to stay connected to the main pleating curve. This also tends to lead to pleating failure because one undesired branch connects to the main pleating curve.

Figure 4.6 shows numerical pleating results with a slightly large horizontal space h of 0.94. With zero pleat strength, the two branches with undesired localization detach from the main pleating curve and exist as two coincident isolated loops. Increasing pleat strength and pleat stiffness causes one loop to connect to the main pleating curve and the other one to keep existing as an isolated loop. The results suggest that increasing pleat strength and pleat stiffness tend to lead to pleating failures.

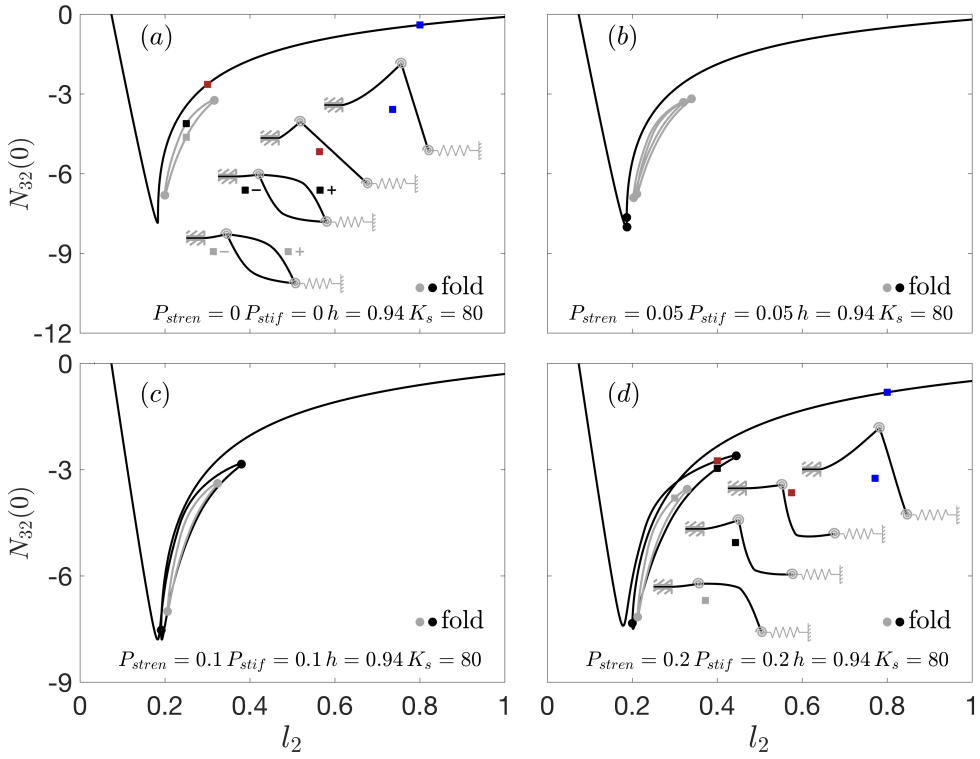

Figure 4.6: Rotary pleating results with $A = 1, B = 1, y_{P_1} = -0.5, h = 0.94, K_s = 80$, and different values of P_{stren} and P_{stif}. (a) With vanishing pleat strength, solution branches with undesired localizations exist as two coincident isolated loops. (b)-(d) With increasing values of pleat strength and pleat stiffness, one of the loops connects with the main pleating curve and the other exists as an isolated loop.

Figure 4.7 shows the distribution of angle θ and curvature κ of the pleating shapes in Figure 4.6a and Figure 4.6b. The discontinuity in θ is caused by the pleat, modeled as a discrete hinge, where the curvature is assumed to be continuous. At an undesired localization (a kink), θ changes abruptly, leading to a spike in curvature. In the correct pleating configuration, the right segment is almost straight, leading to a constant θ and an almost vanishing curvature.

In Figure 4.8, we gradually increase the horizontal space h while keeping the other parameters fixed to see how the pleating curves evolve. With a small h of 0.95 (see Figure 4.8a), one undesired branch connects with the main pleating curve and the other forms an isolated loop. With a slight increase of h to 0.98, the isolated loop becomes smaller, while the undesired branch previously connected to the main pleating curve detaches from it and becomes an isolated loop. A further increase of h to 1.01 makes the smaller loop disappear and the bigger loop smaller. Finally, all the undesired branches disappear with a h of 1.04, and the main pleating curve is the only solution left. We consider the results in Figure 4.8a to be bad pleating. Results in Figure 4.8b and 4.8c are slightly safer because the main pleating

curve is disconnected to the undesired solutions. However, pleating failure may still occur because in the real pleating process, dynamic effects and other unknown perturbations may push the correct configuration to nearby undesired shapes. We consider the pleating results in 4.8d to be good pleating, where the undesired solutions disappear and the main pleating curve is the only solution.

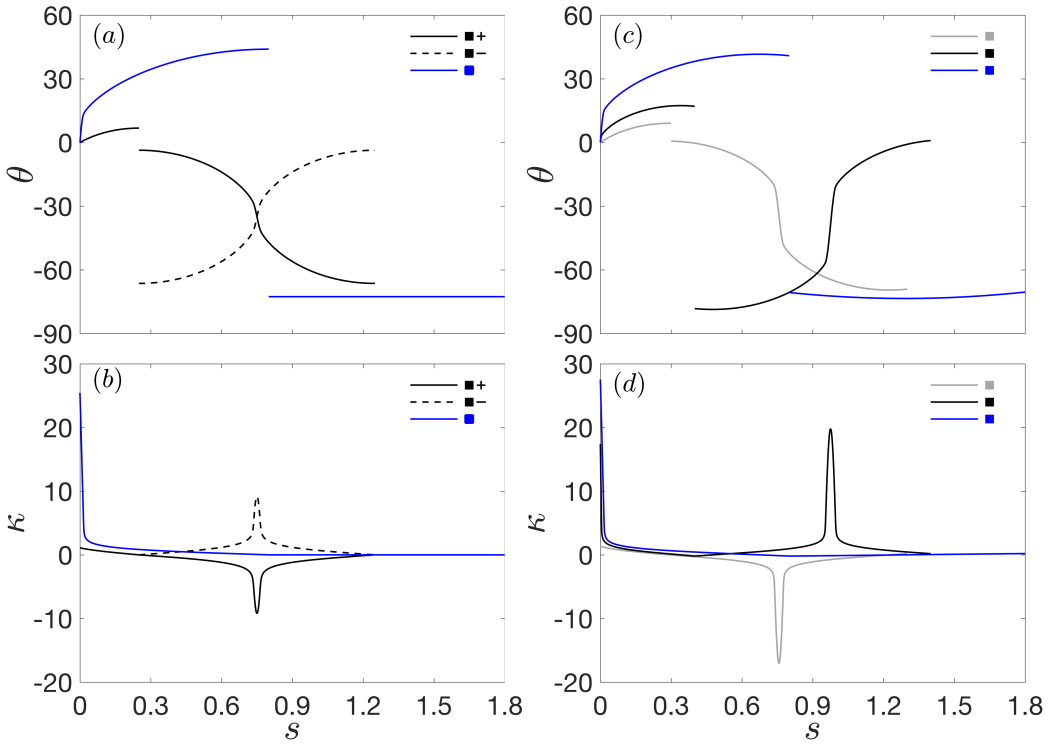

Figure 4.7: (a) Angle θ distribution of the insets in Figure 4.6a. The discontinuity occurs at the pleat. At a kink, θ changes abruptly. (b) Curvature κ distribution of the insets in Figure 4.6a. The undesired localization leads to a spike. Localization/plastic deformation also occurs at $s = 0$ (i.e., at the sleeve edge). (c) Angle θ distribution of the insets in Figure 4.6d. (d) Localization/plastic deformation also occurs at $s = 0$ (i.e., at the sleeve edge). Curvature κ distribution of the insets in Figure 4.6d.

The undesired solution loops disappear through the annihilation of two fold points, i.e., the loop becomes smaller and smaller and finally disappears. An efficient way to track the evolution of the undesired loop is to track the loci of the aforementioned fold points by varying processing and material parameters. Figure 4.9a shows the loci of the fold bifurcation in $h - l_2$ plane with different values of pleat strength. The two sets of curves, i.e., solid and dashed, correspond to the undesired branch that has a downward kink and an upward kink, respectively. At the peak point, two adjacent fold points annihilate each other, which destroys the loop solution. In Figure 4.9b, we plot a series of the peak points from Figure 4.9a in $h - P_{stren}$ plane. With smaller increments of P_{stren}, we can get a pleatability curve. Above

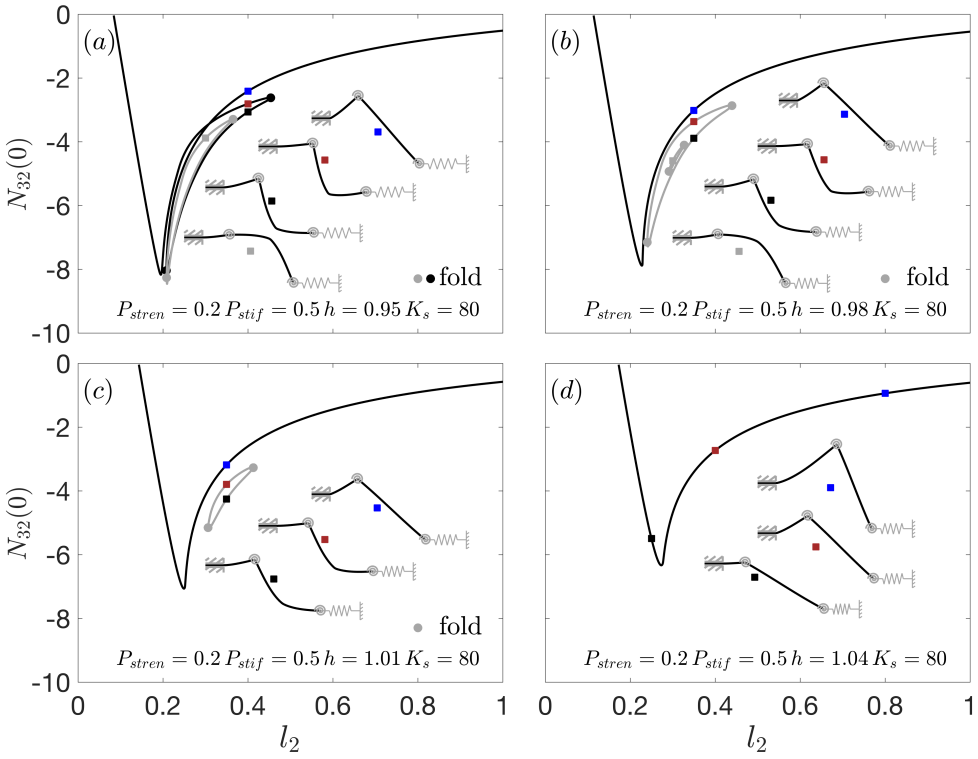

Figure 4.8: Rotary pleating results with $A = 1, B = 1, y_{P_1} = -0.5, K_s = 80, P_{stren} = 0.2, P_{stif} = 0.5$, and different values of h. (a) $h = 0.95$: One branch with a kink connects with the main branch, and the other exists as an isolated loop. (b) $h = 0.98$: The branch previously connected to the main pleating curve detaches from it, and the other isolated loop becomes smaller (c) $h = 1.01$: the bigger loop becomes smaller, and the smaller loop disappears. (d) $h = 1.04$: Both of the two loops disappear.

the pleatability curve, the undesired solution branches disappear and the pleating should be good.

By adding another axis like P_{stif} to Figure 4.9b, we get a series of pleatability curves that will make a pleatability surface. Our numerical results also suggest that plastic deformation or localization can occur at the sleeve edge (see Figure 4.4), which leads to another pleatability surface (by setting the plastic moment as $0.95A$).

Figure 4.10 shows such pleatability surfaces with a flexible pack. Below the pleatability surface, either solutions with undesired localizations exist or plastic deformation occurs at the sleeve edge. Both of them are considered pleating failure. With $B = 1$ (i.e., plastic/localization curvature $\kappa = 1.832$), the pleatability is controlled by the plastic deformation at the sleeve edge. Above the pleatability surface, rotary pleating should be good. Starting from a point below the pleatability surface, pleating failure can be avoided by either increasing the horizontal space h or decreasing the pleat strength or pleat stiffness.

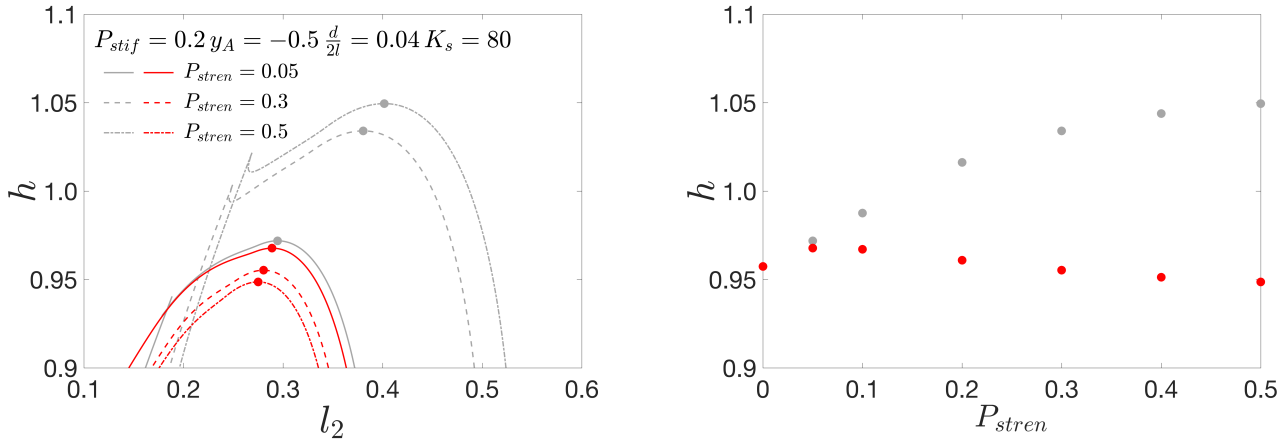

(a) (b)

Figure 4.9: (a) Loci of the fold bifurcation on the branch with a downward kink (gray) and on the branch with an upward kink (red) in the $h - l_2$ plane with different values of P_{stren}. At $P_{stren} = 0$, the two loci coincide. The peak "point" leads to the annihilation of fold bifurcations and thus kills the undesired loop solution. (b) A series of "peak points" in $P_{stren} - h$ plane: Gray (downward kink) and red (upward kink).

.

Figure 4.11 shows similar pleatability surfaces with a rigid pack, i.e., all the *constrained pleats* are moving at a constant speed of $v_p = \frac{d}{2l} v_m$. Here v_m is the inserting speed of the materials at the left sleeve edge. With a rigid pack, the pleatability surfaces are slightly elevated compared with a flexible pack. The measured horizontal space in Figure 4.1d is approximately 1.2 and is close to the upper limit of the pleatability surface predicted by our model.

Figure 4.12 shows another set of pleatability surfaces with a flexible pack and $B = 0.5$ (i.e., plastic/localization curvature $\kappa = 3.664$). The pleatability is controlled by the combination of plastic deformation at the sleeve edge and the undesired localization branch.

Figure 4.13 shows similar pleatability surfaces with a rigid pack and $B = 0.5$. Again, the pleatability is controlled by the combination of plastic deformation at the sleeve edge and the undesired localization branch.

Our results show that increasing h tends to destroy the undesired solution branches and relieve the strain at the sleeve edge. However, the maximal h is limited by the geometry of the rotary pleating, e.g., the number of *active pleats* cannot exceed three. A simple geometric analysis suggests that $h_{max} \approx \sqrt{2^2 - 0.5^2} \approx 1.94$. Our numerical simulations with $A = 1, B = 1, P_{stren} = 0.5, P_{stif} = 5$, and $K_s = 80$ suggest that when $h \geq 1.9$, the pleat cannot be correctly formed (see Figure 4.14).

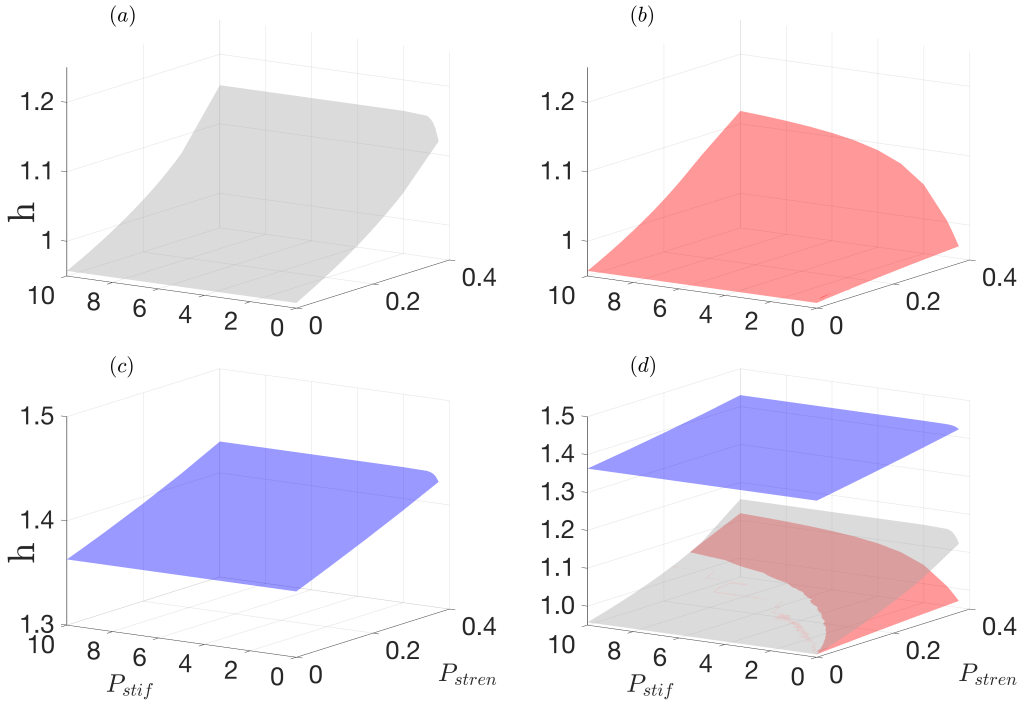

Figure 4.10: Pleatability surfaces in $h - P_{stren} - P_{stif}$ space with $A = 1, B = 1, \epsilon = 0.001, \frac{d}{2l} = 0.04, K_s = 80$, and $\frac{P_{stiff}}{P_{stren}} B \geq 1.166$. The surface has been (a) A pleatability surface associated with a downward kink. (b) A pleatability surface associated with an upward kink. (c) A pleatability surface associated with plastic deformation at the sleeve edge. (d) All pleatability surfaces are plotted together.

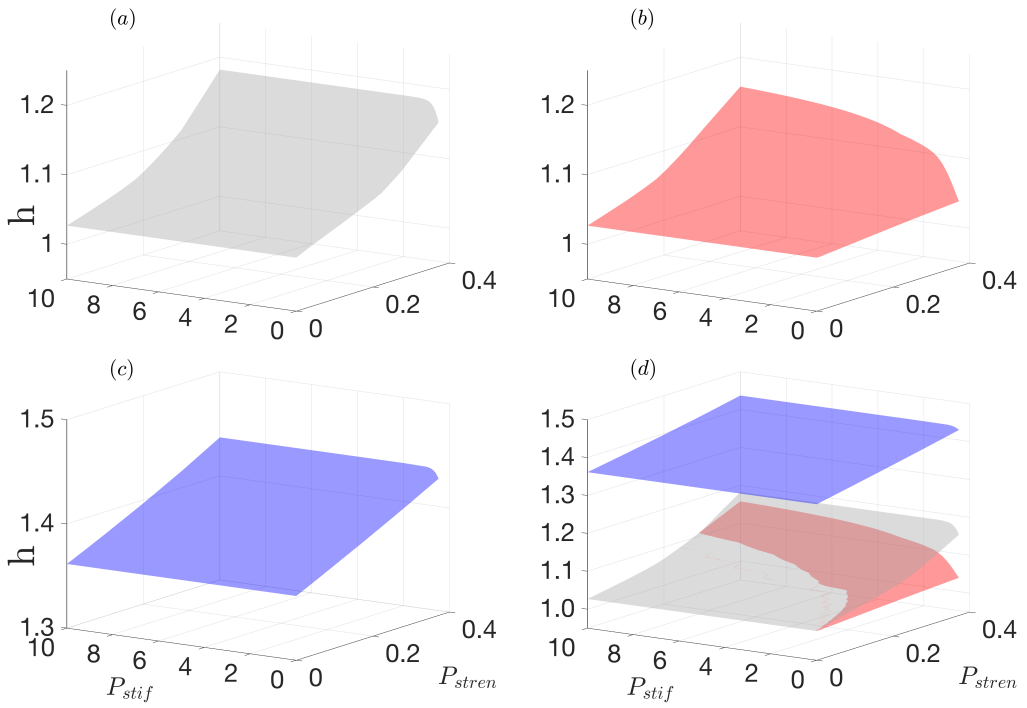

Figure 4.11: Pleatability surfaces in $h - P_{stren} - P_{stif}$ space with $A = 1, B = 1, \epsilon = 0.001, \frac{d}{2l} = 0.04, \frac{P_{stiff}}{P_{stren}} B \geq 1.166$, and a moving rigid pack. (a) A pleatability surface associated with a downward kink. (b) A pleatability surface associated with an upward kink. (c) A pleatability surface associated with plastic deformation at the sleeve edge. (d) All pleatability surfaces are plotted together.

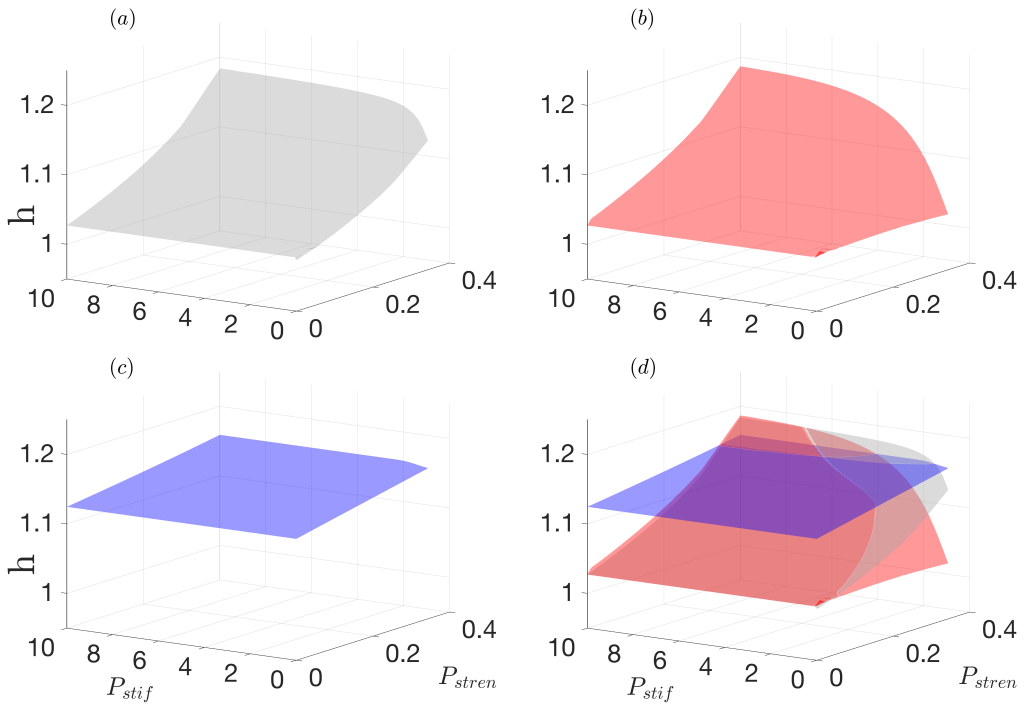

Figure 4.12: Pleatability surfaces in $h - P_{stren} - P_{stif}$ space with $A = 1, B = 0.5, \epsilon = 0.001, \frac{d}{2l} = 0.04, K_s = 80$, and $\frac{P_{stiff}}{P_{stren}} B \geq 1.166$. (a) A pleatability surface associated with a downward kink. (b) A pleatability surface associated with an upward kink. (c) A pleatability surface associated with plastic deformation at the sleeve edge. (d) All pleatability surfaces are plotted together.

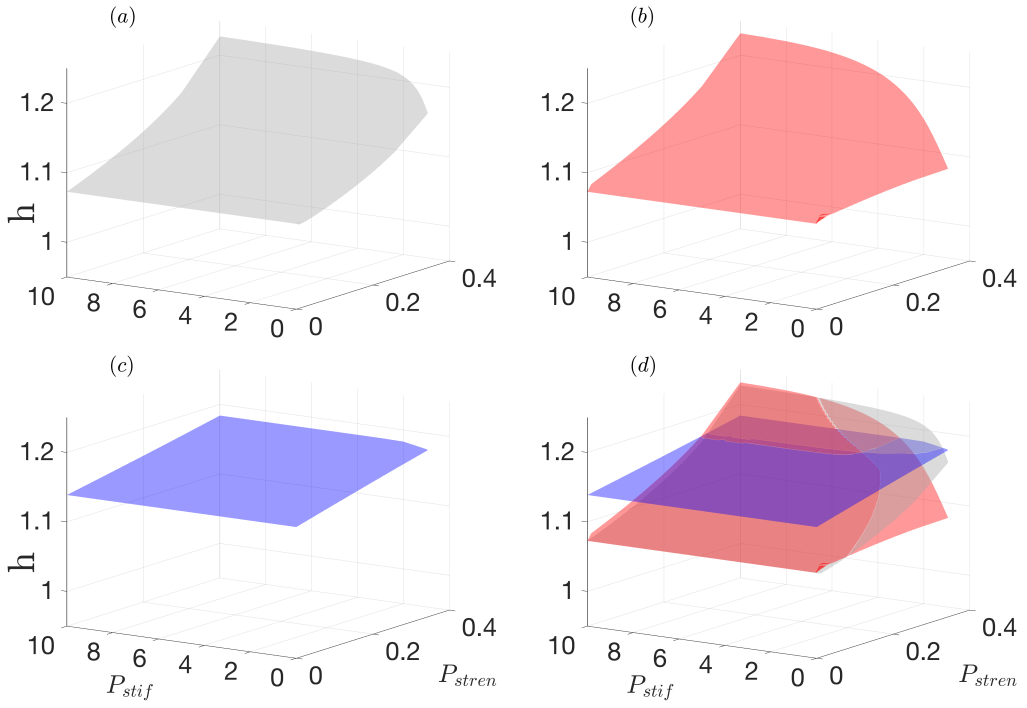

Figure 4.13: Pleatability surfaces in $h - P_{stren} - P_{stif}$ space with $A = 1, B = 0.5, \epsilon = 0.001$, $\frac{d}{2l} = 0.04$, $\frac{P_{stiff}}{P_{stren}} B \geq 1.166$, and a moving rigid pack. (a) A pleatability surface associated with a downward kink. (b) A pleatability surface associated with an upward kink. (c) A pleatability surface associated with plastic deformation at the sleeve edge. (d) All pleatability surfaces are plotted together.

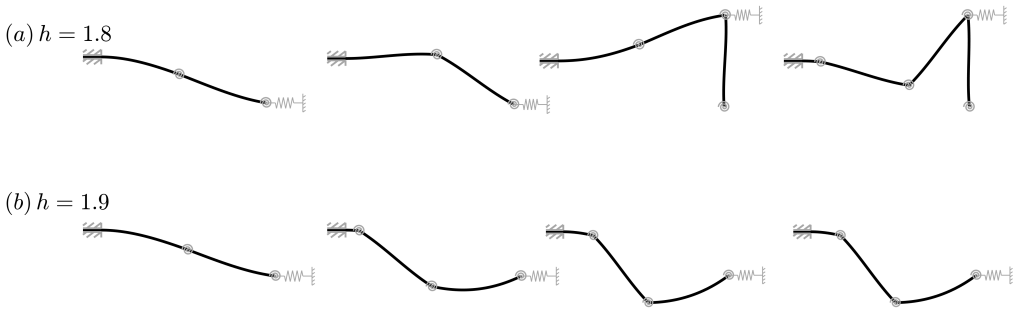

Figure 4.14: Pleating shapes with large values of h ($A = 1, B = 1, P_{stren} = 0.5, P_{stif} = 5, \epsilon = 0.001$, $\frac{d}{2l} = 0.04$, and $K_s = 80$). (a) h=1.8 (b) h=1.9: the pleat is not correctly formed. These configurations are not possible in the real pleating process because of constraints below (see Figure 4.1d).

4.5 Conclusion and further discussion

The current study only focuses on the mechanics of pleating and ignores other factors such as thermal processing that may also influence the pleating results. In addition, the constitutive laws (i.e., hyperbolic tangent functions) we have used for the materials and the pleats are *elastic*. However, plastic deformations may occur at the sleeve edge or at an undesired kink. Once the material enters the plastic regime, it will likely adopt a different unloading path that is not incorporated in our model. We have obtained a pleatability surface that prevents plastic deformations at the sleeve edge. Additionally, at an undesired kink, our numerical results imply that the unloading of the material from plastic deformations is possible (see Figures 4.5, 4.6, and 4.8). Our numerical results are not realistic once the kink starts unloading. Similar unloading is also observed in a real rotary pleating process [41]. The main focus of this work is on capturing the loci of the fold bifurcations on the undesired loop solutions, which generates several pleatability surfaces. The flexibility of the pleated pack is modeled as a simple linear spring inserted at the leftmost pleat inside the pack. In the real pleating process, there exists a transitional region where several pleating segments interact/contact with each other and contribute together to the flexibility [41].

In this work, we have only included the numerical pleating results that have pleat strength up to 0.4. With pleat strengths larger than 0.4, small pleat stiffness does not influence the pleating results too much, but large pleat stiffness leads to complicated solutions. For example, the undesired localization branches seem to exist in large values of horizontal space, even though the main pleating curve becomes clean. If we think of scoring (i.e., pre-weakening) as a process of reducing material thicknesses, half of the original thickness leads to a pleat strength of one-eighth of the original material, and 40% of the original material strength is caused by a pleat that has a thickness of 73.6% of the unweakened material. Also, for a real pleat, the pleat strength and pleat stiffness seem not to be independent parameters, and they should be related to each other through the scoring process.

We have developed a theoretical model to study the mechanical rotary pleating process and formulated it as a multi-point variable-arc-length boundary value problem (BVP). We used numerical continuation to solve the BVP and track the evolution of the solutions in terms of processing and material parameters including pleat stiffness, pleat strength, flexibility of the pleated pack, and the horizontal space between the sleeve edge and the pack. With a small value of the horizontal space, the solution branches with an undesired localization/kink are identified as isolated loops or connect to the main pleating curve even with vanishing pleat strength. Localization/plastic deformation could also occur at the sleeve edge. Other complicated/multiple localization branches may exist. In this study, we only focus on the localization at the sleeve edge and the undesired branches that have either an upward or a downward kink, which seem to be the most likely pleating failures.

Increasing horizontal space (or decreasing pleat strength and pleat stiffness) generally relieves the localization at the sleeve edge, disconnects the undesired solution loops from the main

pleating curve and can further destroy the undesired solution loops through the annihilation of fold bifurcations. However, the maximal horizontal space h is limited by the geometry of rotary pleating. We consider pleating results with undesired solutions connected to the main pleating curve or with localization/plastic deformation at the sleeve edge to be bad pleating. Additionally, pleating results with undesired isolated loops may also lead to pleating failures due to dynamic effects and other unknown perturbations in the real pleating process. The pleatability surfaces that identify which portions of the parameter space lead to successful pleating can potentially help the industry avoid pleating failures. Our theoretical model and implementation can be adapted to study other pleating processes (e.g., mechanical knife pleating [1]) and may also be useful to simulate growth of one dimensional slender structures.

Currently we don't have any stability information about the undesired localized branches. We guess that for the loop solution, one half is stable and the other half is unstable. It will be interesting to establish a stability criterion for this type of problem with sleeve boundary conditions, i.e., the motion of the material along the arc-length direction should also be considered when applying perturbations to an equilibrium.

4.6 Acknowledgments

This work was supported by The NonWovens Institute (project 16-197). We thank H. Singh for helpful discussions on sleeve boundary conditions.

Bibliography

[1] I. M. Hutten. *Handbook of nonwoven filter media*. Elsevier, 2007.

[2] Z. Y. Wei, Z. V. Guo, L. Dudte, H. Y. Liang, and L. Mahadevan. Geometric mechanics of periodic pleated origami. *Physical Review Letters*, 110(21):215501, 2013.

[3] M. A. Dias and C. D. Santangelo. The shape and mechanics of curved-fold origami structures. *Europhysics Letters*, 100(5):54005, 2012.

[4] Z. Marciniak, J. L. Duncan, and S. J. Hu. *Mechanics of sheet metal forming*. Butterworth-Heinemann, 2002.

[5] T. X. Yu and W. Johnson. The press-brake bending of rigid/linear work-hardening plates. *International Journal of Mechanical Sciences*, 23(5):307–318, 1981.

[6] A. Benusiglio, V. Mansard, A. L. Biance, and L. Bocquet. The anatomy of a crease, from folding to ironing. *Soft Matter*, 8(12):3342–3347, 2012.

[7] A. C. Abbott, P. R. Buskohl, J. J. Joo, G. W. Reich, and R. A. Vaia. Characterization of creases in polymers for adaptive origami structures. In *ASME 2014 Conference on Smart Materials, Adaptive Structures and Intelligent Systems, Newport, RI*, pages SMASIS2014–7480. American Society of Mechanical Engineers, 2014.

[8] C. Y. Wang. Folding of elastica-similarity solutions. *Journal of Applied Mechanics*, 48 (1):199–200, 1981.

[9] Y. Satou and H. Furuya. Mechanical properties of z-fold membrane under elasto-plastic deformation. *Journal of Space Engineering*, 4(1):14–26, 2011.

[10] B. Y. Dharmadasa, H. M. Y. C. Mallikarachchi, and F. Lopez Jimenez. Characterizing the mechanics of fold-lines in thin kapton membranes. In *2018 AIAA Spacecraft Structures Conference*, page 0450, 2018.

[11] Frederic Lechenault, Benjamin Thiria, and Mokhtar Adda-Bedia. Mechanical response of a creased sheet. *Physical Review Letters*, 112(24):244301, 2014.

[12] T. Jules, F. Lechenault, and M. Adda-Bedia. Local mechanical description of an elastic fold. *Soft Matter*, 15(7):1619–1626, 2019.

[13] Y. Satou and H. Furuya. Local buckling in crease induced by wrapping fold of space membrane. *Journal of Spacecraft and Rockets*, 51(2):595–603, 2014.

[14] Y. Satou and H. Furuya. Fold line based on mechanical properties of crease in wrapping fold membrane. In *54th AIAA/ASME/ASCE/AHS/ASC Structures, Structural Dynamics, and Materials Conference, Boston, MA*, page 1595, 2013.

[15] A. Papa and S. Pellegrino. Mechanics of systematically creased thin-film membrane structures. In *46th AIAA/ASME/ASCE/AHS/ASC Structures, Structural Dynamics and Materials Conference, Austin, Texas*, page 1975, 2005.

[16] DJS Newman and RJ Wootton. An approach to the mechanics of pleating in dragonfly wings. *Journal of Experimental Biology*, 125(1):361–372, 1986.

[17] C. J. C. Rees. Form and function in corrugated insect wings. *Nature*, 256(5514):200, 1975.

[18] H. Kobayashi, B. Kresling, and J. F. V. Vincent. The geometry of unfolding tree leaves. *Proc. R. Soc. B*, 265(1391):147–154, 1998.

[19] M. Brunet, F. Morestin, and S. Godereaux. Nonlinear kinematic hardening identification for anisotropic sheet metals with bending-unbending tests. *Journal of Engineering Materials and Technology*, 123(4):378–383, 2001.

[20] J. Carbonnière, S. Thuillier, F. Sabourin, M. Brunet, and P. Y. Manach. Comparison of the work hardening of metallic sheets in bending–unbending and simple shear. *International Journal of Mechanical Sciences*, 51(2):122–130, 2009.

[21] J. L. Duncan, S. C. Ding, and W. L. Jiang. Moment-curvature measurement in thin sheet–part I: equipment. *International Journal of Mechanical Sciences*, 41:249–260, 1999.

[22] J. L. Duncan, S. C. Ding, and W. L. Jiang. Moment-curvature measurement in thin sheet–part II: yielding and kinking in aged steel sheet. *International Journal of Mechanical Sciences*, 41:261–267, 1999.

[23] J. Mendiguren, A. Abvabi, B. Rolfe, and M. Weiss. Improvement of accuracy in a free bending test for material characterization. *International Journal of Mechanical Sciences*, 103:288–296, 2015.

[24] M. Weiss, H. Wolfkamp, B. F. Rolfe, P. D. Hodgson, and E. Hemmerich. Measurement of bending properties in strip for roll forming. *International Deep Drawing Research Group International Conference, Golden, CO*, pages 521–532, 2009.

[25] T. W. Murphey, M. E. Peterson, and M. M. Grigoriev. Large strain four-point bending of thin unidirectional composites. *Journal of Spacecraft and Rockets*, 52(3):882–895, 2015.

[26] J. M. Fernandez and T. W. Murphey. A simple test method for large deformation bending of thin high strain composite flexures. In *2018 AIAA Spacecraft Structures Conference. Kissimmee, Florida*, page 0942, 2018.

[27] T. Isshi. Bending tester for fibers, yarns and fabrics. *Journal of the Textile Machinery Society of Japan*, 3(2):48–52, 1957.

[28] T. Yu and J. Hanna. Exact and approximate mechanisms for pure bending of sheets. [arXiv:1905.07484].

[29] G. E. Sanford, E. V. Ardelean, T. W. Murphey, and M. M. Grigoriev. High strain test method for thin composite laminates. In *16th International Conference on Composite Structures. Porto, Portugal*, 2011.

[30] TAPPI 566 om-08. Bending resistance (stiffness) of paper (Taber-type tester in 0 to 10 Taber stiffness unit configuration). Standard, Technical Association of the Pulp and Paper Industry, Peachtree Corners, GA, 2008.

[31] D. Bigoni, F. Dal Corso, F. Bosi, and D. Misseroni. Eshelby-like forces acting on elastic structures: theoretical and experimental proof. *Mechanics of Materials*, 80:368–374, 2015.

[32] O. M. O'Reilly. Some perspectives on Eshelby-like forces in the elastica arm scale. *Proceedings of the Royal Society A*, 471(2174):20140785, 2015.

[33] J. A. Hanna, H. Singh, and E. G. Virga. Partial constraint singularities in elastic rods. *Journal of Elasticity*, 133(1):105–118, 2018.

[34] A. Liakou and E. Detournay. Constrained buckling of variable length elastica: Solution by geometrical segmentation. *International Journal of Non-Linear Mechanics*, 99:204–217, 2018.

[35] F. Bosi, D. Misseroni, F. Dal Corso, and D. Bigoni. An elastica arm scale. *Proceedings of the Royal Society A*, 470(2169):20140232, 2014.

[36] U. Ascher and R.D. Russell. Reformulation of boundary value problems into "standard" form. *SIAM Review*, 23(2):238–254, 1981.

[37] Y. Vetyukov, E. Oborin, J. Scheidl, M. Krommer, and C. Schmidrathner. Flexible belt hanging on two pulleys: contact problem at non-material kinematic description. *International Journal of Solids and Structures*, 168:183–193, 2019.

[38] L. Kong and R. G. Parker. Equilibrium and belt-pulley vibration coupling in serpentine belt drives. *J. Appl. Mech.*, 70(5):739–750, 2003.

[39] A. Lyckegaard and O. T. Thomsen. Nonlinear analysis of a curved sandwich beam joined with a straight sandwich beam. *Composites Part B: Engineering*, 37(2-3):101–107, 2005.

[40] E. J. Doedel, R. C. Paffenroth, A. R. Champneys, T. F. Fairgrieve, Y. A. Kuznetsov, B. E. Oldeman, B. Sandstede, and X. Wang. AUTO-07P: Continuation and bifurcation software for ordinary differential equations.
`indy.cs.concordia.ca/auto/` , 2007.

[41] Youtube video by Double Win Corporation Limited. For the video, see:
https://www.youtube.com/watch?v=V11FChu2bS8.

Chapter 5

Bistability of creased thin disks

The work presented in this chapter comes from an ongoing project studying bistability in creased thin sheets. The contents of this chapter have not been published yet.

Attribution

The work presented in this chapter was done in collaboration with J. A. Hanna, who contributed to the work through idea development, editing, and support.

Abstract

Creased thin sheets exhibit bistability, with a pressed-through state possessing a localized elastic singularity. We experimentally explore the loss of bistability upon excision of the singularity and a surrounding region of material, varying the thickness and hole geometry. We examine numerical solutions of an inextensible strip model, varying hole geometry, crease angle and stiffness, and other factors, and find reasonable qualitative agreement with experimental bistability boundaries. The strip model captures the critical hole size that destroys the bistability through a fold bifurcation. Our results shed new light on the mechanics of creases and singularities, and may guide the design of origami and kirigami.

5.1 Introduction

Creasing thin sheets is commonly seen in paper folding, deployable space structures, and sheet metal forming [1]. Conspiring with the flexibility of thin sheets, creases are able to

create new equilibria and thus novel bending degrees of freedom that extend the configuration space of rigid origami [2, 3, 4]. Curved creases employ bending deformations of thin sheets, leading to promising folded shapes [5, 6, 7]. Creases in thin sheets have generic bistability, with a pressed-through state possessing a localized singularity [8, 9, 10]. Elastic singularities in thin sheets can supply rigidity and interact with each other [11]. Truncating two ends of a stretching ridge relieves stress concentration through transforming the ridge from a conical surface to a cylindrical surface [12]. Upon excising the singularity of a creased strip through making a hole around the vertex, the force needed to invert the strip is reduced [9]. We find the bistability of creases will be lost if the hole is large enough. In this chapter, we study the critical hole size that destroys the bistability of creases.

It is the competition between the mechanics of creases and the flexibility of the facets that determines the shapes and other mechanical properties of creased thin structures. Various continuum models/theories have been developed and applied to study the mechanics of thin sheets. For example, Föppl-von Kármán theory [8], inextensible plate theory [13, 14, 15], and an inextensible strip model [6, 7, 16]. There have been other discrete models such as the truss and hinge model [17, 18, 19], triangular mesh model [20, 21], and the hinge and facet model [9]. Another important aspect for studying creased structures is to accurately understand the mechanics of creases, which have been studied by modeling the crease as a discrete hinge [22, 23] or a continuous structure [24, 25]. The *origami length* identified in a creased thin strip determines whether the deformation of the crease or the facets is dominant [22]. A similar *hinge index* is proposed to evaluate the "hinge-like" behavior of creases [26].

5.2 Geometry of the experiments and methods for stability test

We experimentally explore the loss of bistability in creased thin disks by excising the singularity and varying the hole geometry and material thickness. Other factors, such as crease stiffness, crease angle, and number of creases also influence bistable behaviors (see Figure 5.1). We are particularly interested in the dependence of the bistability on the size and shape of the hole. We observe that a finite circular hole leads to the loss of bistability, while a slit or an elliptical hole cut along the crease direction can be as large as the size of the disk and bistability still remains (Figure 5.1e). Interestingly, by excising an annular sector, the critical hole size is found to increase significantly (Figure 5.1c and Figure 5.1d). We define an angle deficit α, with $\alpha < 1$ corresponding to cutting off an annular sector, $\alpha > 1$ corresponding to inserting an annular sector, and $\alpha = 1$ corresponding to no cutting or insertion. The angle deficit also helps with numerical continuation of the inextensible strip model.

We use a Silhouette Cameo 3 cutting machine (Silhouette America, Lindon, UT) to cut samples of different thicknesses (0.005"/0.127 mm, 0.003"/0.076 mm, and 0.002"/0.051 mm) from thin polyester shim stock sheets (Artus Corp., Englewood, NJ). Creases are introduced

by a vise whose swivel is always rotated to the same position, trying to apply consistent pressure and thus achieve consistent crease angles. We refer to the stable equilibrium after creases are introduced as the *creased configuration* and to the stable configuration after being inverted as the *inverted configuration*. Between these two stable equilibria exists an unstable *energy barrier*.

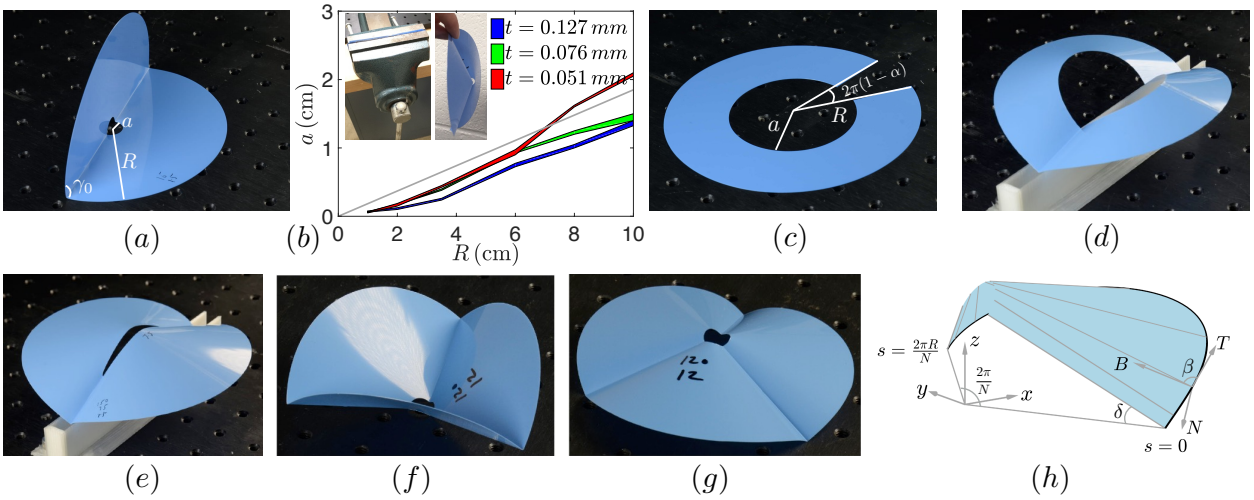

Figure 5.1: Folded cones made by thin shim stock under removal of elastic singularities. (a) Creased configuration with two radial creases, circular hole size a/R, and crease angle γ_0. (b) Critical hole size for three thicknesses of 0.127 mm (blue), 0.076 mm (green), and 0.051 mm (red). Each data point contains five samples. Upper boundaries of each band have a stability probability of 25%, and lower boundaries 75%. (c) By introducing an angle deficit $2\pi(1-\alpha)$ to the annulus, the hole size can be increased significantly, as shown in (d). (e) An inverted configuration with a narrow elliptic hole. (f) A creased configuration with three evenly distributed creases and a circular hole. (g) The inverted configuration obtained from (f). (h) A developable strip can be constructed with a family of straight generators. The generators make an angle β with the tangent. The outer circle is chosen as the directrix of the developable surface. $\boldsymbol{T}$ is the tangent to the baseline, $\boldsymbol{N}$ is the unit normal to the surface, and $\boldsymbol{B} = \boldsymbol{T} \times \boldsymbol{N}$.

After introducing the crease, we let the *creased configuration* relax for five minutes before manually inverting it to test the bistability. We hang the *inverted configuration* vertically to test its stability. Figure 5.1b shows stability bands of creased thin disks of different thicknesses with circular holes. Bistability is lost at a finite hole size that is much larger than the thickness of the material and much smaller than the size of the disk. The stability bands roughly follow the numerical prediction of an inextensible strip model (gray line). The agreement will likely become better as we increase the disk size, which can be explained qualitatively by the *origami length scale* [22]: the crease tends to behave rigidly with increasing size of the thin disk, leading to an asymptotic value of critical hole size that is proportional to the size of the disk.

5.3 An inextensible strip model

Because of the high energy costs in stretching thin objects, inextensibility is usually imposed everywhere on the surface of a thin strip [27]. We describe the thin disk as an inextensible annular strip that can be parametrized by a family of straight generators. Sadowsky [28] first derived a one-dimensional energy functional for an infinitesimal narrow inextensible strip. Later Wunderlich extended Sadowsky's functional to a strip with finite width [29]. Recently Starostin and van der Heijden derived Euler-Lagrange equations from Wunderlich's functional and constructed realistic shapes of developable Möbius strips [16]. Inextensible strip models are fraught with singular issues and are appropriate only when the edge of regression of the developable strip lives outside the material surface [30, 31]. However, when the geometry is free of singularities, inextensible strip models have been successfully applied to study various problems [32, 33].

Our description employs an orthonormal material frame $(\boldsymbol{T}, \boldsymbol{N}, \boldsymbol{B})$ [7] that is attached to the outer circle $\boldsymbol{r}(s)$ of the annulus (s is the arc length of $\boldsymbol{r}(s)$). The three directors correspond to the tangent $\boldsymbol{T}$ of $\boldsymbol{r}(s)$, normal $\boldsymbol{N}$ of the surface, and $\boldsymbol{B} = \boldsymbol{T} \times \boldsymbol{N}$, respectively. Figure 5.1h shows such a frame. During the isometric deformation, geodesic curvature on the outer circle $\boldsymbol{r}(s)$ must be preserved [27]. Motion of the material frame can be written as $\boldsymbol{T}' = \kappa_n \boldsymbol{N} - \kappa_g \boldsymbol{B}$, $\boldsymbol{N}' = -\kappa_n \boldsymbol{T} + \tau_g \boldsymbol{B}$, $\boldsymbol{B}' = \kappa_g \boldsymbol{T} - \tau_g \boldsymbol{N}$. Here, κ_n, κ_g and τ_g are the normal curvature, geodesic curvature and geodesic torsion of $\boldsymbol{r}(s)$, respectively. $(\tau_g \boldsymbol{T} + \kappa_g \boldsymbol{N} + \kappa_n \boldsymbol{B})$ is the Darboux vector. In our formulation, κ_g is negative. Because of the symmetry, we only need to study one piece of the creased disk that can be parameterized as

$$\begin{aligned} \boldsymbol{X}(s, v) &= \boldsymbol{r}(s) + v[\boldsymbol{B}(s) + \eta(s)\boldsymbol{T}(s)], \\ \eta(s) = \tau_g/\kappa_n = \cot\beta, s \in [0, \tfrac{2\pi R}{N}\alpha], v \in [0, V], \chi(V(s,\eta), s, \eta) &= 0, \end{aligned} \tag{5.1}$$

where $(\boldsymbol{B} + \eta \boldsymbol{T})$ aligns with the generators, which make an angle β with the tangent direction of the curve $\boldsymbol{r}(s)$. N is the number of evenly distributed creases, α is the angle deficit, and R is the radius of the outer circle $\boldsymbol{r}(s)$. v is the coordinate along the generator and $V\sqrt{1+\eta^2}$ represents the length of the generator. The mean curvature of the developable surface $\boldsymbol{X}(s, v)$ can be written as $H = \frac{\kappa_n(1+\eta^2)}{2[1+v[\eta' + \kappa_g(1+\eta^2)]]}$, and a differential area element is $dA = [1 + v(\eta' + \kappa_g(1+\eta^2))]\, ds dv$. We assume *a lengthwise constant crease angle* and per-unit-length moment generated by the crease $K_c \sin(\Gamma - \gamma_0)$. Here, γ_0 is the rest angle of the crease, and Γ is the deformed crease angle. The total elastic energy of a creased thin disk can be written as

$$\begin{aligned} U &= N\left[\frac{D}{2}\int_0^{\frac{2\pi R}{N}\alpha}\int_0^{V(s,\eta)} (2H)^2\, dA + K_c(R-a)\int_{\gamma_0}^{\gamma_f} \sin(\Gamma - \gamma_0) d\Gamma\right], \\ &= DN\left[\int_0^{\frac{2\pi R}{N}\alpha} g(\kappa, \eta, \eta', s) ds + \frac{K_c R}{D}(1 - \frac{a}{R})(1 - \cos(\gamma_f - \gamma_0))\right], \end{aligned} \tag{5.2}$$

where $g(\kappa_n, \eta, \eta', s) = Y(\kappa_n, \eta, \eta')W(\eta', \eta, s)$, $Y = \frac{\kappa_n^2(1+\eta^2)^2}{2[\eta'+\kappa_g(1+\eta^2)]}$, and $W = \ln[1 + V(s, \eta)(\eta' + \kappa_g(1 + \eta^2))]$. $D = Et^3/[12(1 - \nu^2)]$ is the per-unit-length bending rigidity, ν is Poisson's ratio, E is Young's modulus, t is the thickness, and a is the radius of a circular hole. *We assume that the crease angle in the inverted configuration is constant along the crease.* D/K_c is identified as an *origami length scale* [22], and is approximately $200t$ for thin mylar sheets. For a really thin disk (i.e., $t \to 0$) with a finite size of R, K_cR/D approaches infinity, which makes a rigid crease. The crease energy in Equation 5.2 drops out as boundary conditions and does not enter the bulk equations. Euler-Lagrange equations of 5.2 can be written as [16, 34]

$$\begin{aligned} \boldsymbol{F}' + \boldsymbol{w} \times \boldsymbol{F} = \boldsymbol{0}\,, \boldsymbol{M}' + \boldsymbol{w} \times \boldsymbol{M} + \boldsymbol{T} \times \boldsymbol{F} = \boldsymbol{0}\,, \\ \partial_{\kappa_n} g - \eta M_1 - M_3 = 0\,, \partial_\eta g - (\partial_{\eta'} g)' - \kappa_n M_1 = 0\,. \end{aligned} \tag{5.3}$$

The first two equations represent force and moment balances, and the last two equations contain constitutive information. Forces $\boldsymbol{F}$ and moments $\boldsymbol{M}$ can be resolved on the moving frame as $\boldsymbol{F} = F_1\boldsymbol{T} + F_2\boldsymbol{N} + F_3\boldsymbol{B}$ and $\boldsymbol{M} = M_1\boldsymbol{T} + M_2\boldsymbol{N} + M_3\boldsymbol{B}$. All forces and moments are normalized by D. In the absence of external force, $\boldsymbol{F}$ should be a constant vector, which further vanishes due to the rotational symmetry in the creased disk. *Surprisingly, the creased disk is under pure bending.* From Equation 5.3, together with an Euler angle description of the moving frame $(\boldsymbol{T}, \boldsymbol{N}, \boldsymbol{B})$ and the boundary conditions imposed at the two creased ends, we get a two-point boundary value problem (see Appendix C.1).

With circular holes, V in equation 5.1 can be solved explicitly in terms of η [34]. However, for holes with general shapes, V may also depend on arc-length s and may not be solved as an explicit function of η and s. Instead of trying to solve for V, we use an implicit function $\chi(V(s\,, \eta)\,, s\,, \eta) = 0$ to describe V. We treat V as an independent variable and turn the algebraic constraint $\chi = 0$ into a differential equation by differentiating it with respect to s. We have $\dfrac{\mathrm{d}V}{\mathrm{d}s} = V_s + V_\eta\eta'$, where V_s and V_η can be derived through implicit differentiation, i.e. $V_s = -\chi_s/\chi_V$ and $V_\eta = -\chi_\eta/\chi_V$. The lost constant in the differentiation process is kept by adding a boundary condition, i.e. $\chi(V(0), 0, \eta(0)) = 0$.

5.4 Numerical results of circular holes

We use the continuation package AUTO 07P [35] to solve the two-point boundary value problem. Several continuations are successively conducted to deform a conical frustum to match with the crease boundary conditions, through which the hole size a/R, crease angle γ_0, crease stiffness K_c, and angle deficit α are included as continuation parameters (see Appendix C.1). In AUTO 07P, the length of the integral interval is always normalized to 1. In numerical simulations, *we fix the radius of the thin disk R to 1 by introducing a scaling factor $2\pi\alpha/N$ to the boundary value problem.*

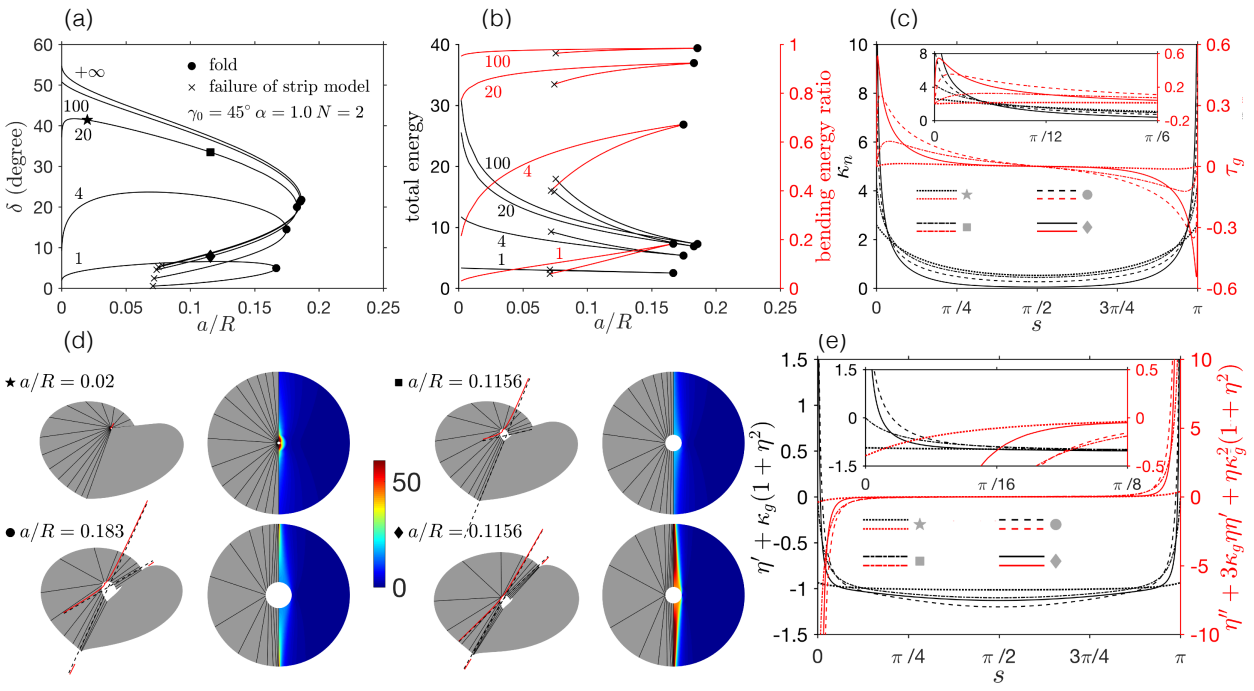

Figure 5.2: Numerical solutions of the inextensible strip model with circular holes. All data are presented with $\gamma_0 = 45°, \alpha = 1.0$ and $N = 2$. R is set to 1 for renderings. Solutions are plotted in different measures: (a) Cone strength with several crease stiffnesses K_cR/D; (b) Total elastic energy and ratio of facet bending energy. (c) Normal curvature and geodesic torsion on the baseline of several equilibria at $K_cR/D = 20$. (d) Several equilibria with generators (black) and the edge of regression (red) at $K_cR/D = 20$ are shown in both deformed and rest configurations. Color maps represent bending energy density on a half disk. Insets show the shape of the edge of regression. (e) Cylindrical and conical points correspond to zeros of the two functions.

For a circular hole, we have $\chi(V,\eta) = V^2 + (R^2 - 2VR - a^2)\sin^2\beta$, where $\cot\beta = \eta$. Figure 5.2 shows numerical solutions with $\gamma_0 = 45°, \alpha = 1.0, N = 2$ and various values of dimensionless crease stiffness K_cR/D. In all solution curves, the hole size is always bounded by a fold bifurcation, representing the loss of bistability. On the lower branch that represents the unstable energy barrier, the strip model breaks down because the edge of regression contacts the material surface, forming a conical structure that leads to divergence of bending energy. Beyond this point, stretching must be introduced to relieve local stress focusing. Similar conical structures bound the maximal width of a developable Möbius band [16], and are observed in displacing one end of a buckled strip laterally [31]. For strong creases (i.e., large values of K_cR/D), the crease energy is relatively small and the main deformation comes from bending of the facets. On the contrary, with a weak crease, the main deformation comes from the opening of the crease. As $K_cR/D \to \infty$, the solution approaches an asymptotic curve.

Figures 5.2d and 5.2c show several renderings of deformed and planar configurations, as well as distributions of κ_n and τ_g, respectively. Starting from a small hole and by continuously increasing its size, the edge of regression at the crease moves from one side to the other side of $\boldsymbol{r}$, indicating a critical hole size at which the crease becomes a cylindrical point with constant curvature along the crease. At $K_c R/D = 20$, the crease makes a cylindrical point at $a/R \approx 0.1156$. This transformation indicates that the internal end of the crease tends to open more when the hole is small ($0 < a/R < 0.1156$), and vice versa, the external end opens more with a bigger hole ($0.1156 < a/R$), because the bending moment is inversely proportional to the distance between a point on a generator and the edge of regression. With a small enough hole, the edge of regression approaches a point corresponding to the vertex of the cone. These numerical predictions qualitatively agree with experimental observations in which the crease angle is observed to be nonconstant. For the equilibrium on the unstable branch, the edge of regression always lies outside $\boldsymbol{r}$ at the crease, indicating that the external end of the crease should open more.

5.5 Numerical results of elliptic holes

With elliptic holes, χ can be written as $\chi(s,\eta,V(s,\eta)) = a^2(V^2 + (R^2 - 2VR)\sin^2\beta) + (b^2-a^2)(\cos^2\lambda(V^2+(R^2-2VR)\sin^2\beta) - \cos 2\lambda(R-V)^2\sin^2\beta + \sin 2\lambda(R-V)V\sin\beta\cos\beta) - a^2b^2\sin^2\beta$, where a and b are the two axes of the elliptic hole with b aligned with the crease direction. The arc-length coordinate s enters the problem through $\lambda = s/R$, leading to a "nonautonomous" boundary value problem. We transform the nonautonomous system to be "autonomous" by adding a trival differential equation $s' = 1$ and an additional boundary condition $s(0) = 0$. Numerical results with elliptic holes are summarized in Figure 5.3. We calculate a stability boundary (i.e., loci of the folds) in the space of the two elliptic axes with various crease stiffness. The area on the left of the boundary corresponds to the bistable region. On the stability curve, the size of a/R is bounded by a fold, creating a small region in which both increasing and decreasing the size of b/R lead to instability. In this region, b/R must be larger than certain values to maintain bistability. We test these surprising numerical results with two thicknesses of shim stock (see 5.3a). In experiments, we fix a/R at various values and vary b/R incrementally. The two sets of data both exhibit a fold structure that qualitatively agrees with numerical predications. The fold structure corresponds to isola-center bifurcations shown in Figure (5.3b), in which we fix a/R at various values and vary b/R.

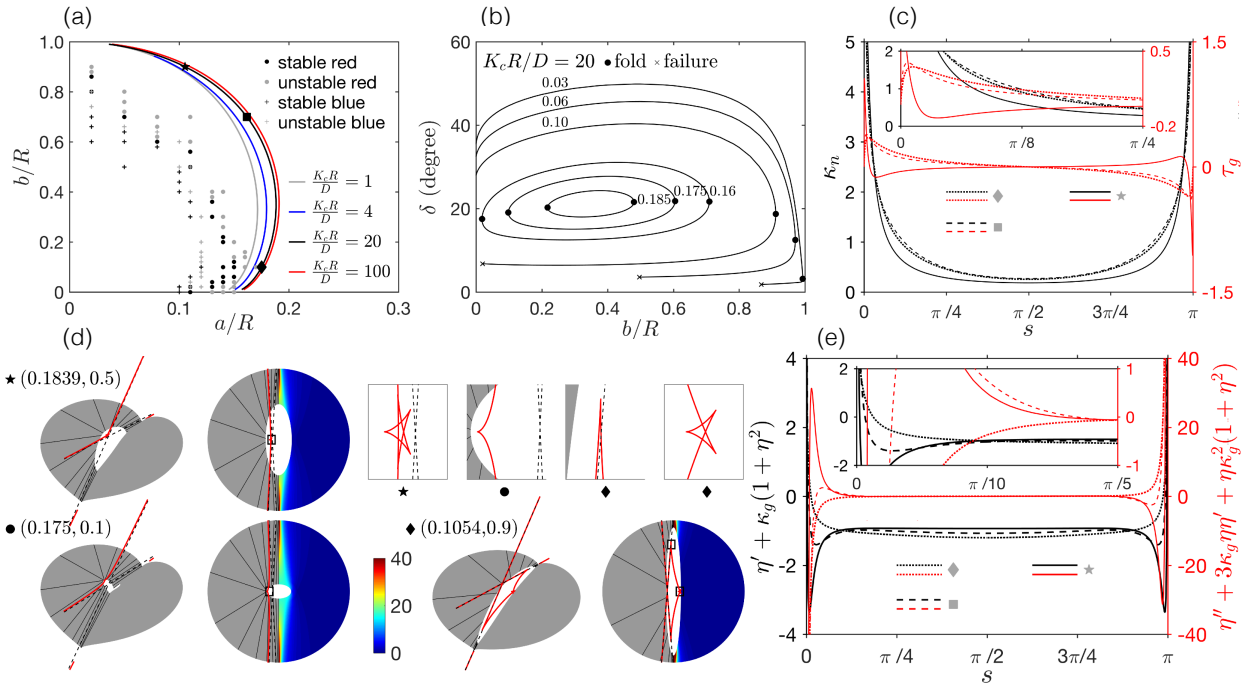

Figure 5.3: Numerical solutions of the inextensible strip model with elliptic holes. All data are presented with $\gamma_0 = 45°, \alpha = 1.0$ and $N = 2$. R is set to 1 for renderings. (a) Loci of the fold in the space spanned by the the two elliptic axes b/R (aligned with the crease) and a/R, with various crease stiffnesses K_cR/D. Shown also are two sets of experimental data. (b) Solutions by varying b/R for different values of a/R. In all curves, the upper branch is stable. In most values of a/R, only increasing b/R leads to a fold bifurcation. In a narrow regime of a/R created by the fold in (a), both increasing and decreasing b/R lead to a fold, and the two folds close the curve. (c) Normal curvature and geodesic torsion on the baseline of several equilibria at $K_cR/D = 20$. (d) Several equilibria from the stability boundary in (a) at $K_cR/D = 20$ are shown in both deformed and rest configurations. Color maps represent bending energy density. Insets show the shape of the edge of regression. (e) Cylindrical and conical points correspond to zeros of the two functions.

5.6 Loci of the fold bifurcations with circular holes

The relationship between the critical hole size and other parameters such as the crease angle, the number of evenly distributed creases, and the angle deficit can be better understood by tracing the loci of the fold bifurcation of the inextensible strip equations in various parameter spaces. Shown in Figure 5.4 is the relationship between the number of evenly distributed creases and the critical hole size. Figure 5.4a shows the variation of the critical hole size a/R with an increasing number of evenly distributed creases under different values of crease stiffness K_cR/D and angle deficit α. The series of fold bifurcations follows a check-mark shape. By decreasing α, a smaller value of K_cR/D tends to lead to a larger critical hole size, which matches with the numerical results showing that a bigger crease angle leads to a larger critical hole size with $\alpha < 1$. With $N = 1$, $K_cR/D = 20$, $\alpha = 1$ and $\gamma_0 = 45°$, the hole size can be as large as the size of a thin disk and bistability is kept. Figure 5.4b shows the solution curves in the plane of the hole size a/R and the cone strength δ. Shown also are the solution curves of the *creased configurations* with $N = 3$ and $N = 4$. Note that in a large number of creases, asymmetric modes may exist in experiments, which we don't take into account here.

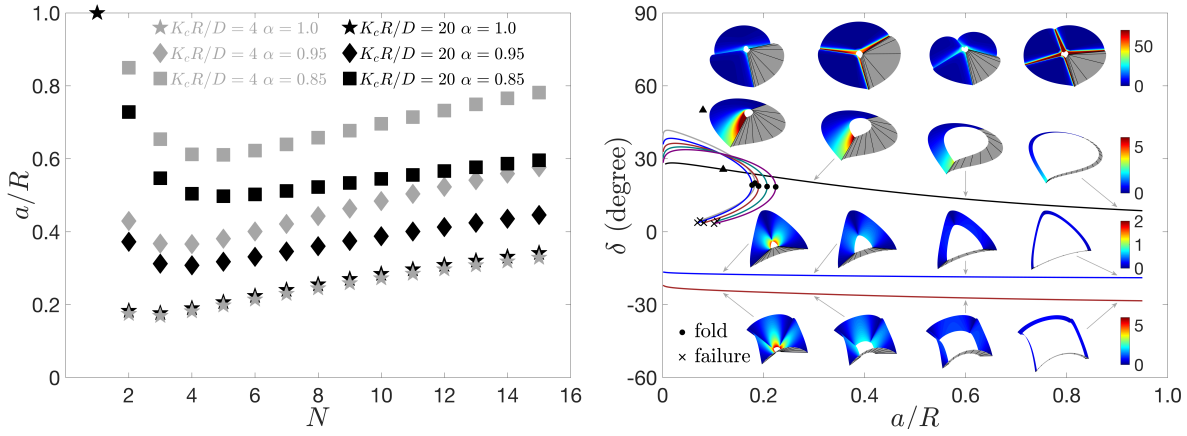

Figure 5.4: (a) Loci of the fold bifurcation for the inextensible strip model in the plane spanned by the number N of evenly distributed creases and the critical hole size a/R with different values of angle deficit α and dimensionless crease stiffness K_cR/D. (b) Solution curves with $K_cR/D = 20$; $\alpha = 1.0$; N=1(black), N=2(gray), N=3(blue), N=4(brown), N=5(green), N=6(purple). The renderings in the top row have a hole size $a/R = 0.12$ and contain the stable inverted configurations (i.e., the first and third ones, from left to right.) and the unstable energy barriers for $N = 3$ and $N = 4$. Solution curves above $\delta = 0$ represent the stable inverted configuration (upper branch) and the unstable energy barrier (lower branch); For $N = 1$, the critical hole size can be arbitrarily large. Solution curves below $\delta = 0$ represent creased configurations.

Shown in Figure 5.5 is the relationship between the angle deficit α and the critical hole size a/R. Figure 5.5a shows the loci of the fold bifurcation in the plane spanned by α and the critical hole size a/R with different dimensionless crease stiffnesses K_cR/D. We identify an upper and a lower boundary, and the area between them corresponds to the bistable regime. Both increasing and decreasing α may lead to instability; the former connects to the aforementioned unstable energy barrier, and the latter connects to another flipped unstable configuration. By varying α, several solution curves are also shown in Figure 5.5a . Figure 5.5b shows the solution curves in the plane of the circular hole size a/R and cone strength δ. Decreasing α generally leads to bigger critical hole size. With small values of K_cR/D and α, decreasing a/R also leads to instability, corresponding to the fact that the crease is not strong enough to hold the stable configuration, so the structure flips.

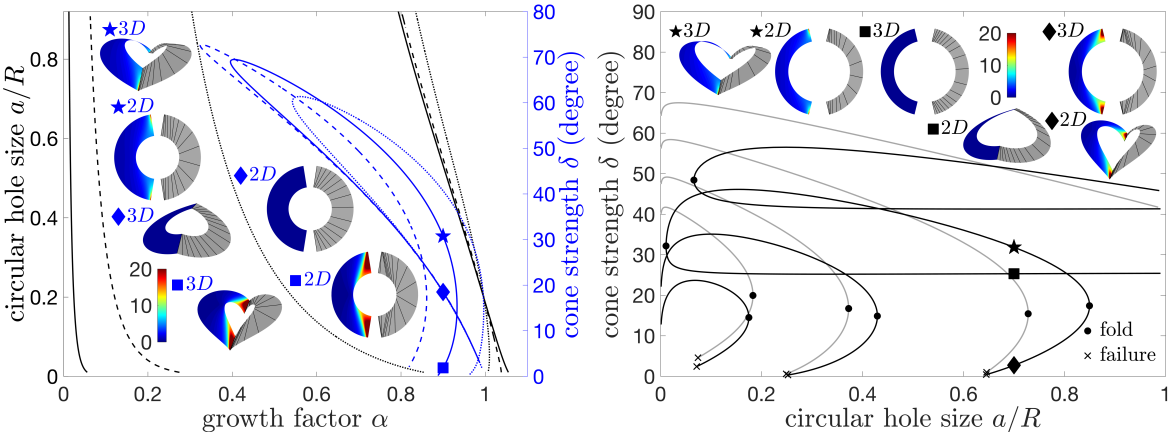

Figure 5.5: (a) Black curves show loci of the fold bifurcation for the inextensible strip model in the plane spanned by the angle deficit α and the critical circular hole size a/R at $\gamma_0 = 45°$, $N = 2$, $K_cR/D = 4$(dotted), $K_cR/D = 20$(dashed), and $K_cR/D = 100$(solid). The area enclosed by the left and the right boundary corresponds to the bistable region. Blue curves show solutions with $K_cR/D = 4$, $\gamma_0 = 45°$, $N = 2$, $a/R = 0.2$ (dotted), $a/R = 0.5$ (solid), and $a/R = 0.8$ (dashed). Both increasing and decreasing α lead to fold bifurcations. The upper branch is stable. Three equilibria that have exactly the same parameters are plotted in the deformed configuration and mapped back onto the flat configuration. (b) Solution curves with $K_cR/D = 4$ (solid) and $K_cR/D = 20$ (dashed); $\alpha = 1$ (gray), $\alpha = 0.95$ (blue), $\alpha = 0.85$ (black) and $\alpha = 0.70$ (purple).

Figure 5.6 shows the relationship between the rest crease angle γ_0 and the critical hole size a/R. Figure 5.6a shows the loci of the fold bifurcation in the plane spanned by γ_0 and the critical hole size a/R with different values of α. The area below the stability boundary corresponds to the bistable region. With $\alpha < 1$, decreasing γ_0 leads to instability, while with $\alpha \geq 1$, increasing γ_0 leads to instability. Figure 5.6b shows the solution curves in the plane of the rest crease angle γ_0 and the cone strength δ. With $\alpha \geq 1$, increasing γ_0 leads to instability, while $\alpha < 1$, decreasing γ_0 leads to instability.

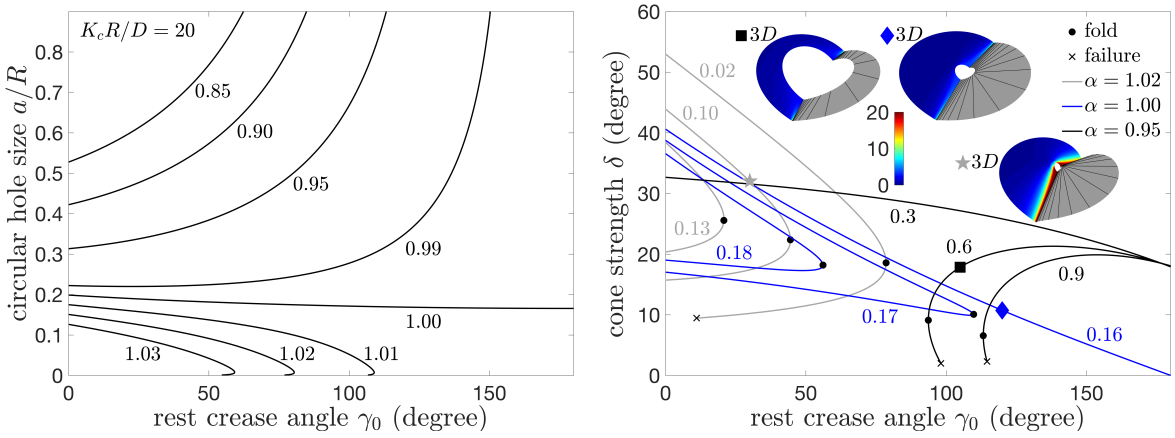

(a) (b)

Figure 5.6: All data are presented with $N = 2$ and $K_cR/D = 20$. (a) Loci of the fold bifurcation for the inextensible strip model in the plane spanned by the rest angle γ_0 and the critical hole size a/R with different values of α shown beside each curve. The area below the boundary corresponds to the bistable region. (b) Solution curves in the plane spanned by the rest crease angle γ_0 and cone strength δ, with different values of α and hole size a/R shown beside each curve.

5.7 Further discussion

We have presented experimental and numerical results on the bistability of creased thin disks under removal of singularities. The experiments suggest that the critical hole size depends on the material thickness and seems to follow the *origami length scale* [22]. This implies that with thin enough or large enough sheets, the crease tends to become rigid and the critical hole size will be proportional to the disk size. Material thickness is an interesting factor worth further exploration. We have also explored a stability boundary with elliptical holes in the plane spanned by the two elliptic axes. We found for a narrow elliptic hole with the long axis aligned with the crease direction (of which the limit corresponds to a slit), the long axis can be as large as the size of the disk and bistability remains. However, the other axis is bounded to a finite size and in a certain interval of it, both increasing and decreasing the axis along the crease direction can destroy the bistability.

The inextensible strip model captures the critical hole size as a fold bifurcation connected to a branch representing the (unstable) energy barrier. The numerical stability boundary of elliptic holes agrees with our experimental observations that a slit or a narrow elliptic hole can be as large as the thin disk, and is further bounded by a fold in the axis perpendicular to the crease direction. This fold leads to an isola center bifurcation in the solution space. With a circular hole, we have also quantified the influences of other factors such as the crease angle and number of creases on the bistability. Particularly, numerical results suggest that by cutting off an annular sector, the critical hole size can be increased significantly, which

can be easily verified (see Figure 5.1d).

The major challenge of the experiments is to control the crease angle. We observed quantitative inconsistency of the crease angle even though we tried to apply a consistent creasing procedure. Annealing the crease in a mold with fixed angle seems to be a promising technique [24]. It is interesting that our numerical results suggest that the critical hole size is not sensitive to the crease angle with $\alpha = 1.0$ (see Figure 5.6a), i.e., without inserting or cutting off any annular sector. This could probably also be seen from Figure 5.2a, where the critical hole size seems not to change too much within a large range of crease stiffnesses. With elliptical holes, the two facets in the inverted configuration may come in contact with each other if we push either of the elliptic axes to be very small, leading to a slit. Even though we assume a lengthwise constant crease angle, both our numerical and experimental results imply interesting lengthwise variations of the crease angle, depending on the hole size. Further studies could incorporate a non-constant crease angle into the inextensible strip model, likely causing generators to intersect with the crease [6].

Acknowledgments

This work was partially supported by the National Science Foundation under grant CMMI-1902444. We thank Tom Witten for helpful discussions.

Bibliography

[1] J. Hu, Z. Marciniak, and J. Duncan. *Mechanics of sheet metal forming*. Elsevier, 2002.

[2] J. L. Silverberg, J.H. Na, A. A. Evans, B. Liu, T. C. Hull, C. D. Santangelo, R. J. Lang, R. C. Hayward, and I. Cohen. Origami structures with a critical transition to bistability arising from hidden degrees of freedom. *Nature Materials*, 14(4):389–393, 2015.

[3] J. L. Silverberg, A. A. Evans, L. McLeod, R. C. Hayward, T. Hull, C. D. Santangelo, and I. Cohen. Using origami design principles to fold reprogrammable mechanical metamaterials. *Science*, 345(6197):647–650, 2014.

[4] B. Liu, J. L. Silverberg, A. A. Evans, C. D. Santangelo, R. J. Lang, T. C. Hull, and I. Cohen. Topological kinematics of origami metamaterials. *Nature Physics*, 14(8):811, 2018.

[5] J. P. Duncan and J. L. Duncan. Folded developables. *Proc. R. Soc. Lond. A*, 383(1784): 191–205, 1982.

[6] J. C. Badger, T. G. Nelson, R. J. Lang, D. M. Halverson, and L. L. Howell. Normalized coordinate equations and an energy method for predicting natural curved-fold configurations. *Journal of Applied Mechanics*, 86(7):071006, 2019.

[7] M. A. Dias and B. Audoly. A non-linear rod model for folded elastic strips. *Journal of the Mechanics and Physics of Solids*, 62:57–80, 2014.

[8] F. Lechenault and M. Adda-Bedia. Generic bistability in creased conical surfaces. *Physical Review Letters*, 115(23):235501, 2015.

[9] M. G. Walker and K. A. Seffen. On the shape of bistable creased strips. *Thin-Walled Structures*, 124:538–545, 2018.

[10] I Andrade, M Adda-Bedia, and MA Dias. Foldable cones as a framework for nonrigid origami. *arXiv preprint arXiv:1906.02625*, 2019.

[11] L. Walsh, R. Meza, and E. Hamm. Weakening of a thin shell structure by annihilating singularities. *Journal of Physics D: Applied Physics*, 44(23):232002, 2011.

[12] T. A. Witten. Spontaneous free-boundary structure in crumpled membranes. *J. Phys. Chem. B*, 113(12):3738–3742, 2009.

[13] E. H. Mansfield. The inextensional theory for thin flat plates. *Quart. Journ. of Mech. and Applied Math.*, 8(3):338–352, 1955.

[14] D. G. Ashwell. The equilibrium equations of the inextensional theory for thin flat plates. *Quart. Journ. of Mech. and Applied Math.*, 10(2):169–182, 1957.

[15] E. H. Mansfield. Bending, buckling and curling of a heated thin plate. *Proc. R. Soc. Lond. A*, 268(1334):316–327, 1962.

[16] E. L. Starostin and G. H. M. van der Heijden. The shape of a Möbius strip. *Nature Materials*, 6(8):563–567, 2007.

[17] A. Gillman, K. Fuchi, and P. R. Buskohl. Truss-based nonlinear mechanical analysis for origami structures exhibiting bifurcation and limit point instabilities. *International Journal of Solids and Structures*, 147:80–93, 2018.

[18] K. Liu and G. H. Paulino. Nonlinear mechanics of non-rigid origami: an efficient computational approach. *Proc. R. Soc. A*, 473(2206):20170348, 2017.

[19] E. T. Filipov, K. Liu, T. Tachi, M. Schenk, and G. H. Paulino. Bar and hinge models for scalable analysis of origami. *International Journal of Solids and Structures*, 124: 26–45, 2017.

[20] M. A. Dias, L. H. Dudte, L. Mahadevan, and C. D. Santangelo. Geometric mechanics of curved crease origami. *Physical Review Letters*, 109(11):114301, 2012.

[21] D. M. Kleiman, D. F. Hinz, Y. Takato, and E. Fried. Influence of material stretchability on the equilibrium shape of a Möbius band. *Soft Matter*, 12(16):3750–3759, 2016.

[22] Frederic Lechenault, Benjamin Thiria, and Mokhtar Adda-Bedia. Mechanical response of a creased sheet. *Physical Review Letters*, 112(24):244301, 2014.

[23] B.Y. Dharmadasa, H.M.Y.C. Mallikarachchi, and F. López Jiménez. Characterizing the mechanics of fold-lines in thin kapton membranes. In *2018 AIAA Spacecraft Structures Conference, Kissimmee, Florida*, page 0450.

[24] T. Jules, F. Lechenault, and M. Adda-Bedia. Local mechanical description of an elastic fold. *Soft Matter*, 15(7):1619–1626, 2019.

[25] M. G. Walker and K. A. Seffen. The flexural mechanics of creased thin strips. *International Journal of Solids and Structures*, 167:192–201, 2019.

[26] K. C. Francis, J. E. Blanch, S. P. Magleby, and L. L. Howell. Origami-like creases in sheet materials for compliant mechanism design. *Mechanical Sciences*, 4(2):371–380, 2013.

[27] J. Guven, M. M. Müller, and P. Vázquez-Montejo. Isometric bending requires local constraints on free edges. *Mathematics and Mechanics of Solids*, 24(12):4051–4077, 2019.

[28] D. F. Hinz and E. Fried. Translation of Michael Sadowsky's paper "An elementary proof for the existence of a developable Möbius band and the attribution of the geometric problem to a variational problem". *Journal of Elasticity*, 119(1-2):3–6, 2015.

[29] W. Wunderlich. Über ein abwickelbares Möbiusband. *Monatshefte für Mathematik*, 66 (3):276–289, 1962.

[30] E. L. Starostin and G. H. M. van der Heijden. Equilibrium shapes with stress localisation for inextensible elastic Möbius and other strips. *Journal of Elasticity*, 119(1-2):67–112, 2015.

[31] T. Yu and J. A. Hanna. Bifurcations of buckled, clamped anisotropic rods and thin bands under lateral end translations. *Journal of the Mechanics and Physics of Solids*, 122:657–685, 2019.

[32] A. P. Korte, E. L. Starostin, and G. H. M. van der Heijden. Triangular buckling patterns of twisted inextensible strips. *Proceedings of the Royal Society A*, 467(2125):285–303, 2010.

[33] E. L. Starostin and G. H. M. van der Heijden. Tension-induced multistability in inextensible helical ribbons. *Physical Review Letters*, 101(8):084301, 2008.

[34] M. A. Dias and B. Audoly. "Wunderlich, meet Kirchhoff": A general and unified description of elastic ribbons and thin rods. *Journal of Elasticity*, 119(1-2):49–66, 2015.

[35] E. J. Doedel, R. C. Paffenroth, A. R. Champneys, T. F. Fairgrieve, Y. A. Kuznetsov, B. E. Oldeman, B. Sandstede, and X. Wang. AUTO-07P: Continuation and bifurcation software for ordinary differential equations.
`indy.cs.concordia.ca/auto/` , 2007.

Appendices

Appendix A

Bifurcations of anisotropic rods and thin bands under lateral end translations

A.1 Limiting states

The shearing process tends towards limiting states, past which the sheet cannot deform without stretching somewhere. Figures A.1a-b show folded paper models representing a limiting S-like state for $\psi_0 = 0°$ and a limiting U-like state for $\psi_0 = 180°$. The models are flat-foldable for these choices of clamping angle, but more general models can be made. Figure A.1c shows an experimental $uUui$ state (a U-like state from the W family) for a clamping angle $\psi_0 = 30°$. Red arrows point at incipient conical singularities forming near the clamps. In the limit, these cones share a single straight line generator formed from a band diagonal (red lines) that sets the limiting shear to

$$\Delta D_{max} = \sqrt{L^2 + D^2 - (L - \Delta L)^2} - D\,. \tag{A.1}$$

A.2 Numerical continuation of the Kirchhoff equations

To solve the Kirchhoff equations and reconstruct the centerline of the bands, we employ a quaternion representation of the director frame. Additionally, it is most straightforward to represent some of the boundary conditions using classical Euler angles (ψ, θ, ϕ), which we express with reference to a Cartesian coordinate system (x, y, z), before translating them into the quaternion language. These coordinates and angles are shown in Figure A.2, along

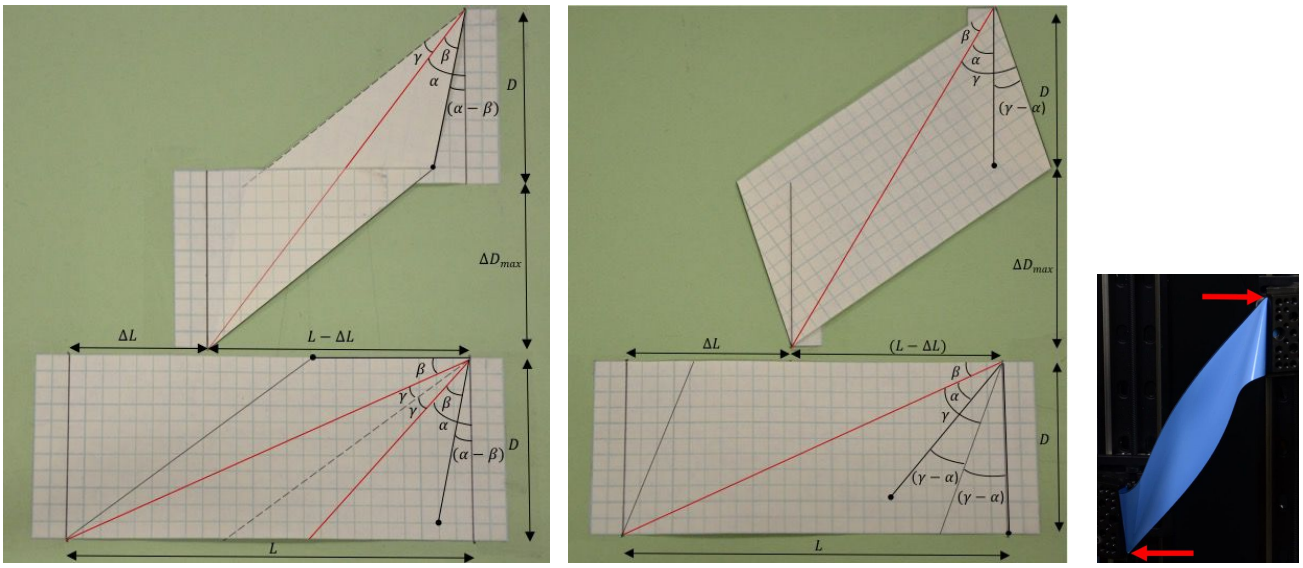

(a) (b) (c)

Figure A.1: Folded paper models representing (a) a limiting S-like state for $\psi_0 = 0°$ and (b) a limiting U-like state for $\psi_0 = 180°$. Clamping occurs on the vertical lines located two squares in from the ends of the gridded paper. The folding process brings red lines and black dots on the bottom reference strips into coincidence (note that there is slight difference in scale between the left and right images). (c) An experimental $uUui$ state for a clamping angle of 30°. Red arrows point at incipient conical singularities.

with a sequence of rotations applied to a band. We place an origin at the starting point of the centerline $\mathbf{X}(0)$ when the shear $\Delta D = 0$. We move the point $\mathbf{X}(0)$ in the negative z direction in the numerics, leaving $\mathbf{X}(L)$ fixed. During the experiments, the z axis is aligned with $-\boldsymbol{d_1}(0)$ and $-\boldsymbol{d_1}(L)$, and the x and y axes are aligned with the sum $\boldsymbol{d_3}(0) + \boldsymbol{d_3}(L)$ and difference $\boldsymbol{d_3}(0) - \boldsymbol{d_3}(L)$, respectively. Thus, the plane of clamping is spanned by x and z. We follow the z-y-z (3-2-3) rotation convention, as given in Love [1]. Our boundary conditions correspond to $\psi(0) = -\psi(L) = \psi_0$, the clamping angle, $\theta(0) = \theta(L) = \pi/2$, and $\phi(0) = \phi(L) = 0$.

The relationship between the director frame and the Cartesian frame may be expressed in terms of either the Euler angles or the components q_i of a unit quaternion [1, 2],

$$\begin{aligned}\begin{bmatrix}\boldsymbol{d_1}\\ \boldsymbol{d_2}\\ \boldsymbol{d_3}\end{bmatrix} &= \begin{bmatrix} cos\phi & \sin\phi & 0\\ -sin\phi & cos\phi & 0\\ 0 & 0 & 1\end{bmatrix}\begin{bmatrix} cos\theta & 0 & -sin\theta\\ 0 & 1 & 0\\ sin\theta & 0 & cos\theta\end{bmatrix}\begin{bmatrix} cos\psi & \sin\psi & 0\\ -sin\psi & cos\psi & 0\\ 0 & 0 & 1\end{bmatrix}\begin{bmatrix}\hat{\boldsymbol{x}}\\ \hat{\boldsymbol{y}}\\ \hat{\boldsymbol{z}}\end{bmatrix}\\ &= 2\begin{bmatrix} q_0^2+q_1^2-\frac{1}{2} & q_1q_2+q_0q_3 & q_1q_3-q_0q_2\\ q_1q_2-q_0q_3 & q_0^2+q_2^2-\frac{1}{2} & q_2q_3+q_0q_1\\ q_1q_3+q_0q_2 & q_2q_3-q_0q_1 & q_0^2+q_3^2-\frac{1}{2}\end{bmatrix}\begin{bmatrix}\hat{\boldsymbol{x}}\\ \hat{\boldsymbol{y}}\\ \hat{\boldsymbol{z}}\end{bmatrix}\end{aligned} \tag{A.2}$$

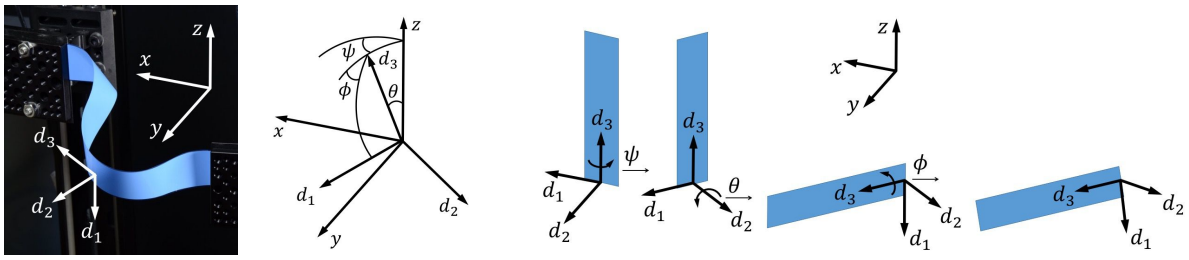

(a) (b) (c)

Figure A.2: Relations between the director frame, Euler angles, and Cartesian coordinates. (a) The director frame and Cartesian coordinates superimposed on a thin band experiment. The right end of the band $\mathbf{X}(0)$ coincides with the Cartesian origin when zero shear is applied, and is translated in the negative z direction during shearing. The z axis is aligned with $-\boldsymbol{d_1}(0)$ and $-\boldsymbol{d_1}(L)$, and the x and y axes are aligned with the sum $\boldsymbol{d_3}(0)+\boldsymbol{d_3}(L)$ and difference $\boldsymbol{d_3}(0)-\boldsymbol{d_3}(L)$, respectively. (b) The Euler angles defined with respect to the director frame and Cartesian coordinates. After Love [1]. (c) The sequence of rotations of a strip implied by the Euler angles, using a z-y-z (3-2-3) rotation convention. Beginning with a frame ($\boldsymbol{d_1}$,$\boldsymbol{d_2}$,$\boldsymbol{d_3}$) aligned with the (x-y-z) axes, we sequentially rotate around $\boldsymbol{d}_3$ by ψ, around $\boldsymbol{d}_2$ by θ, and around $\boldsymbol{d}_3$ by ϕ.

The Euler angles and quaternion components are related by

$$q_0 = \cos\tfrac{\theta}{2}\cos\tfrac{\phi+\psi}{2}\,,\ q_1 = \sin\tfrac{\theta}{2}\sin\tfrac{\phi-\psi}{2}\,,\ q_2 = \sin\tfrac{\theta}{2}\cos\tfrac{\phi-\psi}{2}\,,\ q_3 = \cos\tfrac{\theta}{2}\sin\tfrac{\phi+\psi}{2}\,, \tag{A.3}$$

derivatives of Cartesian components are given by

$$x' = 2(q_1q_3 + q_0q_2)\,,\ y' = 2(q_2q_3 - q_0q_1)\,,\ z' = 2(q_0^2 + q_3^2 - \tfrac{1}{2})\,, \tag{A.4}$$

and derivatives of quaternion components are given by

$$\begin{aligned} q_0' &= \tfrac{1}{2}(-q_1\kappa_1 - q_2\kappa_2 - q_3\tau)\,,\ q_1' = \tfrac{1}{2}(q_0\kappa_1 - q_3\kappa_2 + q_2\tau)\,, \\ q_2' &= \tfrac{1}{2}(q_3\kappa_1 + q_0\kappa_2 - q_1\tau)\,, \quad q_3' = \tfrac{1}{2}(-q_2\kappa_1 + q_1\kappa_2 + q_0\tau)\,. \end{aligned} \tag{A.5}$$

Using nondimensional lengths and curvatures,

$$s \to s/L\,,\ x \to x/L\,,\ y \to y/L\,,\ z \to z/L\,,\ \kappa_1 \to \kappa_1 L\,,\ \tau \to \tau L\,, \tag{A.6}$$

the boundary conditions for position can be combined with those for clamping angle and translated from the Euler angle to quaternion description, for a total of fourteen boundary conditions,

$$\begin{aligned} &q_0(0) = q_0(1) = q_2(0) = q_2(1) = \tfrac{\sqrt{2}}{2}\cos\tfrac{\psi_0}{2}\,, \\ &q_1(0) = -q_1(1) = -q_3(0) = q_3(1) = -\tfrac{\sqrt{2}}{2}\sin\tfrac{\psi_0}{2}\,, \\ &x(0) = y(0) = y(1) = z(1) = 0\,,\ x(1) = \Delta L/L\,,\ z(0) = -\Delta D/L\,, \end{aligned} \tag{A.7}$$

involving three parameters, the compression $\Delta L/L$, shear $\Delta D/L$, and clamping angle ψ_0.

For kinematics described by a general Darboux vector $\boldsymbol{\omega} = \kappa_1\boldsymbol{d_1} + \kappa_2\boldsymbol{d_2} + \tau\boldsymbol{d_3}$, the Kirchhoff equations (2.3) can be written in components as,

$$\begin{aligned} N_1' - N_2\tau + N_3\kappa_2 &= 0\,, \\ N_2' + N_1\tau - N_3\kappa_1 &= 0\,, \\ N_3' + N_2\kappa_1 - N_1\kappa_2 &= 0\,, \\ M_1' - M_2\tau - N_2 + M_3\kappa_2 &= 0\,, \\ M_2' + M_1\tau - M_3\kappa_1 + N_1 &= 0\,, \\ M_3' + M_2\kappa_1 - M_1\kappa_2 &= 0\,. \end{aligned} \tag{A.8}$$

Using nondimensional forces,

$$N_1 \to N_1L^2/(GJ), N_2 \to N_2L^2/(GJ), N_3 \to N_3L^2/(GJ), \tag{A.9}$$

and linear constitutive laws $M_1 = EI_1\kappa_1$, $M_2 = EI_2\kappa_2$, and $M_3 = GJ\tau$, and defining the rigidity ratios $a \equiv EI_1/(GJ)$ and $b \equiv EI_2/(GJ)$, these equations become

$$\begin{aligned} N_1' &= N_2\tau - N_3\kappa_2\,, \\ N_2' &= -N_1\tau + N_3\kappa_1\,, \\ N_3' &= -N_2\kappa_1 + N_1\kappa_2\,, \\ a\kappa_1' &= (b-1)\kappa_2\tau + N_2\,, \\ b\kappa_2' &= (1-a)\kappa_1\tau - N_1\,, \\ \tau' &= (a-b)\kappa_1\kappa_2\,. \end{aligned} \tag{A.10}$$

However, except in Appendix A.4, we use a different set of equations that represent a flat band as a perfectly anisotropic rod that cannot bend around $\boldsymbol{d_2}$. Thus, κ_2 is set to zero, and $M_2 \to M_2L/(GJ)$ is a Lagrange multiplier. For a rod with a rectangular cross-section of width D and thickness t composed of elastically isotropic material, the bending and torsional rigidities are [1],

$$EI_1 = \tfrac{1}{12}EDt^3\,,\ EI_2 = \tfrac{1}{12}ED^3t\,,\ GJ = \lambda GDt^3 = \lambda D\frac{E}{2(1+\nu)}t^3\,, \tag{A.11}$$

in which λ is a shape factor that is a function of D/t. The ratios of bending to torsional rigidity a and b are thus

$$a = \frac{(1+\nu)}{6\lambda}\,,\ b = \frac{(1+\nu)}{6\lambda}\left(\frac{D}{t}\right)^2\,. \tag{A.12}$$

For our narrow bands, $D/t \approx 23.6$, the shape factor is already approaching the asymptotic value $\lambda \to 1/3$, and the ratio b/a is quite large, justifying our approximation of vanishing κ_2. In this limit, the equilibrium equations take the form,

$$\begin{aligned}
N_1' &= N_2\tau\,,\\
N_2' &= -N_1\tau + N_3\kappa_1\,,\\
N_3' &= -N_2\kappa_1\,,\\
M_1' &= M_2\tau + N_2\,,\\
M_2' &= -M_1\tau + M_3\kappa_1 - N_1\,,\\
M_3' &= -M_2\kappa_1\,.
\end{aligned} \tag{A.13}$$

Using the same linear constitutive laws for M_1 and M_3, and combining with the relationships (A.4) and (A.5), we have thirteen equations,

$$\begin{aligned}
N_1' &= N_2\tau\,,\\
N_2' &= -N_1\tau + N_3\kappa_1\,,\\
N_3' &= -N_2\kappa_1\,,\\
a\kappa_1' &= M_2\tau + N_2\,,\\
M_2' &= (1-a)\kappa_1\tau - N_1\,,\\
\tau' &= -M_2\kappa_1\,,\\
q_0' &= \frac{1}{2}(-q_1\kappa_1 - q_3\tau)\,,\ q_1' = \frac{1}{2}(q_0\kappa_1 + q_2\tau)\,,\\
q_2' &= \frac{1}{2}(q_3\kappa_1 - q_1\tau)\,,\ q_3' = \frac{1}{2}(-q_2\kappa_1 + q_0\tau)\,,\\
x' &= 2(q_1q_3 + q_0q_2)\,,\ y' = 2(q_2q_3 - q_0q_1)\,,\ z' = 2(q_0^2 + q_3^2 - \tfrac{1}{2})\,.
\end{aligned} \tag{A.14}$$

The system (A.14) and (A.7) has one excess boundary condition. The redundancy comes from the fact that quaternion components satisfy the algebraic constraint $q_0^2+q_1^2+q_2^2+q_3^2 = 1$. We need only specify all four components at one end, so we simply do not use the $q_0(1)$ boundary condition.

Adding a nondimensional body force g to the equilibrium equations modifies the first three to

$$\begin{aligned}
N_1' &= N_2\tau - 2g(q_0q_2 - q_1q_3)\,,\\
N_2' &= -N_1\tau + N_3\kappa_1 + 2g(q_2q_3 + q_0q_1)\,,\\
N_3' &= -N_2\kappa_1 + 2g(q_0^2 + q_3^2 - \tfrac{1}{2})\,.
\end{aligned} \tag{A.15}$$

A good starting point for continuation is the circular configuration

$$\begin{aligned} N_1 = 0, N_2 = 0, N_3 = 0\,, \\ \kappa_1 = 2\pi, M_2 = 0, \tau = 0\,, \\ q_0 = \tfrac{\sqrt{2}}{2}\sin(\pi s)\,,\ q_1 = -\tfrac{\sqrt{2}}{2}\cos(\pi s)\,, \\ q_2 = \tfrac{\sqrt{2}}{2}\sin(\pi s)\,,\ q_3 = \tfrac{\sqrt{2}}{2}\cos(\pi s)\,, \\ x = -\tfrac{\sin 2\pi s}{2\pi}\,,\ y = \tfrac{1-\cos 2\pi s}{2\pi}, z = 0\,, \end{aligned} \tag{A.16}$$

from which the ends can be opened and rotated to achieve various buckled states. Note that we cannot apply compression directly to a straight configuration, because the initial guess for Auto 07P cannot be a branch point [3].

The rod frame renderings are achieved by sweeping the director $\boldsymbol{d}_1(s)$ along the center line $\mathbf{X}(s)$. The resulting surface can be parameterized as

$$\begin{aligned} \boldsymbol{R}(s,v) &= \mathbf{X}(s) + v\boldsymbol{d}_1(s)\,, \\ &= \left[x + 2v\left(q_0^2 + q_1^2 - \tfrac{1}{2}\right)\right]\hat{\boldsymbol{x}} + \left[y + 2v\left(q_1q_2 + q_0q_3\right)\right]\hat{\boldsymbol{y}} + \left[z + 2v\left(q_1q_3 - q_0q_2\right)\right]\hat{\boldsymbol{z}}\,, \end{aligned} \tag{A.17}$$

with $-\frac{D}{2L} \le v \le \frac{D}{2L}$. Note that a finite-width band will deform into a different surface. The above surface corresponding to the rod frame is thus only a rough approximation to the actual shape of a narrow band. In a developable model, the generators do not coincide with the material directors $\boldsymbol{d}_1$.

A.3 Poisson's ratio

Using two-parameter continuation in shear-Poisson's ratio space, we have confirmed that the effects of Poisson's ratio ν on the results for perfectly anisotropic rods are minimal, with the exception of bifurcations such as 0, 1, and 2, which are associated with highly twisted states. This is consistent with Goss's results for isotropic rods [4]. Figure A.3 shows a representative example for the clamping angle $\psi_0 = 15°$, showing the shear value of the bifurcation for admissible positive values of Poisson's ratio. Poisson's ratio affects the ratios of bending to torsional rigidity (A.12). A larger ν means a relatively lower torsional rigidity, and thus a wider range of stability for highly twisted states.

A.4 Anisotropy

Using the full rod equations (A.10), we confirm that much of the complexity of our solution manifolds is due to the anisotropy of the rod. For a rod with square cross section, $\lambda \approx 0.141$ [1], $a = b \approx 1.478$ for $\nu = 0.25$, and τ is a constant. Analytical solutions exist for such systems,

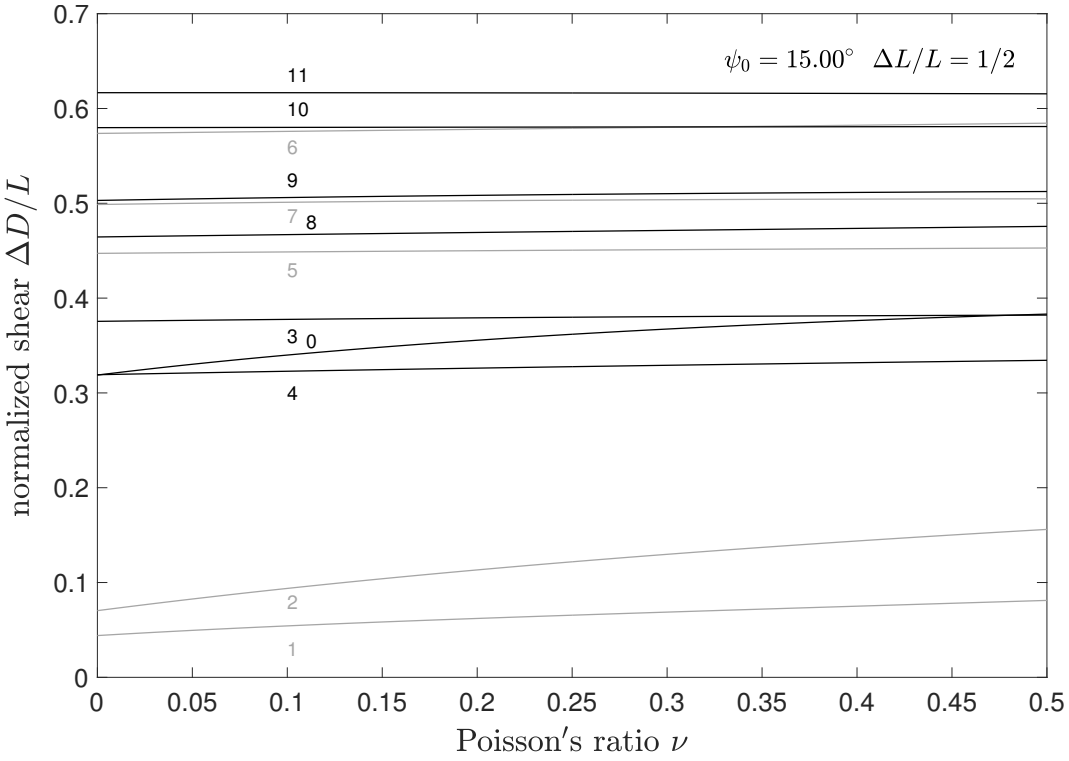

Figure A.3: Effect of Poisson's ratio ν on the shear value of bifurcations with clamping angle $\psi_0 = 15°$. Points 0, 1, and 2 are associated with highly twisted states, and are affected the most. A ν of 0.25 was used in this work.

but for brevity we present numerical continuation results in Figure A.4 for clamping angles of $\psi_0 = 0°$ (black curves) and $\psi_0 = 15°$ (brown curves). This can be compared with Figures 2.3 and 2.7 in Section 2.4. Aside from the absence of twisted states, the connectivity of the solution manifolds is quite different, and fewer states exist at high shear.

For zero clamping angle $\psi_0 = 0°$, shearing the first mode of planar *elastica* deforms the rod into a spatial configuration with two nonzero curvatures and a constant twist. At a supercritical pitchfork bifurcation at $\Delta D/L \approx 0.685$, the shape eventually changes to the second mode of planar *elastica* in a plane perpendicular to that of the initial configuration. This state has only one curvature and zero twist. We thus realize that for an isotropic rod, the shear is simply equivalent to a meaningless spatial rotation plus changes in compression and clamping angle, the latter serving to exchange the stability of first and second mode *elastica*. This behavior can be imperfectly observed in a smartphone charger cord, despite the inevitable presence of rest curvature in such objects. For nonzero clamping angle, this pitchfork is broken and the configurations remain non-planar at high shears.

Further tinkering with the numerics shows that at zero clamping angle, the bifurcations on the first mode (U) branch to the $US\pm$ and uUu branches appear when the anisotropy D/t reaches moderate values. Buzano [5] studied the appearance of secondary bifurcations of

compressed, clamped rectangular cross section rods when the cross section became infinitesimally anisotropic. van der Heijden and Thompson [6] discuss a transition in the behavior of elliptical cross section rods when the anisotropy reaches a moderate value.

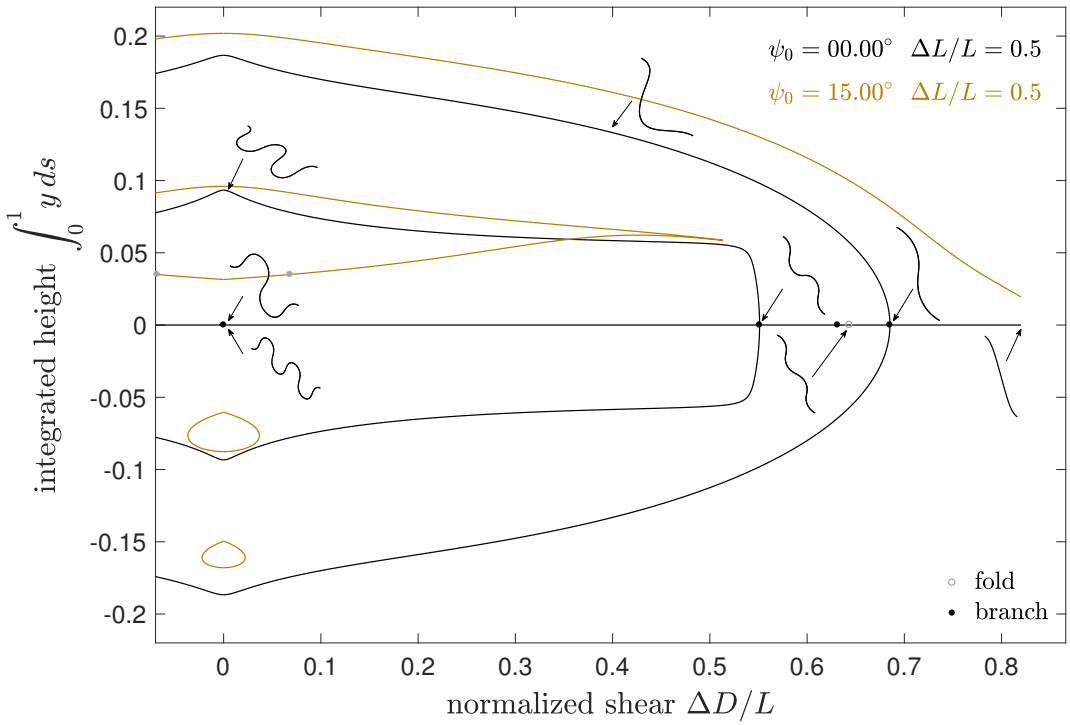

Figure A.4: Solution curves and bifurcations (open and closed disks) for square cross section Kirchhoff rods for clamping angles $\psi_0 = 0°$ and $\psi_0 = 15°$, along with drawn curves from the arrowed locations for $\psi_0 = 0°$. Compare with Figures 2.3 and 2.7.

A.5 Comparison with a strip model

Here we use one of our experimental deformation paths to compare the anisotropic Kirchhoff rod model with a strip model implemented in a manner following van der Heijden and Starostin [7]. In strip models, the description of inflection points is singular, and in this implementation, such points are inserted by hand. We display two consequences of this situation. One is that numerical continuation will not lead to the creation of new inflection points. We can allow pre-existing inflection points to move as internal boundaries within the strip by using the approach of Ascher and Russell [8], but they cannot spontaneously appear or disappear. It seems that this issue did not arise in the work of Dias and Audoly [9, 10] or Audoly and Seffen [11], where continuation was performed along branches that did not involve creation of new inflection points. Second, at the pre-set inflection points, the curvature and torsion behave strangely. As the limit of a narrow strip is approached,

these quantities develop sharp gradients and do not approach those of a rod, but instead a singular limit involving a jump in curvature [12], which would indicate a singular source of moment in a rod. While the first issue may arise from our choice of implementation, the second is a characteristic of inextensible strip models themselves, and can be observed in the prior results of several groups [7, 13], including two-dimensional simulations of strips in the inextensible limit [14]. Both issues are such that strip models cannot capture some of the behavior in our experiments, which involve the creation and destruction of inflection points, and in which the curvature and torsion appear to be well-behaved. Regularization of the strip energy may resolve the first issue, but does not resolve the second [13]. Others have suggested the use of a piecewise-continuous energy density, with modifications in regions of small curvature [15]. We conclude that there is a need for new models of strips that interpolate between rod models and wide, inextensible strip models. A good testing ground for such a model might be the simple case of a body subject to simple tensile end constraints and twist. A rod model admits twisted solutions with a straight centerline [16], which do not correspond to developable surfaces.

Figure A.5 compares results from the rod model (blue) and a Wunderlich strip model [7] applied to narrow (red, $D/L = 1/80$) and wide (grey, $D/L = 1/8$) strips, for values of compression $\Delta L/L = 0.5$, clamping angle $\psi_0 = 45°$, and a sequence of shears $\Delta D/L = 0.2, 0.4, 0.56, 0.6$. This corresponds to a path along the *U-w-uUui* branch shown in the supplementary video `widtheffect45.mp4` [17]. The configurations begin with two inflection points near the ends. In experiments, narrow bands smoothly gain two additional inflection points near the middle, and wide bands experience a snap-through instability which also creates two inflection points. The numerical rod solutions behave like the experimental narrow bands. The numerical strip solutions do not pick up new inflection points or detect a snap-through bifurcation. Recall that the single curvature and twist of a perfectly anisotropic rod can be identified with the curvature and torsion for a developable strip. The singular behavior of the curvature and torsion are most apparent for narrow strips.

The rod model and the rendering of the rod frame have already been discussed in the main text and Appendix A.2. The strip model employs the Wunderlich functional proportional to $\kappa_1^2(1+\eta^2)^2\frac{1}{D\eta'}\ln(\frac{1+D\eta'/2}{1-D\eta'/2})$, where $\eta \equiv \frac{\tau}{\kappa_1}$. The limit of this model as the strip width D vanishes is known as the Sadowsky functional, which lacks the logarithmic term and its prefactor. The Wunderlich functional leads to a set of Euler-Lagrange equations, equivalent up to a sign to equations (29) in [7]. The strips are rendered as rectifying developables

$$\boldsymbol{R}(s,v) = \mathbf{X}(s) + v\left[\boldsymbol{d}_1(s) + \eta(s)\boldsymbol{d}_3\right], \tag{A.18}$$

with $-\frac{D}{2L} \le v \le \frac{D}{2L}$. Generators are drawn on the wide strips, showing the focusing of bending energy akin to that shown in Figure 2.19 and in the video.

The solution of the strip model involves several steps, which we merely sketch here, referring the reader to the necessary references for extensive details. First, a starting solution is obtained from the Euler *elastica* or rod model configuration at zero shear. In the Wunderlich model, but not the Sadowsky model, the description of the energy density is singular, and a

Taylor expansion in η' is applied to find a suitable starting solution for continuation, until the shear is a small nonzero value. The solution is partitioned into pieces by its inflection points. The resulting multi-point variable-arc-length boundary value problem is reformulated as a standard two-point boundary value problem by the introduction of scalar variables [8] representing the dynamically updating lengths of segments between the inflection points, and solved using the continuation package AUTO 07P [3]. At each inflection point, a small jump in curvature and torsion is introduced [7] such that the ratio η is continuous; this jump is decreased as far as numerical stiffness will allow. Near these jumps, "ears" develop in the curvature profile and a spurious extra oscillation in the torsion arises due to the requirement that the torsion vanish with the curvature. These features, which are not seen in experiments, become more extreme as the strip width shrinks, as can be clearly seen in Figure A.5 and in numerical results on one- and two-dimensional inextensible models in the literature, such as Figure 7 of [7], Figure 6 of [13], and Figure 4 of [14]. The Sadowsky limit of the "ears" is a jump in curvature [12], something that cannot exist in a Kirchhoff rod model without an applied moment. Note that this jump is orders of magnitude larger than the artificial jump introduced in order to handle the numerics near the inflection point.

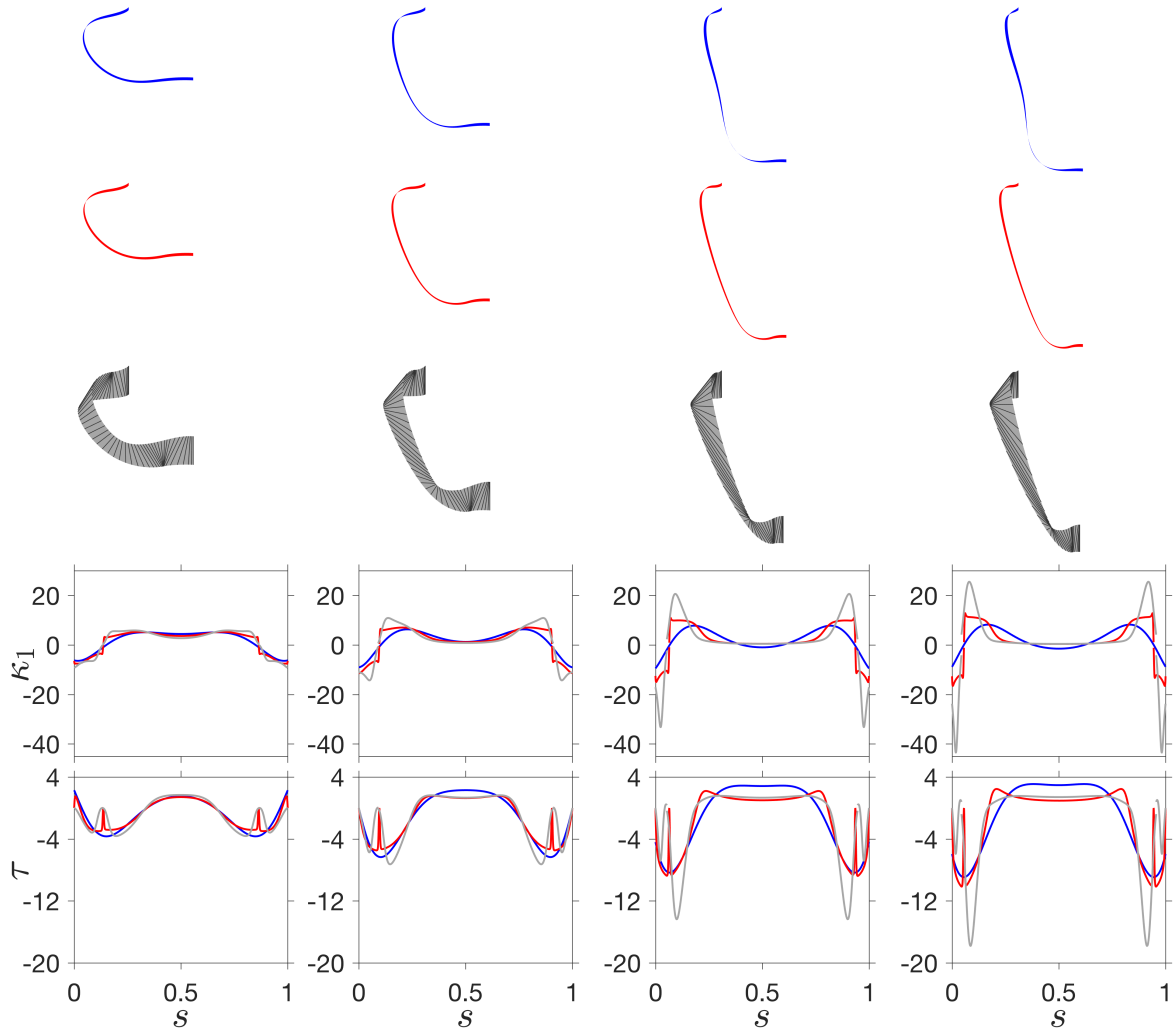

Figure A.5: Numerically determined configurations, curvature, and torsion (twist) corresponding to a path along the *U-w-uUui* branch shown in the supplementary video `widtheffect45.mp4`, with compression $\Delta L/L = 0.5$, clamping angle $\psi_0 = 45°$, and shear $\Delta D/L = 0.2, 0.4, 0.56, 0.6$ increasing from left to right. Shown are renderings of the rod frame based on the perfectly anisotropic Kirchhoff rod equations (blue) and renderings of the rectifying developable corresponding to the Wunderlich strip equations for narrow (red, $D/L = 1/80$) and wide (grey, $D/L = 1/8$) strips, with generators drawn on the wide strip. As explained in the text, continuation of the Wunderlich model following the approach of [7] does not capture either the appearance of inflection points in narrow bands or the occurrence of a snap-through in wide bands. All solutions begin with two inflection points near the ends, and the rod solution gains two additional inflection points near the middle. Note the singular behavior of the narrow band curvature and torsion near the two inflection points. Jumps in curvature and torsion are introduced to handle the inflection points in the strip model [7].

Bibliography

[1] A. E. H. Love. *A treatise on the mathematical theory of elasticity*. Dover, New York, 1927.

[2] S. L. Altmann. *Rotations, quaternions, and double groups*. Clarendon Press, Oxford, 1986.

[3] E. J. Doedel, R. C. Paffenroth, A. R. Champneys, T. F. Fairgrieve, Y. A. Kuznetsov, B. E. Oldeman, B. Sandstede, and X. Wang. AUTO-07P: Continuation and bifurcation software for ordinary differential equations. `indy.cs.concordia.ca/auto/` , 2007.

[4] V. G. A. Goss. *Snap buckling, writhing and loop formation in twisted rods*. PhD thesis, University College London, 2003.

[5] E. Buzano. Secondary bifurcations of a thin rod under axial compression. *SIAM Journal on Mathematical Analysis*, 17(2):312–321, 1986.

[6] G. H. M. van der Heijden and J. M. T. Thompson. Lock-on to tape-like behaviour in the torsional buckling of anisotropic rods. *Physica D*, 112(1-2):201–224, 1998.

[7] E. L. Starostin and G. H. M. van der Heijden. Equilibrium shapes with stress localisation for inextensible elastic Möbius and other strips. *Journal of Elasticity*, 119(1-2):67–112, 2015.

[8] U. Ascher and R.D. Russell. Reformulation of boundary value problems into "standard" form. *SIAM Review*, 23(2):238–254, 1981.

[9] M. A. Dias and B. Audoly. A non-linear rod model for folded elastic strips. *Journal of the Mechanics and Physics of Solids*, 62:57–80, 2014.

[10] M. A. Dias and B. Audoly. "Wunderlich, meet Kirchhoff": A general and unified description of elastic ribbons and thin rods. *Journal of Elasticity*, 119(1-2):49–66, 2015.

[11] B. Audoly and K. A. Seffen. Buckling of naturally curved elastic strips: The ribbon model makes a difference. *Journal of Elasticity*, 119(1-2):293–320, 2015.

[12] D. F. Hinz and E. Fried. Translation and interpretation of Michael Sadowsky's paper "Theory of elastically bendable inextensible bands with applications to the Möbius band". *Journal of Elasticity*, 119(1-2):7–17, 2015.

[13] A. Moore and T. J. Healey. Computation of elastic equilibria of complete Möbius bands and their stability. *Mathematics and Mechanics of Solids*, 24(4):939–967, 2019.

[14] D. M. Kleiman, D. F. Hinz, Y. Takato, and E. Fried. Influence of material stretchability on the equilibrium shape of a Möbius band. *Soft Matter*, 12(16):3750–3759, 2016.

[15] L. Freddi, P. Hornung, M. G. Mora, and R. Paroni. A corrected Sadowsky functional for inextensible elastic ribbons. *Journal of Elasticity*, 123(2):125–136, 2016.

[16] A. Goriely, M. Nizette, and M. Tabor. On the dynamics of elastic strips. *Journal of Nonlinear Science*, 11(1):3–45, 2001.

[17] Six supplementary videos are available at:
http://www.sciencedirect.com/science/article/pii/S0022509617307469.

Appendix B

Exact and approximate mechanisms for pure bending of thin sheets

B.1 Maximum achievable curvature

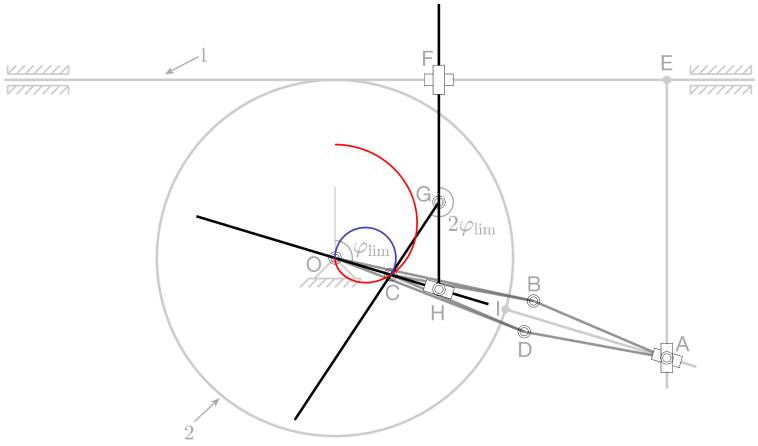

Figure B.1: A configuration near the limiting configuration in which the links of the kite-shaped inversor OABCD align.

The maximum curvature and minimum sample length are limited in practice by the bending angle at which the links of the kite-shaped inversor OABCD align (see Figure B.1). This limiting angle φ_{lim} is related to the link lengths l and m and the wheel size R through the trigonometric relationship

$$(l+m)\sin\varphi_{\text{lim}} = R\varphi_{\text{lim}}\,. \tag{B.1}$$

Note that $l+m<R$. The sample radius at this limit is

$$r_{0\text{lim}} = \frac{L}{2\varphi_{\text{lim}}} = \frac{l^2 - m^2}{2R\varphi_{\text{lim}}} = \frac{l - m}{2\sin\varphi_{\text{lim}}}, \tag{B.2}$$

where the second and third equalities in (B.2) use $LR = l^2 - m^2$ from Section 3.2.1, and (B.1), respectively.

Among other things, these relationships tell us that for a fixed R, the limiting radius can be made arbitrarily small at some finite limiting angle by shrinking the difference in link lengths $l - m$.

B.2 Solutions for Euler *elastica*

The Euler *elastica* is an analytically tractable system, but for expedience we decided to forego an extended exercise in elliptic integrals and instead use a continuation code for rods already on hand to quickly compute the solutions in Figures 3.4c-3.4e. The Kirchhoff equations for an inextensible rod in two dimensions, and the kinematics in terms of an angle θ measured clockwise from the vertical, are

$$\begin{aligned} \partial_s N_2 - N_3\kappa &= 0, \\ \partial_s N_3 + N_2\kappa &= 0, \\ \partial_s M(\kappa) - N_2 &= 0, \\ \partial_s \theta &= \kappa, \\ \partial_s x &= \sin\theta, \\ \partial_s y &= \cos\theta, \end{aligned} \tag{B.3}$$

where N_2 and N_3 are the components of the contact force along the normal and tangential directions, respectively, and $M(\kappa)$ is a general constitutive law representing the moment-curvature response of the sheet. For an *elastica*, M is linear in κ. The choice of bending stiffness does not affect the shape in response to displacement boundary conditions. These conditions for the approximate mechanism are

$$\begin{aligned} x(0) = 0,\ y(0) = 0,\ \theta(0) = 0,\ x(1) &= \left(\sqrt{\eta^2 - (1-\eta)^2\sin\varphi^2} + (1-\eta)\cos\varphi\right)\sin\varphi, \\ y(1) &= \left(\sqrt{\eta^2 - (1-\eta)^2\sin\varphi^2} + (1-\eta)\cos\varphi\right)\cos\varphi,\ \theta(1) = 2\varphi. \end{aligned} \tag{B.4}$$

We solve the system (B.3)-(B.4) using the continuation package AUTO 07P [1]. Starting with a half-circle configuration, we move the sample end to the position corresponding to $\varphi = \pi/2$, then continue φ down to 0, the straight configuration. Using instead the straight configuration as a starting solution does not work well, perhaps because the equations are one-sidedly constrained by inextensibility.

Bibliography

[1] E. J. Doedel, R. C. Paffenroth, A. R. Champneys, T. F. Fairgrieve, Y. A. Kuznetsov, B. E. Oldeman, B. Sandstede, and X. Wang. AUTO-07P: Continuation and bifurcation software for ordinary differential equations.
`indy.cs.concordia.ca/auto/` , 2007.

Appendix C

Bistabilities of creases under removal of singularities

C.1 Numerical continuation of an inextensible strip model

To solve the inextensible strip equations and reconstruct the developable surface, we employ classical Euler angles (ψ, θ, ϕ) to describe rotations of the director frame $(\boldsymbol{T}, \boldsymbol{N}, \boldsymbol{B})$. Figure C.1 shows a Cartesian coordinate system (x, y, z) and a sequence of rotations applied to deform an annulus sector to match with the crease boundaries. We place an origin at $\frac{\boldsymbol{r}(0)+\boldsymbol{r}(L)}{2}$, with the z axis aligned with the axis of rotational symmetry and $x-z$ being a plane of symmetry . Because of the N-fold mirror symmetry (together with the z axis, each crease makes a plane of symmetry) and N-fold rotational symmetry within an evenly distributed set of N creases, we only need to solve for an annulus sector that subtends an angle of $2\pi/N$.

The relationship between the director frame and the Cartesian frame can be written as [1],

$$\begin{bmatrix} -\boldsymbol{N} \\ \boldsymbol{T} \\ \boldsymbol{B} \end{bmatrix} = \begin{bmatrix} \cos\phi & \sin\phi & 0 \\ -\sin\phi & \cos\phi & 0 \\ 0 & 0 & 1 \end{bmatrix} \begin{bmatrix} \cos\theta & 0 & -\sin\theta \\ 0 & 1 & 0 \\ \sin\theta & 0 & \cos\theta \end{bmatrix} \begin{bmatrix} \cos\psi & \sin\psi & 0 \\ -\sin\psi & \cos\psi & 0 \\ 0 & 0 & 1 \end{bmatrix} \begin{bmatrix} \boldsymbol{i} \\ \boldsymbol{j} \\ \boldsymbol{k} \end{bmatrix}. \tag{C.1}$$

Together with $\kappa_n = -\boldsymbol{N}' \cdot \boldsymbol{T}$, $\kappa_g = \boldsymbol{B}' \cdot \boldsymbol{T}$, and $\tau_g = -\boldsymbol{B}' \cdot \boldsymbol{N}$, we have

$$\kappa_n = \phi' + \cos\theta\psi', \kappa_g = \psi' \sin\theta\cos\phi - \theta' \sin\phi, \tau_g = \theta' \cos\phi + \psi' \sin\theta \sin\phi. \tag{C.2}$$

By combining $\boldsymbol{r}'(s) = \boldsymbol{T}$, equations (5.3), (C.2), and the algebraic constraint $\chi(V(s,\eta), s, \eta) = 0$, we have

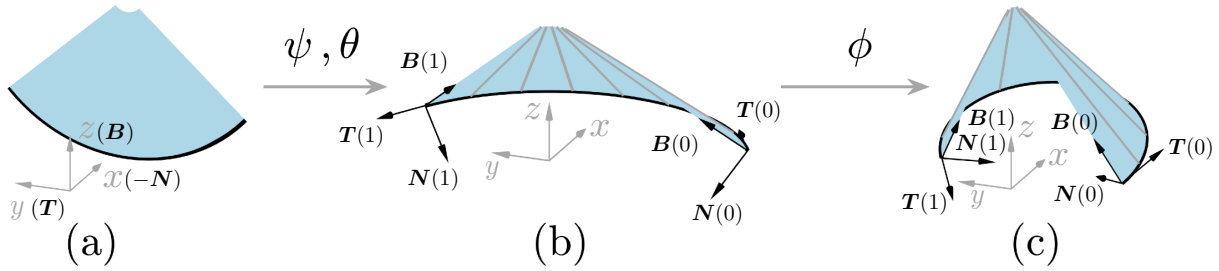

Figure C.1: Euler angles are used to describe the sequential rotations of the director frame attached to the outer circle of an annulus sector, following a $z-y-z$ (3-2-3) rotation convention. A Cartesian coordinate system $(x-y-z)$ is placed such that the z axis is aligned with the axis of rotational symmetry, $z-x$ makes a plane of symmetry of the annulus sector, and the two ends $\boldsymbol{r}(0)$ and $\boldsymbol{r}(L)$ are in the $x-y$ plane. (a) The annulus sector has its director frame $(-\boldsymbol{N},\boldsymbol{T},\boldsymbol{B})$ attached to the outer circle and aligned with the x, y, and z axes, respectively. (b) The annulus sector is deformed into a cone frustum by rotating the director frame about $\boldsymbol{B}(s)$ by $\psi(s)$, and then about $\boldsymbol{T}(s)$ by $\theta(s)$. In this step, $\psi(s)$ is a linear function of s and $\theta(s)$ is constant. (c) The crease angle is introduced by rotating the director frame at the two ends about $\boldsymbol{B}(0)$ and $\boldsymbol{B}(1)$.

$$
\begin{aligned}
F_1' - \kappa_n F_2 + \kappa_g F_3 = 0\,,\, F_2' + \kappa_n F_1 - \kappa_n \eta F_3 = 0\,,\, F_3' + \kappa_n \eta F_2 - \kappa_g F_1 = 0\,,\\
M_1' - \kappa_n M_2 + \kappa_g M_3 = 0\,,\, M_2' + \kappa_n M_1 - \kappa_n \eta M_3 - F_3 = 0\,,\, M_3' + \kappa_n \eta M_2 - \kappa_g M_1 + F_2 = 0\,,\\
(AE - C^2)\kappa_n' + (BE - DC)\eta' = FE - GC\,,\\
(AE - C^2)\eta'' + (AD - CB)\eta' = AG - CF\,,\\
\psi' = (\tau_g \sin\phi + \kappa_g \cos\phi)/\sin\theta\,,\, \theta' = \tau_g \cos\phi - \kappa_g \sin\phi\,,\\
\phi' = \kappa_n - (\kappa_g \cos\phi + \tau_g \sin\phi)/\tan\theta\,,\, x' = -\sin\psi\cos\phi - \cos\psi\sin\phi\cos\theta\,,\\
y' = \cos\psi\cos\phi - \sin\psi\sin\phi\cos\theta\,,\, z' = \sin\theta\sin\phi\,,\\
s' = 1\,,\, V' = -\frac{\chi_s}{\chi_V} - \frac{\chi_\eta}{\chi_V}\eta'\,,
\end{aligned}
\tag{C.3}
$$

in which

$$
\begin{aligned}
A = Y_{\kappa_n\kappa_n} W\,,\, B = Y_{\kappa_n\eta} W + Y_{\kappa_n} W_\eta + Y_{\kappa_n} W_V V_\eta\,,\, C = Y_{\kappa_n\eta'} W + Y_{\kappa_n} W_{\eta'}\,,\\
D = Y_{\eta'\eta} W + Y_{\eta'} W_\eta + Y_{\eta'} W_V V_\eta + Y_\eta W_{\eta'} + Y W_{\eta'\eta} + Y W_{\eta' V} V_\eta\,,\\
E = Y_{\eta'\eta'} W + 2 Y_{\eta'} W_{\eta'} + W_{\eta'\eta'} Y\,,\, F = \eta' M_1 - F_2 + \kappa_g (M_1 - \eta M_3) - Y_{\kappa_n} W_V V_s\,,\\
G = Y_\eta W + Y W_\eta + Y W_V V_\eta - \kappa_n M_1 - Y_{\eta'} W_V V_s - Y W_{\eta' V} V_s\,,
\end{aligned}
\tag{C.4}
$$

where a subscript represents a partial derivative. With vanishing external forces, the contact force $\boldsymbol{F}$ should be a constant vector. Due to the symmetry, the contact force vanishes

identically. The N-fold mirror symmetry of the structure further forces the contact moment $\boldsymbol{M}$ to align with the z axis, and thus the whole structure is under pure bending. We have $\boldsymbol{F} = \boldsymbol{0}$ and $\boldsymbol{M} = M_z\boldsymbol{k}$. Forces in the symmetric plane and moments perpendicular to the symmetric plane should be zero. The boundary conditions at the two ends of an annulus sector in inverted configurations can be summarized as

$$\begin{aligned} x(0) = -y(0)\cot\frac{\pi}{N}, z(0) = 0, x(L) = y(L)\cot\frac{\pi}{N}, z(L) = 0, y(0) + y(1) = 0, \\ \psi(0) = -\frac{\pi}{N}, \phi(0) = -\left(\frac{\pi}{2} - \frac{\gamma_0}{2}\right), \psi(L) = \frac{\pi}{N}, \phi(L) = \left(\frac{\pi}{2} - \frac{\gamma_0}{2}\right), \eta(0) = 0, \eta(L) = 0, \\ F_z(0) = 0, F_r(0) = 0, M_t(0) = 0, s(0) = 0, \chi(V(0), 0, \eta(0)) = 0, \\ \frac{\kappa_n(0)(1+\eta^2(0))^2}{\eta'(0) + \kappa_g(0)(1+\eta^2(0))} W(\eta'(0), \eta(0)) - \eta(0)M_1(0) - M_3(0) = 0, \end{aligned} \tag{C.5}$$

in which $F_r(0) = \boldsymbol{F}(0)\cdot(-\cos(\frac{\pi}{N})\boldsymbol{i} + \sin(\frac{\pi}{N})\boldsymbol{j})$ and $F_z(0) = \boldsymbol{F}(0)\cdot\boldsymbol{k}$ are forces in the plane of symmetry, and $M_t(0) = \boldsymbol{M}(0)\cdot(\sin(\frac{\pi}{N})\boldsymbol{i} + \cos(\frac{\pi}{N})\boldsymbol{j})$ is the moment perpendicular to the plane of symmetry. Boundary conditions of the creased configuration can be obtained similarly, except that the two ends are rotated to opposite directions, namely $\phi(0) = (\frac{\pi}{2} - \frac{\gamma_0}{2})$ and $\phi(L) = -(\frac{\pi}{2} - \frac{\gamma_0}{2})$.

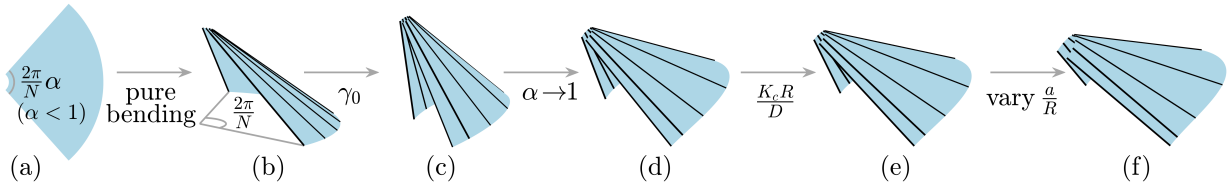

Figure C.2: The creased equilibrium is obtained through several continuation steps. (a) An annulus sector that subtends an angle less than $2\pi/N$ (i.e., $\alpha < 1$). (b) The annulus is purely bent into a cone frustum with a central angle of $2\pi/N$. (c) Rigid creases are added at the two ends by rotating the director frame about the crease. (d) α is increased to 1. (e) A finite crease stiffness is introduced. (f) The hole size is varied.

We use a part of a cone frustum as a starting solution for numerical continuation of the two-point boundary value problem consisting of equations (C.3) and (C.5). An annulus sector that subtends an angle of $2\pi\alpha/N$ $(0 < \alpha < 1)$ can be deformed into a cone frustum that subtends an angle of $2\pi/N$ through pure bending. The starting solution describing the cone frustum in Figure C.2b can be summarized as

$$
\begin{aligned}
&F_{10}=0\,,F_{20}=0\,,F_{30}=0\,,M_{10}=0\,,M_{20}=\ln\frac{a}{R}\,,M_{30}=-\ln\frac{a}{R}\sqrt{\frac{1}{\alpha^2}-1}\,,\\
&\kappa_{n0}=\sqrt{(\frac{\kappa_g}{\alpha})^2-\kappa_g^2}\,,\eta_0=0\,,\eta_0'=0\,,\psi_0=-\frac{\pi}{N}-\frac{\kappa_g}{\alpha}s_0\,,\theta_0=-\sin^{-1}\alpha\,,\phi_0=0\,,\\
&x_0=-\frac{\alpha}{\kappa_g}\cos\left(\frac{\pi}{N}+\frac{\kappa_g}{\alpha}s_0\right),y_0=\frac{\alpha}{\kappa_g}\sin\left(\frac{\pi}{N}+\frac{\kappa_g}{\alpha}s_0\right),z_0=0,s_0\in\left[0\,,\tfrac{2\pi R}{N}\alpha\right],V_0=R-a\,,
\end{aligned}
\tag{C.6}
$$

where α is the angle deficit. In all simulations, we fix R to 1 (i.e., $\kappa_g=-1$). We start from a cone frustum with a small hole and rotate the two ends to generate the crease angle. Then, we increase the angle deficit α to 1. Crease stiffness is "introduced" by substituting the two boundary conditions $\phi(0)=-0.5(\pi-\gamma_0)$ and $\phi(1)=0.5(\pi-\gamma_0)$ in equation (C.5) with $M_3(0)=-K_cR/D(1-b/R)\sin(\pi-\gamma_0+2\phi(0))$ and $M_3(L)=K_cR/D(1-b/R)\sin(\pi-\gamma_0-2\phi(L))$, respectively. In this step, we decrease K_cR/D from a large number to the real crease stiffness. Finally, the hole size a for a circular hole, or a and b for an elliptic hole, is varied to study the bistable behavior.

An annulus sector can be reconstructed as

$$
\begin{aligned}
\boldsymbol{X}(s,v)&=\boldsymbol{r}(s)+v[\boldsymbol{B}(s)+\eta(s)\boldsymbol{T}(s)]\,,\\
&=(x-v[\eta(\sin\psi\cos\phi+\cos\psi\sin\phi\cos\theta)-\sin\theta\cos\psi])\boldsymbol{i}\\
&\quad+(y+v[\eta(\cos\psi\cos\phi-\sin\psi\sin\phi\cos\theta)+\sin\theta\sin\psi])\boldsymbol{j}\\
&\quad+(z+v[\eta\sin\theta\sin\phi+\cos\theta])\boldsymbol{k}\,,
\end{aligned}
\tag{C.7}
$$

where $\eta=\tau_g/\kappa_n, v\in[0,V]$. The complete structure can be constructed by the symmetry of the creased thin disk. We call points where $\eta'=-\kappa_g(1+\eta^2)$ "cylindrical." At a cylindrical point, the mean curvature is constant along the local generator. The edge of regression, where adjacent generators intersect with each other, can be defined as

$$
\boldsymbol{c}(s)=\boldsymbol{r}(s)+\frac{\sin\beta}{\beta'-\kappa_g}\frac{\boldsymbol{B}(s)+\eta(s)\boldsymbol{T}(s)}{|\boldsymbol{B}(s)+\eta(s)\boldsymbol{T}(s)|}=\boldsymbol{r}(s)-\frac{\boldsymbol{B}(s)+\eta(s)\boldsymbol{T}(s)}{\eta'+\kappa_g(1+\eta^2)}\,.
\tag{C.8}
$$

By differentiation, we have $\boldsymbol{c}'(s)=\frac{[\eta\kappa_g^2(1+\eta^2)+\eta''+3\kappa_g\eta\eta']}{[\eta'+\kappa_g(1+\eta^2)]^2}(\boldsymbol{B}+\eta\boldsymbol{T})$. We call isolated points where $\eta''=-3\kappa_g\eta\eta'-\eta\kappa_g^2(1+\eta^2)$ "conical." At a conical point, the edge of regression contains a cusp. The distribution of the generators can be mapped onto the annulus sector as

$$
\begin{aligned}
\boldsymbol{X}(s,v)&=\boldsymbol{r}(s)+v[\boldsymbol{b}(s)+\eta(s)\boldsymbol{t}(s)]\,,\\
&=(\sin\lambda-v\sin\lambda+v\eta\cos\lambda)\boldsymbol{i}+\left(v\eta\sin\lambda+v\cos\lambda-\frac{1}{\pi}\cos\lambda\right)\boldsymbol{j}\,,
\end{aligned}
\tag{C.9}
$$

where $\boldsymbol{b}(s)$ and $\boldsymbol{t}(s)$ are the binormal and the tangent of the annulus sector, respectively.

The edge of regression can be mapped onto the annulus sector as

$$\begin{aligned} \boldsymbol{c}(s) &= \boldsymbol{r}(s) - \frac{\boldsymbol{b}(s) + \eta(s)\boldsymbol{t}(s)}{\eta' + \kappa_g(1+\eta^2)}\,, \\ &= \left(\frac{\sin\lambda - \eta\cos\lambda}{\eta' + \kappa_g(1+\eta^2)} + \sin\lambda\right)\boldsymbol{i} + \left(\frac{-\eta\sin\lambda - \cos\lambda}{\eta' + \kappa_g(1+\eta^2)} - \cos\lambda\right)\boldsymbol{j}\,. \end{aligned} \tag{C.10}$$

Bibliography

[1] A. E. H. Love. *A treatise on the mathematical theory of elasticity.* Dover, New York, 1927.